COSMOLOGICAL STRUCTURE FORMATION USING SPECTRAL METHODS

A thesis submitted in conformity with the requirements

for the degree of Master of Science

Department of Pure and Applied Mathematics

Rhodes University

by

Michelle Funcke

March 2016

Abstract

Numerical simulations are becoming an increasingly important tool for understanding the growth and development of structure in the universe. Common practice is to discretize the space-time using physical variables. The discreteness is embodied by considering the dynamical variables as fields on a fixed spatial and time resolution, or by constructing the matter fields by a large number of particles which interact gravitationally (N-body methods).

Recognizing that the physical quantities of interest are related to the spectrum of perturbations, we propose an alternate discretization in the frequency domain, using standard spectral methods. This approach is further aided by periodic boundary conditions which allows a straightforward decomposition of variables in a Fourier basis. Fixed resources require a high-frequency cut-off which lead to aliasing effects in non-linear equations, such as the ones considered here.

This thesis describes the implementation of a 3D cosmological model based on Newtonian hydrodynamic equations in an expanding background. Initial data is constructed as a spectrum of perturbations, and evolved in the frequency domain using a pseudo-spectral evolution scheme and an explicit Runge-Kutta time integrator. The code is found to converge for both linear and non-linear evolutions, and the convergence rate is determined. The correct growth rates expected from analytical calculations are recovered in the linear case. In the non-linear model, we observe close correspondence with linear growth and are able to monitor the growth on features associated with the non-linearity.

High-frequency aliasing effects were evident in the non-linear evolutions, leading to a study of two potential resolutions to this problem: a boxcar filter which adheres to "Orszag's two thirds rule" and an exponential window function, the exponential filter suggested by Hou & Li [1], and a shifted version of the exponential filter suggested, which has the potential to alleviate high frequency ripples resulting from the Gibbs' phenomenon. We found that the filters were somewhat successful at reducing aliasing effects but that the Gibbs' phenomenon could not be entirely removed by the choice of filters.

Acknowledgements

To my supervisors, Denis Pollney and Julien Larena, who have taught me everything I know about numerical simulations and cosmology.

Thank you to the NRF and Rhodes Henderson Scholarship for providing my funding during masters. Without which this thesis would not be possible.

To my proof readers: Peter Kogel, John Gowland and Matthew Funcke. Thank you for reading the whole paper with a critical mind, and correcting more than just my grammar.

Thank you to Sue Funcke for always making a plan. A big thank you to my family, both sides, for their love and support.

And the biggest thank you goes to my husband, Matthew. You have kept me sane through these three years of hard work and I appreciate all your help.

Contents

Part I

General Introduction

Chapter 1

Introduction

Cosmology is the study of the large scale properties of the universe. It aims to develop a model - although possibly idealised - of the origin, evolution and future of the universe. To ascertain the effectiveness of the model, its predictions are compared with observations made by astronomers.

Observations of the universe are limited due to:

1. Having only one point of observation.
2. The speed of light.
3. There were no free travelling photons before the cosmic microwave background (CMB).

Since there is only one observable universe, measurements must be taken from multiple points to gather more information. Cosmological predictions are made on intergalactic scales. Therefore, any changes in the observer's position, which are smaller than these scales, will have no observable effect. This is why observations are limited to one observation point (point 1).

In order to make observations, one receives light or electromagnetic waves from distant objects. These electromagnetic waves are limited to travelling at the speed of light (point 2). If the object, for example galaxy, is further away than the Hubble distance - discussed in Section 1.4 - then space is expanding faster than light [2]. In this case, light emitted from the object cannot reach Earth and be observed.

Light emitted by distant objects has to travel to Earth at the speed of light, which takes time. This implies that what is observed is not the current state of the object. Due to expansion, discussed in Section 1.4, the light emitted is subject to redshift while travelling. Light that was emitted further in the past has a longer wavelength. The CMB is the farthest into the past that can be observed due to the coupling of matter and photons before this time, discussed in Section 1.3.

These limitations impose a distinction between the universe and the *observable universe*. To develop a model of the universe, assumptions must be made about the areas that cannot be observed.

The standard cosmological model is based on four assumptions:

1. **General Relativity (GR) describes gravity** [3]. GR is Einstein's theory of space, time and gravitation [4], which he postulated at the end of 1915 [5]. This assumption has been proved for solar system scales but might not hold on larger scales or at earlier times.

2. The particles observed in the universe, for example galaxies, are a representation of the total matter content. The assumption is that on large scales **matter is described by a mixture of a pressureless fluid and radiation** [3].

3. The above assumption is not enough to solve Einstein's equation. Assumptions of the symmetric nature of spacetime need to be made as well - this is known as the **Cosmological principle** [3], discussed in Section 1.2.

4. The last assumption is that the universe exists in a **globally hyperbolic spacetime** [3]. This allows the choice of topology for spacetime to reduce to the choice of topology for the spatial sections [3].

The above four assumptions allow one to construct very successful universe models [3]. There are reasons to challenge these assumptions, but that will not be discussed in this thesis.

GR and the Cosmological principle are discussed in greater detail later in this chapter. The thermal history of the universe is then outlined, which leads into an explanation of the scale factor and Hubble parameter. Lastly, the theory of inflation is discussed.

1.1 General Relativity

Einstein developed the theory of GR in order to describe the spacetime distorting-effects of massive objects [5]. The spacetime metric, in the absence of mass, is flat. Curvature, i.e. the deviation of the spacetime metric from flatness, accounts for the physical effects usually attributed to a gravitational field [4, 5]. Massive objects, such as the Sun, produce a local distortion in the geometry of spacetime [5]. This distortion affects the motion of objects and photons around the massive object.

A key concept of GR is the spacetime interval ds^2, or line element [2], between nearby points. An inertial frame is defined as a coordinate system (t, x, y, z) in which [6]:

$$ds^2 = -dt^2 + dx^2 + dy^2 + dz^2. \tag{1.1}$$

This is usually written in the summation convention as [6]:

$$ds^2 = \eta_{\mu\nu} dx^\mu dx^\nu, \tag{1.2}$$

where $\eta_{\mu\mu} = (-1, 1, 1, 1)$ is called a metric tensor. The generic coordinate dx^μ can refer to $\left(x^0, x^1, x^2, x^3\right) = (t, x, y, z)$.

The spacetime interval, equation (1.1), can be written in spherical polar coordinates as:

$$ds^2 = -dt^2 + dr^2 + r^2 \left(d\theta^2 + \sin^2\theta d\phi^2\right). \tag{1.3}$$

By choosing this coordinate system, there is an underlying assumption that the spacetime surface is flat. Generally the spacetime is considered to be curved and can be regarded as flat in "small" regions [6].

The value of ds^2 determines the type of path it represents. The three types are [6]:

- Timelike if $ds^2 < 0$
- Spacelike if $ds^2 > 0$
- Lightlike if $ds^2 = 0$

A particle with mass follows a timelike path and a photon follows a lightlike path [2]. The set of all lightlike lines passing through a given spacetime point is called the lightcone [6]. This allows spacetime to be divided into the past ($ds^2 < 0$ with $t < 0$), the future ($ds^2 < 0$ with $t > 0$) and everywhere else ($ds^2 > 0$).

The line element of an arbitrary coordinate system is [6]:

$$ds^2 = g_{\mu\nu} dx^\mu dx^\nu, \tag{1.4}$$

where the metric tensor is now:

$$g_{\mu\nu} = \frac{\partial x'^\alpha}{\partial x^\mu} \frac{\partial x'^\beta}{\partial x^\nu} \eta_{\alpha\beta}. \tag{1.5}$$

The connection coefficients, or Christoffel symbols, are given by:

$$\Gamma^\gamma_{\beta\mu} = \frac{1}{2} g^{\alpha\gamma} \left(\partial_\mu g_{\alpha\beta} + \partial_\beta g_{\alpha\mu} - \partial_\alpha g_{\beta\mu}\right). \tag{1.6}$$

The Einstein equation [4]:

$$R_{\mu\nu} - \frac{1}{2} R g_{\mu\nu} + \Lambda g_{\mu\nu} = \frac{8\pi G}{c^4} T_{\mu\nu}, \tag{1.7}$$

links the curvature of the metric (left hand side) to the matter content (right hand side). The right-hand side contains the stress-energy-momentum tensor $T_{\mu\nu}$ which describes the matter in the universe. The left-hand side contains the Einstein tensor $G_{\mu\nu} = R_{\mu\nu} - \frac{1}{2}Rg_{\mu\nu}$ and the cosmological constant Λ [4]. The Einstein tensor is calculated from the Ricci tensor $R_{\mu\nu}$ and Ricci Scalar R which are given by first derivatives of the Christoffel symbols Γ^a_{bc}, defined in equation (1.6). The cosmological constant Λ refers to the energy density of the vacuum of space usually called dark energy [3]. Λ is considered to be small enough that deviations from Newtonian theory are not noticeable [4]. In this thesis it is assumed that $\Lambda = 0$.

1.2 Cosmological Principle

One of the corner stones of the standard cosmological model is the *cosmological principle.* The principle states that the universe is *spatially isotropic* and *homogeneous* [3].

An arrangement of particles is spatially isotropic if there exists a point that observes an invariant arrangement of particles under spatial rotations [7]. Whereas an arrangement of particles is spatially homogeneous if the arrangement of particles is invariant under translation of coordinates in space [7].

Observations of galaxies and the CMB suggest that the matter in the universe is spread isotropically [3] around Earth/The Milky Way. This alone does not affirm the cosmological principle since there are two possible scenarios that result in an isotropic arrangement of particles. Either there is only one point of observation that results in an isotropic view of the universe or the particles are spread isotropically around every point. The first scenario implies our galaxy is located at the centre of the universe which is statistically unlikely. Therefore the second scenario is assumed which is equivalent to stating that the universe is homogeneous.

Using the cosmological principle, definite predictions for all unobservable regions in the universe can be made due to homogeneity. Observations are still limited to one universe, observation limitation 1 (see Section 1).

It is clear from observations made on galactic scales that the universe is highly inhomogeneous on these scales. The cosmological principle only applies on large scales at the current epoch, and in a statistical sense, discussed in Section 3.1. In other words, for a universe smoothed on distances greater than its larger structures. The largest known cosmic structures are galaxy filaments which have a typical length $\sim 100h^{-1}$Mpc [8, 9].

1.3 Thermal History of the Universe

Wavelengths of electromagnetic waves are stretched due to the expansion of space. Therefore, waves that have been travelling for longer periods of time are stretched more. Observing longer wavelengths (radio waves) is equivalent

to seeing the universe at epochs further into the past. Using this information, astronomers are able to determine when particular events occurred. However, there is a time in the history of the universe that cannot be observed due to the scattering of light by free electrons.

Cosmology assumes the Big Bang model of the universe [6], Figure 1.1. This theory supposes that the whole universe expanded from a very high density and high temperature state [6]. The universe then began to expand and subsequently cool.

During the first second of the existence of the universe it went through several speculated processes. **Inflation** occurred after 10^{-42} s [6], discussed in Section 1.5. Once inflation ends, the universe continues to expand at a slower rate, $a(t) \propto t^{1/2}$. This time period is referred to as the **Cold Big Bang** [6]. At this stage, the universe is dominated by non-relativistic particles (matter dominated) which decay into relativistic particles at $10^{-18\pm6}$ s [6] to form radiation. This process is called *reheating*, since the radiation increases the temperature of the universe. This temperature increase marks the beginning of the **Hot Big Bang**, universal temperature $\sim 10^{6\pm3}$ GeV [6]. Once reheating has ended, the universe continues to expand and cool. The **electromagnetism and weak interaction fields decouple** once the temperature reaches 100GeV [6]. Free **quarks condense to form hadrons** once the universe cools to $\sim$ 200 MeV [6]. At this stage the hadrons (i.e. protons, neutrons and pions) exist in thermal equilibrium with the photons, neutrinos, electrons, positrons and various hyperons [10].

At the end of this second, the temperature has reduced enough for the neutrinos to decouple from the matter [6]. The hyperons and mesons then decay. The universe then consisted of free travelling neutrinos, electron-positron pairs, electrons, neutrons, protons and photons in thermal equilibrium at $T \sim 850$MeV ($T \sim 10^{10}$ K [10]). The electron-positron pairs then annihilated each other [6]. The neutrons and protons do not form stable nuclei at this point due to high energy protons which blast apart any atomic nucleus the moment it forms [10].

The universe continued to expand and cool until the conditions were right for nucleosynthesis [6, 10], time shown in Figure 1.2. This is the process whereby protons and neutrons bind together to form nuclei. Once the universe has cooled further, the protons are too cold to penetrate the Coulomb barrier and all the free neutrons decay into electrons and protons [10].

Thus far in the description, the universe has been dominated by radiation, red line in Figure 1.2. The density of the non-relativistic matter continues to increase - blue line in Figure 1.2. After 10^4 yr [6], the density of non-relativistic matter is the same as the density of the relativistic matter, known as matter-radiation equality [6]. Beyond this time, the universe is in the matter dominated era.

When the matter dominated era begins, the expansion rate changes from $a(t) \propto t^{1/2}$ to $a(t) \propto t^{2/3}$ [6] which decreases the temperature faster.

The above processes are unobservable due to the coupling of photons and matter. Consider Figure 1.1; the coloured regions of time cannot be observed since the light emitted is scattered by free electrons. The universe existed

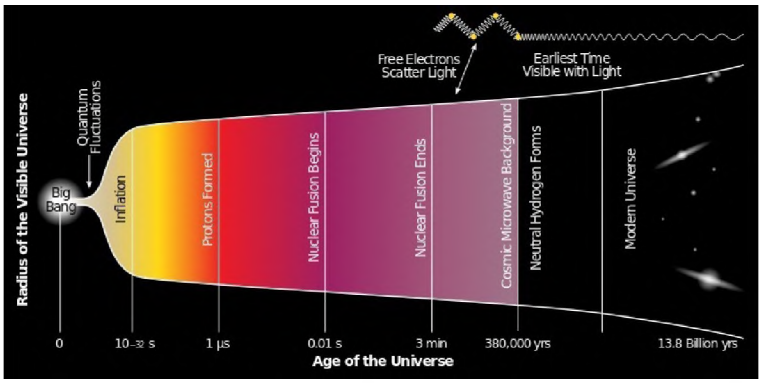

Figure 1.1: Diagram depicting the history of the universe where key stages are highlighted. Edited from Bicep2 2014 release image gallery [11]

as a particle-radiation plasma where photons did not travel far before being scattered. During the matter dominated era, the temperature of the universe cooled enough for photons to decouple from the matter, at 10^5 yr [6]. This process occurred in two stages. First, majority of the electrons bind to the nuclei to form atoms [6]. The remaining photons couple to the ionized electrons that remain. Shortly afterwards, the radiation decouples completely from the matter [6]. These photons propagate freely and become the Cosmic Microwave Background (CMB) [6]. Over time, the wavelength of the photons that make up the CMB become stretched due to expansion, top of Figure 1.1.

Nucleosynthesis created mostly Hydrogen and Helium [10] atoms. During the radiation dominated era the photon pressure did not allow the atoms to condense into stars and galaxies [10]. After photons decouple, small perturbations in the matter density grow until galaxies form and stars 'ignite' [10].

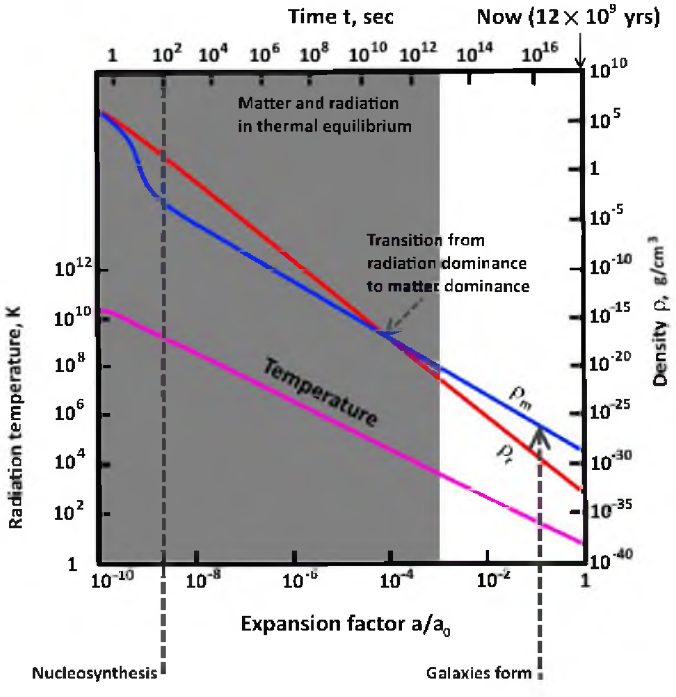

Figure 1.2: The figure illustrates how the density of radiation (red line) dominates the density of matter (blue line) until matter-radiation equality. The diagram includes a line illustrating the change in temperature of the universe (pink line). The grey area indicates where matter and radiation are in thermal equilibrium. Adapted from [10].

1.4 Scale Factor and Hubble Parameter

Since the universe is homogeneous and isotropic, the distance between any two comoving points (discussed in Chapter 6) is proportional to a universal scale factor $a(t)$ [6], where t is cosmic time. Since the scale factor at the present epoch is arbitrary [3], it is normalised to be unity, i.e. $a_0 = a(t_{present}) = 1$. Henceforth, the subscript 0 will denote present day values of the variable in question.

The scale factor is increasing with time; see Section 3.2. Therefore the distance between comoving points is increasing. This results in the redshift of light travelling from one point to another. Redshift, z, occurs when the wavelength of light from an object is increased. The redshift of a photon sent between two comoving observers is [3, 6]:

$$1 + z \equiv \frac{\lambda_{obs}}{\lambda_{emit}}, \tag{1.8}$$

where λ_{obs} is the wavelength of the light being observed and λ_{emit} is the wavelength of light that was emitted. The wavelength varies as the scale factor, $\lambda \propto a$, therefore [3, 6]:

$$1 + z = \frac{a(t_{obs})}{a(t_{emit})}. \tag{1.9}$$

Due to the connection between redshift, time and distance it is more convenient to quote time and distance in terms of redshift. When the redshift refers to a particular epoch, it represents the time at which the scale factor was a fraction $1/(1+z)$ of its present value.

At any epoch, the Hubble parameter H gives the rate of expansion of the universe,

$$H \equiv \frac{\dot{a}}{a}, \tag{1.10}$$

where $\dot{a}$ is the derivative of the scale factor with respect to cosmic time t. The present Hubble parameter is:

$$\begin{aligned} H_0 &= 100h \,\mathrm{km \cdot s^{-1} Mpc^{-1}} \\ &\simeq \frac{h}{3000} \,\mathrm{Mpc^{-1}}, \end{aligned}$$

where the last equality uses $c = 1$ and h is the dimensionless Hubble parameter which contains the uncertainty of H_0, $h = 0.72 \pm 0.05$ [3]. The Hubble time, H^{-1}, and Hubble distance, cH^{-1}, at the present epoch are:

$$\begin{aligned} H_0^{-1} &= 9.78h^{-1}\,\text{Gyr}, \\ cH_0^{-1} &= 2998h^{-1}\,\text{Mpc}. \end{aligned}$$

The Hubble time is the age the universe would have been if the expansion of the universe was linear [3]. The Hubble distance is the distance between the Earth and the galaxies which are currently receding from us at the speed of light [3].

1.5 Inflation

As discussed in Section 1.2, the universe on very large scales is assumed to be homogeneous and isotropic. The CMB radiation is spread isotropically around Earth. In order for this to occur, the particles must have been in causal contact [3] before the photons were released, i.e. decoupling.

For two points to be in causal contact at the time of decoupling, their future light cones need to intersect before the time of decoupling. It can be shown that the regions in causal contact at the time of decoupling are smaller than the size of the observable universe. This is known as the *horizon problem* [3].

To solve the horizon problem, a process is added to the Hot Big Bang model: *inflation*. Inflation is simply an epoch during which the scale factor of the universe is accelerating i.e. $\ddot{a} > 0$ [6]. Therefore, the universe was expanding really fast. An accelerating scale factor is easier to visualise using the comoving Hubble length [6]:

$$\frac{d}{dt}\frac{H^{-1}}{a} < 0, \tag{1.11}$$

where $\frac{H^{-1}}{a}$ is the comoving Hubble length. The comoving Hubble length is the characteristic scale of the expanding universe and governs the size of the observable universe [6]. Equation (1.11) implies that during inflation the observable universe shrank.

To visualise this, one begins with the observable universe before inflation, Figure 1.3. The shaded area represents the portion of the observable universe that is in causal contact at the beginning of inflation. This shaded region is well within the comoving Hubble radius at the beginning of inflation. The comoving Hubble length decreases during inflation until it is the size of the inner most circle. After inflation the scale factor is no longer accelerating and the comoving Hubble length starts to grow again. At the present epoch the comoving Hubble length is the size of the circle marked 'now'. This is still inside the shaded region, which explains why the CMB is observed to be isotropic.

The shaded region represents the homogeneous universe. The initial homogeneities (non-shaded region) end up on scales vastly larger than the observable universe at the present epoch [6]. This is why the universe is homogeneous on large scales.

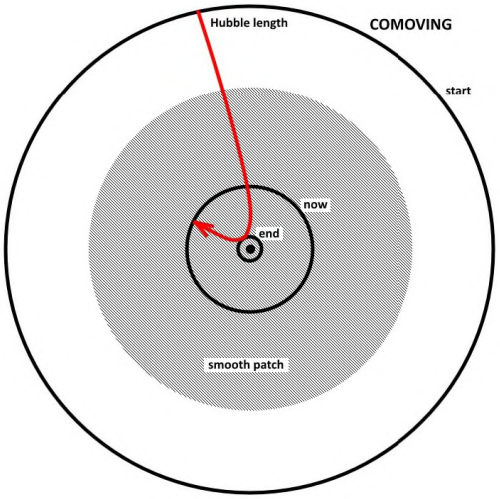

Figure 1.3: This diagram illustrates how the comoving Hubble length changes during inflation. The shaded area represents points that are in causal contact with the centre point at the start of inflation. During inflation the comoving Hubble length shrinks to the size of the inner most circle. After inflation ends the comoving Hubble length is free to grow. The observable universe is still contained in the shaded region which explains why the CMB is homogeneous and isotropic on large scales.

1.6 Outline of Thesis

This thesis is organised as follows:

Chapter 2 discusses cosmological perturbation theory. Beginning with the unperturbed universe, and then including perturbations. The decomposition into separate scalar, vector and tensor modes is then outlined. Gauges are then defined along with their significance. We then choose to adopt the Newtonian gauge.

Chapter 3 expands on the source of the perturbations discussed in the previous chapter. The equations describing this mechanism are discussed along with the derivation of the equations for the scale factor and Hubble radius. The chapter ends by looking at the evolution of modes as they enter the Hubble sphere during different epochs.

Chapter 4 discusses numerical simulations, beginning with a brief history. Two cosmologist groups: the Virgo consortium and the DEUS consortium are introduced, along with the codes and results they have produced. The reasoning behind creating large numerical simulations is then discussed. The latest observable results are mentioned, these results are used to set the initial conditions of the simulation. Lastly, the reason behind creating a new numerical code is

mentioned.

Chapter 5 outlines the theory behind the spectral method of evolution. All constraints are discussed along with the equations necessary to perform the evolution. The Runge-Kutta method of time evolution is then introduced and outlined.

Lastly the effects of aliasing are considered. The section describes the aliasing effects created by sampling a signal, i.e. high-frequency and low-frequency aliasing; effects created by performing a convolution; and effects created by applying a filter that creates a discontinuity. Different filters are suggested and their effects discussed. The section ends by discussing the types of aliasing that may be present on the grid and what will be done to try to limit them.

Chapter 6 outlines the process of determining the evolution equations. Beginning with a description on what the peculiar velocity is and the types of observers. The evolution equations are chosen to be the Euler equations. The Euler equations are derived from the Einstein equations for completeness.

The propagation equation is then derived during the two eras of interest: matter dominated and radiation dominated. The relationship between the physical and coded variables is defined. The propagation equation is linearised to obtain the general solution. The solution for the density contrast and velocity is determined for the evolution of just the growing mode. Lastly, the evolution equations and initial conditions are redefined in Fourier space for ease of programming.

Chapter 7 outlines the results obtained from the evolution. The convergence is determined along with a comparison between growing mode growth and the coded evolution. The evolution with no filter is then shown with a comparison between the 2/3rd boxcar filter and the suggested exponential filter. The results end with a look at the reduction of aliasing effects.

Chapter 8 is the conclusion. A summary of the results is presented along with the conclusions that can be drawn.

There are five chapters of the Appendix which contain the complete derivations of terms and equations discussed in the thesis.

Chapter 2

Cosmological Perturbation Theory

Cosmology uses GR to describe the curvature of spacetime. Without matter, the universe is a flat/curved spacetime, i.e. unperturbed. Once matter is included the metric of spacetime develops small fluctuations, i.e. perturbations.

This chapter begins by describing the perturbed and unperturbed universe. The scalar-vector-tensor decomposition is then described. This leads one to the concept of a Gauge; the way matter is described, and gauge invariant variables are then derived. Finally, the gauge of choice for this thesis is discussed.

2.1 The Unperturbed Universe

Consider a spacetime with no perturbations, i.e. no mass. Since there are no perturbations, the slices of fixed t can be chosen to be homogeneous [6]. To specify the geometry of a homogeneous three-dimensional space, a curvature parameter K is used [6]. This parameter appears in the Friedmann equation from Section 3.2.

The metric, in comoving spherical coordinates, takes the form [3]:

$$ds^2 = -dt^2 + a^2(t)\left[d\chi^2 + f_K^2(\chi)\left\{d\theta^2 + \sin^2\theta d\varphi^2\right\}\right], \tag{2.1}$$

where

$$f_K(\chi) = \begin{cases} K^{-1/2}\sin\left(\sqrt{K}\chi\right) & K > 0 \\ \chi & K = 0 \\ (-K)^{-1/2}\sinh\left(\sqrt{-K}\chi\right) & K < 0. \end{cases} \tag{2.2}$$

By using the radial coordinate $r = f_K(\chi)$, equation (2.1) can take the form:

$$ds^2 = a^2(\eta)\left[-d\eta^2 + \frac{dr^2}{1-Kr^2} + r^2\left(d\theta^2 + \sin^2\theta d\varphi^2\right)\right], \quad (2.3)$$

where t has been replaced by conformal time η, and $dt = a(t)\,d\eta$. This metric is called the Friedmann-Lemaitre-Robertson-Walker (FLRW) metric [6].

2.2 The Perturbed Universe

Since the universe is neither perfectly flat nor perfectly curved, the spacetime contains small perturbations. There are two formalisms for cosmological perturbation theory [3]. This thesis follows the standard method introduced by Bardeen [12]. The method introduces arbitrary parametrisations of the perturbations which can then be used to construct gauge invariant variables. The other approach will not be discussed - however, both approaches do lead to equivalent physical results [3].

Let $\bar{g}_{\mu\nu}$ represent the FLRW metric, equation (2.3). The metric of a perturbed spacetime, $g_{\mu\nu}$, can then be written as [3]:

$$g_{\mu\nu} = \bar{g}_{\mu\nu} + \delta g_{\mu\nu}, \quad (2.4)$$

where $\delta g_{\mu\nu}$ represents small deviations from the FLRW metric. The inverse metric is given by [3]:

$$g^{\mu\nu} = \bar{g}^{\mu\nu} + \delta g^{\mu\nu}\ , \qquad \delta g^{\mu\nu} = -\bar{g}^{\mu\sigma}\bar{g}^{\nu\lambda}\delta g_{\sigma\lambda}\ , \quad (2.5)$$

to first-order. This implies that the indices of all tensor and vector quantities can be raised or lowered using the unperturbed spatial metric, γ_{ij} - which is the spatial portion of equation (2.1).

The line element of $g_{\mu\nu}$ is written as [3]:

$$ds^2 = a^2(\eta)\left[-(1+2A)\,d\eta^2 + 2B_i dx^i d\eta + (\gamma_{ij} + h_{ij})\,dx^i dx^j\right], \quad (2.6)$$

where A is the lapse function, B_i is the shift function, γ_{ij} is the spatial portion of the FLRW metric written in comoving spherical coordinates and h_{ij} is a rank 2 symmetric tensor.

The quantities A, B_i and h_{ij} are unknown functions of space and time that are determined from the Einstein equations.

2.3 Scalar-Vector-Tensor Decomposition

The previous section defined the perturbed spacetime metric. The metric contains scalars, vectors and tensors. It is more useful to perform a scalar-vector-tensor decomposition (SVT) which separates these components.

Any vector field can be decomposed as the sum of the gradient of a scalar and a divergence-less vector as [3]:

$$B^i = \partial^i B + \bar{B}^i \quad \text{with} \quad \partial^i \bar{B}_i = 0, \tag{2.7}$$

where ∂^i represents a derivative with respect to the i-th component. In a similar way, any rank 2 symmetric tensor can be decomposed as [3]:

$$\begin{aligned} h_{ij} \quad &= \quad 2C\gamma_{ij} + 2\partial_i\partial_j E + 2\partial_{(i}\bar{E}_{j)} + 2\bar{E}_{ij} \\ &\text{with} \quad \partial_i \bar{E}^{ij} = 0, \quad \bar{E}^i_i = 0 \ . \end{aligned} \tag{2.8}$$

The size components of h_{ij} can be split into 2 scalar (C and E), 2 vector ($\bar{E}_j$) and 2 tensor $\bar{E}_{ij}$ components. Thus, the metric has been decomposed into 4 scalars (A, B, C and E), 2 vectors ($\bar{B}^i$ and $\bar{E}^i$) and 1 tensor ($\bar{E}^{ij}$) [3].

The biggest advantage of using this decomposition is that, to leading order, the scalar, vector and tensor parts decouple. Thus, the components can be studied separately without ignoring contributions from the other components.

2.4 Gauges

2.4.1 The Gauge Freedom

In Section 2.2, the metric $g_{\mu\nu}$ was assumed to be 'close' to that of the FLRW metric. This was done in order to compare the perturbed metric with a metric that is well understood. During this process an arbitrary freedom is introduced in the way points are identified.

Consider Figure 2.1 where $\overline{\mathcal{M}}$ represents the Friedmann-Lemaître universe and $\mathcal{M}$ represents the perturbed metric. The isomorphism ψ has been formulated in order to relate the points of the two spaces. There is no 'natural' choice for this isomorphism, which implies that there are some unphysical degrees of freedom related to the choice of the coordinate systems on the two manifolds [3].

Locally, the spacetime metric is flat, and all systems of coordinates are equivalent [3]. Differences between coordinate systems are expected on large scales, i.e. scales above the Hubble radius [3].

When choosing a coordinate system, it is necessary that they reduce to the standard coordinates in the limit where perturbations vanish [6]. A **gauge** is a coordinate system that satisfies this constraint [6]. Equation (2.6) assumes implicitly that a system of coordinates has been chosen in the perturbed space. Therefore, any change of coordinates will modify the form of the metric coefficients [3].

It is important to separate the quantities into those that are intrinsic to the manifold in which the perturbations evolve, and the artificially generated ones.

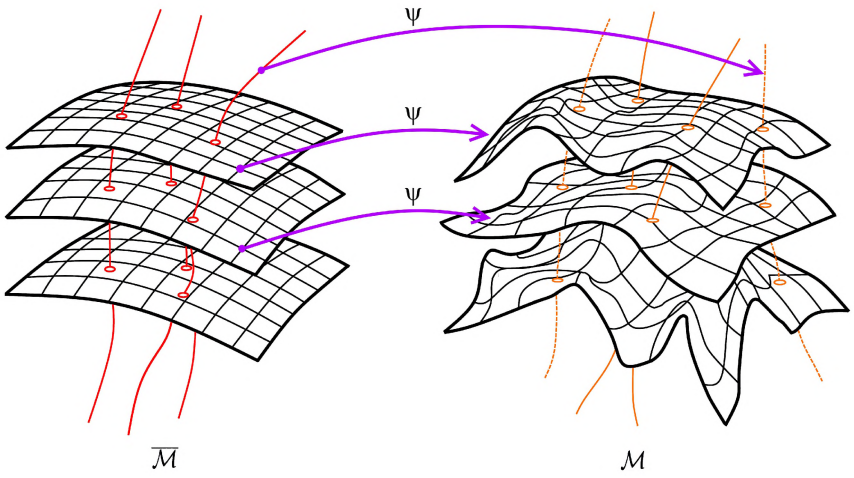

Figure 2.1: Any perturbed quantity can be mapped between Friedmann-Lemaître spacetime, $\overline{\mathcal{M}}$, and the perturbed spacetime $\mathcal{M}$. Adapted from [3]

2.4.2 Gauge Transformation and Invariant Variables

The previous section illustrated that two spacetimes can be related using a gauge. There exist quantities that do remain gauge invariant. These quantities need to be described.

To begin, consider a coordinate transform generated by the vector field ξ. The coordinates of a point change like [3]:

$$x^\mu \quad \rightarrow \quad x^\mu - \xi^\mu. \tag{2.9}$$

The displacement vector ξ^μ is decomposed into two scalar degrees of freedom (T and L) and two vector degrees of freedom ($\bar{L}^i$, which is divergence-less $\partial_i \bar{L}^i = 0$) as $\xi^0 = T$, $\xi^i = L^i = \partial^i L + \bar{L}^i$.

Under this operation, the metric transforms as [3]:

$$g_{\mu\nu} \quad \rightarrow \quad g_{\mu\nu} + \mathfrak{L}_\xi g_{\mu\nu}. \tag{2.10}$$

To first-order the perturbations are:

$$\delta g_{\mu\nu} \rightarrow \quad \delta g_{\mu\nu} + \mathfrak{L}_\xi \bar{g}_{\mu\nu} = \quad \delta g_{\mu\nu} + 2\nabla_{(\mu}\xi_{\nu)}, \tag{2.11}$$

which implies that the metric perturbation variables transform as [3]:

$$A \quad \rightarrow \quad A + T' + \mathcal{H}T \tag{2.12}$$

$$B_i \quad \rightarrow \quad B_i - \partial_i T + L_i' \tag{2.13}$$

$$h_{ij} \quad \rightarrow \quad h_{ij} + \partial_i L_j + \partial_j L_i + 2\mathcal{H}T\gamma_{ij}. \tag{2.14}$$

Using the scalar-vector-tensor decomposition of equations (2.7) and (2.8), the following expressions for the different modes are derived [3]:

Scalar	Vector	Tensor
$A \rightarrow A + T' + \mathcal{H}T$	$\bar{B}^i \rightarrow \bar{B}^i + \bar{L}^{i\prime}$	$\bar{E}_{ij} \rightarrow \bar{E}_{ij}$
$B \rightarrow B - T + L'$	$\bar{E}^i \rightarrow \bar{E}^i + \bar{L}^i$	
$C \rightarrow C + \mathcal{H}T$		
$E \rightarrow E + L$		

The arbitrariness is removed by specifying additional conditions, i.e. choosing a gauge.

There exist some combinations of the above quantities that do not depend on L^i and T, [3]:

$$\Psi \equiv -C - \mathcal{H}(B - E'), \tag{2.15}$$

$$\Phi \equiv A + \mathcal{H}(B - E') + (B - E')', \tag{2.16}$$

$$\bar{\Phi}^i \equiv \bar{E}^{i\prime} - \bar{B}^i, \tag{2.17}$$

$$\bar{E}^{ij}. \tag{2.18}$$

The above quantities can be neither simplified nor eliminated by change of coordinates [3].

2.5 Description of Matter

The initial perturbations present on the metric of the universe are assumed to be very small, i.e. quantum fluctuations. Therefore, the metric is a smooth surface on larger scales.

During radiation domination, the matter content of the universe can be modelled as a perfect fluid with pressure. Once radiation decoupling has taken place, the universe can be modelled as a fluid with zero pressure.

The energy-momentum tensor that describes a perfect fluid in an unperturbed space is of the form [3]:

$$T_{\mu\nu} = (\rho + P) u_\mu u_\nu + P g_{\mu\nu}, \tag{2.19}$$

where ρ is the density, P is the pressure, u_μ is the velocity and $g_{\mu\nu}$ is the metric from Section 2.2. In the presence of perturbations, the energy-momentum tensor of a perturbed fluid takes the general form [3]:

$$\begin{aligned} \delta T_{\mu\nu} = {} & (\delta\rho + \delta P)\, \bar{u}_\mu \bar{u}_\nu + \delta P \bar{g}_{\mu\nu} \\ & + 2(\rho + P)\, \bar{u}_{(\mu} \delta u_{\nu)} + P \delta g_{\mu\nu} + a^2 P \pi_{\mu\nu}, \end{aligned} \tag{2.20}$$

where $u^\mu = \bar{u}^\mu + \delta u^\mu$ is the four-velocity of a comoving observer, satisfying $u_\mu u^\mu = -1$, and $\pi_{\mu\nu}$ is the anisotropic stress tensor. Once δu_μ and $\pi_{\mu\nu}$ are

decomposed into their scalar, vector and tensor parts, the components of the perturbed energy-momentum tensor [equation (2.19)] are [3]:

$$\delta T_{00} = \rho a^2 (\delta + 2A), \tag{2.21}$$
$$\delta T_{0i} = -\rho a^2 \left[(1+w)(\partial_i v + \bar{v}_i) + \partial_i B + \bar{B}_i\right], \tag{2.22}$$
$$\delta T_{ij} = P a^2 \left(h_{ij} + \frac{\delta P}{P}\gamma_{ij} + \pi_{ij}\right), \tag{2.23}$$

where $\delta \equiv \frac{\delta\rho}{\bar{\rho}}$ is the density contrast, w is the ratio of the pressure and density of the fluid, i.e. $\frac{P}{\rho}$, and A, B, h_{ij} and γ_{ij} are the parameters discussed in Section 2.2.

2.6 Gauge Invariant Quantities

A change of coordinates is now performed, equation (2.9). The scalars transform as [3]:

$$\begin{aligned} \delta Q &\rightarrow \delta Q + \mathcal{L}_\xi \bar{Q}, \\ \mathcal{L}_\xi \bar{Q} &= \xi^\alpha \partial_\alpha \bar{Q} = T\bar{Q}', \end{aligned}$$

and the vectors transform as:

$$\begin{aligned} \delta u^\mu &\rightarrow \delta u^\mu + \mathcal{L}_\xi \bar{u}^\mu, \\ \mathcal{L}_\xi \bar{u}^\mu &= \xi^\alpha \partial_\alpha \bar{u}^\mu - u^\alpha \partial_\alpha \xi^\mu. \end{aligned}$$

Therefore, δP, $\delta\rho$, v and $\bar{v}_i$ transform as [3]:

$$\delta\rho \rightarrow \delta\rho + \rho' T, \tag{2.24}$$
$$\delta P \rightarrow \delta P + P' T, \tag{2.25}$$
$$v \rightarrow v - L', \tag{2.26}$$
$$\bar{v}_i \rightarrow \bar{v}_i - \bar{L}_i'. \tag{2.27}$$

The gauge invariant quantities associated with the above can now be determined. The gauge invariant quantities are defined as [3]:

$$\delta^N = \delta + \frac{\rho'}{\rho}(B - E'), \tag{2.28}$$

$$\delta^F = \delta - \frac{\rho'}{\rho}\frac{C}{\mathcal{H}}, \tag{2.29}$$

$$\delta^C = \delta + \frac{\rho'}{\rho}(v + B), \tag{2.30}$$

$$V = v + E', \tag{2.31}$$

$$\bar{V}_i = \bar{v}_i + \bar{B}_i, \tag{2.32}$$

$$\bar{W}_i = \bar{v}_i + \bar{E}'_i. \tag{2.33}$$

These variables are related to each other by [3]:

$$\delta^F = \delta^N + \frac{\rho'}{\rho}\frac{\Psi}{\mathcal{H}}, \tag{2.34}$$

$$\delta^C = \delta^N + \frac{\rho'}{\rho}V, \tag{2.35}$$

$$\bar{W}_i = \bar{V}_i + \bar{\Phi}_i, \tag{2.36}$$

where $\delta = \frac{\delta\rho}{\rho}$ is the total density contrast.

2.7 Newtonian or Longitudinal Gauge

The gauge invariant variables have been defined above. However, these variables have no direct physical interpretation. The quantity δ^N can only be interpreted as the density contrast if it is measured by an observer using this gauge. To relate them to physical quantities, one needs to find a gauge where the perturbation variables reduce to the gauge invariant quantities.

The Newtonian gauge is an example of such a gauge; this is the gauge chosen for this thesis. By setting up a N-body simulation, as discussed in Chapter 4, the gauge is chosen to be Newtonian.

The characteristics of this gauge are:

- The scalar portion of the perturbed metric is diagonal, i.e. $B = 0$ and $E = 0$.
- The vector part is chosen to be zero, i.e. $\bar{B}_i = 0$.

This fixes the gauge completely since the transformation from an arbitrary gauge to the Newtonian is [3]:

$$T = B - E' \ , \quad L = -E \ \text{ and } \quad \bar{L}'_i = -\bar{B}_i.$$

Using the relations from equations (2.15)-(2.18), (2.28), (2.31) and (2.32), the perturbed quantities in terms of the gauge invariant variables are [3]:

$$\begin{aligned} A &= \Phi, \\ C &= -\Psi, \\ \delta &= \delta^N, \\ \delta P &= \delta P^N, \\ v &= V, \\ \bar{v}_i &= \bar{V}_i. \end{aligned}$$

The line element of the Newtonian gauge is [3, 6]:

$$ds^2 = a^2(\eta)\left[-(1+2\Phi)\,d\eta^2 + (1-2\Psi)\,\gamma_{ij}dx^i dx^j\right]. \tag{2.37}$$

Note that locally, all coordinate systems are equivalent; differences are only expected on large scales. It will be shown in Section 3.3 that the limiting scale is the Hubble radius.

Chapter 3

Origin of Structure

The universe began as a homogeneous and isotropic arrangement of matter [3]. However, the universe is highly inhomogeneous on small scales at the current epoch. The origin of the inhomogeneities could be due to gravitational effects, or contained within the initial conditions [6].

Inflation has helped solve the horizon problem, Section 1.5. It also provides a source for the inhomogeneities. The quantum fluctuations in the inflation field about its vacuum state [6] grow over time to create the inhomogeneities.

Let ϕ be the inflation field and $\delta\phi$ be its vacuum fluctuation. The vacuum fluctuation is usually expressed as a Fourier expansion in a comoving box with sides of comoving length L [6]:

$$\delta\phi(\mathbf{x},t) = \sum_{\mathbf{k}} \delta\phi_{\mathbf{k}}(t)\, e^{i\mathbf{k}\cdot\mathbf{x}}, \tag{3.1}$$

where $\mathbf{x}$ is related to the physical position as discussed in Section 6.1. The possible values of $\mathbf{k}$ form a cubic lattice, with spacing

$$\triangle k = \frac{2\pi}{L}. \tag{3.2}$$

The inverse wavenumber $\frac{a}{k}$ defines a distance scale where $\frac{aH}{k} < 1$ represents a scale inside the horizon, and outside the horizon otherwise. During inflation some scales exit the horizon, discussed in Section 1.5. After inflation, the Hubble radius increases and scales begin to re-enter the horizon. The scales are influenced by the time at which they enter the horizon, and will grow with different behaviours and rates depending on whether they enter during the matter dominated era or radiation dominated era.

The perturbations in the inflation field create perturbations in the energy density $\delta\rho(\mathbf{x},t)$ and hence the metric of spacetime [6]. Once the inflation field decays into conventional matter, it creates perturbations $\delta\rho_i(\mathbf{x},t)$ in the densities of individual particle species [6] for example baryons.

The perturbations can be seen in observations of the CMB anisotropies [13]. There are small fluctuations in the temperature of the CMB. Due to the uniform distribution of photons, perturbations are small, and linear response theory applies [13] for most times.

This chapter discusses the initial data chosen for the study of structure formation. The expressions for the background quantities, such as the scale factor, are derived for each epoch. The chapter ends with a look at the evolution of modes after horizon re-entry.

3.1 Initial Conditions

As discussed in Section 1.3, the universe existed as a baryons, and photon plasma during the radiation dominated era [after inflation]. Once the universe cooled enough to allow the baryons and photons to decouple, the photons were emitted and became the CMB.

The vacuum fluctuation altered the initial positions of the baryons. The vacuum fluctuation has a statistical nature [6].

The probability distribution function cannot be completely random due to the isotropic nature of the CMB. Therefore, the cosmological principle imposes that the probability distribution must be statistically isotropic and homogeneous [7].

Let the probability distribution of a field $g(\mathbf{x})$ be described by a 3-dimentional normal (Gaussian) distribution of the form [6]:

$$\mathbf{P}(g) = \frac{1}{\sqrt{2\pi\sigma_g^2}} \exp\left(-\frac{g^2}{2\sigma_g^2}\right), \tag{3.3}$$

where the mean is zero and $\sigma_g^2(\mathbf{x})$ is the variance. Approximating the independent random variables by a normal distribution is allowed, thanks to the central limit theorem [14].

Another useful statistical property is the correlation function:

$$\xi(\mathbf{x}, \mathbf{r}) = \langle g(\mathbf{x})\, g(\mathbf{x}+\mathbf{r}) \rangle . \tag{3.4}$$

Since the field $g(\mathbf{x})$ is assumed to be statistically isotropic and homogeneous, the correlation function only depends on the relative separations $r \equiv |\mathbf{r}|$. Equation (3.4) can be written as:

$$\xi(\mathbf{x}, \mathbf{r}) = \xi(r) . \tag{3.5}$$

The field is initialised in Fourier space by expanding in Fourier modes as [3, 6]:

$$g(\mathbf{r}) = \int \frac{d^3\mathbf{k}}{(2\pi)^{3/2}} g_{\mathbf{k}} \exp(i\mathbf{k}\cdot\mathbf{r}), \tag{3.6}$$

where the Fourier transform also contains a factor of $\frac{1}{(2\pi)^{3/2}}$. Since $g(\mathbf{r})$ is a real-valued field, the conjugation relation has to be satisfied:

$$g_{\mathbf{k}}^{\star} = g_{-\mathbf{k}}, \tag{3.7}$$

where $g_{\mathbf{k}}^{\star}$ represents the complex conjugate of $g_{\mathbf{k}}$. The spectrum is given by [3, 6]:

$$\langle g_{\mathbf{k}} g_{\mathbf{k}'} \rangle = \delta_D \left(\mathbf{k} + \mathbf{k}' \right) P_g \left(k \right), \tag{3.8}$$

where δ_D is the Dirac delta function and P_g is the power spectrum, which is defined as [6, 15]:

$$P_g \equiv L^3 \left\langle \left| g_{\mathbf{k}} \right|^2 \right\rangle, \tag{3.9}$$

where $\left\langle \left| g_{\mathbf{k}} \right|^2 \right\rangle$ is the variance of $\left| g_{\mathbf{k}} \right|^2$ and L is the size of the box at the present epoch. Derivations can be found in Appendix B. The power spectrum is related to the correlation function by:

$$P_g \left(k \right) = \int d^3 \mathbf{r} \xi \left(r \right) \exp \left[i \mathbf{k} \cdot \mathbf{r} \right], \tag{3.10}$$

where $k \equiv |\mathbf{k}|$. The power spectrum is defined in physical units. It is more useful to define a dimensionless spectrum [3, 13, 16]:

$$\mathcal{P}_g \left(k \right) = \frac{k^3}{2\pi^2} P_g \left(k \right). \tag{3.11}$$

Using equation (3.9), the spectrum is related to the variance by:

$$\mathcal{P}_g \left(k \right) \equiv \left(\frac{L}{2\pi} \right)^3 4\pi k^3 \left\langle \left| g_{\mathbf{k}} \right|^2 \right\rangle. \tag{3.12}$$

The equation for the spectrum is determined by the model of inflation used. In almost all models of inflation, the spectrum can be taken as a power law [6, 15, 16, 17, 18]:

$$\mathcal{P}_{\phi} \left(k \right) = \mathcal{P}_0 \left(\frac{k}{k_*} \right)^{n-1}, \tag{3.13}$$

where k_* is the pivot wavenumber, n is the spectral index relative to that wavenumber, and $\mathcal{P}_0$ is a constant set by its value today. Recent surveys have measured n [19]:

$$n \left(k_* = 0.002 \, \mathrm{Mpc}^{-1} \right) = 0.968 \pm 0.012. \tag{3.14}$$

$\mathcal{P}_0$ is set according to observations [20], the most recent measurement is [19]:

$$\mathcal{P}_0 = 2.42 \times 10^{-9}. \tag{3.15}$$

The field $g \left(\mathbf{x} \right)$ is chosen to have a Gaussian probability distribution. This implies that both the real and imaginary components of $g_{\mathbf{k}}$ have a Gaussian probability distribution.

Let R_n and I_n be the real and imaginary components. The components are independent and not correlated. Therefore, the variances must be equal [6]:

$$\sigma_n^2 = \left\langle R_n^2 \right\rangle = \left\langle I_n^2 \right\rangle = \frac{1}{2} \left\langle |g_{\mathbf{k}_n}|^2 \right\rangle . \tag{3.16}$$

The spectrum is thus related to the individual variances by:

$$\mathcal{P}_g \left(k_n \right) = 8\pi \left(\frac{L}{2\pi} \right)^3 k_n^3 \sigma_n^2. \tag{3.17}$$

In the simulation created for this thesis, the variance is fed into the random number generator. The initial field can either be determined by generating two Gaussian random numbers (one for each of the components of the complex field), or by generating one Rayleigh random number for the magnitude of the complex number - and then a uniformly random number for the angle. Appendix C demonstrates how these two approaches are equivalent.

3.2 Friedmann Equation

Before the evolution of individual modes is discussed, consider the Friedmann and acceleration equations [3]:

$$H^2 = \frac{\kappa}{3}\rho - \frac{K}{a^2} + \frac{\Lambda}{3}, \tag{3.18}$$

$$\frac{\ddot{a}}{a} = -\frac{\kappa}{6}\left(\rho + 3P\right) + \frac{\Lambda}{3}, \tag{3.19}$$

where $\kappa = 8\pi G_N$ and $H = \frac{\dot{a}}{a}$ [3]. These two equations are derived from the Einstein tensor, equation (1.7), and the energy-momentum tensor, equation (2.19).

The matter conservation equation ($\nabla_\mu T^{\mu\nu}$) reduces to a single equation:

$$0 = \dot{\rho} + 3H\left(\rho + P\right). \tag{3.20}$$

In order to solve this system of equations additional information is required, calculations in Appendix A. The equation of state is [3]:

$$P = w\rho, \tag{3.21}$$

where

- pressureless matter is described by $w = 0$
- radiation is described by $w = \frac{1}{3}$
- cosmological constant is described by $w = -1$

By using equation (3.21) in equation (3.20) and integrating by time, the relationship between the density and scale factor is:

$$\frac{\rho}{\rho_0} = \left(\frac{a}{a_0}\right)^{-3(1+w)}, \tag{3.22}$$

where $a_0 = 1$ and ρ_0 is the background density measured at the present epoch. The scale factor can be written in terms time for some simple cases.

This thesis considers the case where $K = \Lambda = 0$ and $w \neq -1$. equation (3.18) is simplified to:

$$H = \pm\sqrt{\frac{\kappa}{3}\rho_0}a^{-3(1+w)/2}, \tag{3.23}$$

where equation (3.22) has been used. Since universe is expanding, the positive expression is taken. Rewriting H in terms of the scale factor gives:

$$a^{(1+3w)/2}\dot{a} = \sqrt{\frac{\kappa}{3}\rho_0}. \tag{3.24}$$

Integrating with respect to time gives the scale factor in terms of cosmic time t:

$$a(t) = \left(\frac{t}{t_0}\right)^{2/3(1+w)}. \tag{3.25}$$

Using equation (1.10) and equation (3.22), the Hubble parameter and density in terms of cosmic time are:

$$H(t) = \frac{2}{3(1+w)}\frac{1}{t}, \tag{3.26}$$

$$\rho(t) = \frac{3}{\kappa}H_0^2\left(\frac{t}{t_0}\right)^{-2}. \tag{3.27}$$

Equations (3.25), (3.26) and (3.27) are defined in terms of t where t_0 is the age of the universe, $t_0 = 13.76 * 10^9 yr$ [19]. It is more convenient to define a new time variable:

$$\tau \equiv \frac{t}{t_0}. \tag{3.28}$$

Which allows the time to vary between 0 and 1. Equations (3.25), (3.26) and (3.27) become:

$$a(\tau) = \tau^{2/3(1+w)}, \tag{3.29}$$

$$H(\tau) = H_0 \frac{1}{\tau}, \tag{3.30}$$

$$\rho(\tau) = \frac{3}{\kappa} H_0^2 \tau^{-2}, \tag{3.31}$$

where $H_0 = \frac{2}{3(1+w)} \frac{1}{t_0}$. The redshift can be written in terms of τ:

$$1 + z = \tau^{-2/3(1+w)}. \tag{3.32}$$

3.3 Evolution of Modes

Section 1.5 discussed how the Hubble radius decreased with respect to conformal time during inflation. Modes behave differently depending on the time at which they re-enter the Hubble sphere, mentioned in introduction. This section will describe how the modes behave and what affects their behaviour.

The characteristic scale is the comoving Hubble length $\mathcal{H}$. The modes k at an epoch can be [3]:

$$\begin{array}{lll} k \ll \mathcal{H} & \text{super} - \text{Hubble mode} & \text{wavelength larger than Hubble radius,} \\ k \gg \mathcal{H} & \text{sub} - \text{Hubble mode} & \text{wavelength smaller than Hubble radius.} \end{array}$$

To study the evolution of structure, an understanding of how the modes of the density change over time is necessary. The evolution of the gravitational potential is linked to the density via the poison equation.

The evolution equation for the gravitational potential is given by [3]:

$$\begin{aligned} &\Phi'' + 3\mathcal{H}\left(1 + c_s^2\right)\Phi' \\ &+ \left[2\mathcal{H}' + \left(\mathcal{H}^2 - K\right)\left(1 + 3c_s^2\right)\right]\Phi - c_s^2 \triangle \Phi = \frac{\kappa}{2} a^2 P \Gamma, \end{aligned} \tag{3.33}$$

where c_s is the speed of sound and Γ is the entropy perturbation. This thesis considers the case of a flat universe ($K = 0$) with no entropy perturbation ($\Gamma = 0$).

This section will first consider the evolution of modes during a particular epoch. The evolution of modes during the transition between eras is then discussed. Lastly, the evolution of small perturbations is discussed.

3.3.1 During the Radiation Dominated Era:

During the radiation dominated era, the photons and matter are coupled together. This is modelled as a fluid with a constant equation of state $w \neq 0$ and implies $c_s^2 = w$.

Assuming $w \neq -1$ and $w \neq -\frac{1}{3}$, the scale factor is $a \propto \eta^\nu$ where $\nu = \frac{2}{(1+3w)}$ [this follows directly from equation (3.25) and $dt = a(t)\, d\eta$].

The evolution equation (3.33) can be written in Fourier space as:

$$\hat{\Phi}'' + 3\mathcal{H}(1+w)\hat{\Phi}' + \left[2\mathcal{H}' + \mathcal{H}^2(1+3w)\right]\hat{\Phi} + wk^2\hat{\Phi} \quad = \quad 0. \qquad (3.34)$$

To find the solutions to the above equation, set $f = x^\nu \hat{\Phi}$ where $x = k\eta$. After some manipulation, the form becomes [3]:

$$\frac{d^2 f}{dx^2} + \frac{2}{x}\frac{df}{dx} + \left[w - \frac{\nu(\nu+1)}{x^2}\right] f \quad = \quad 0. \qquad (3.35)$$

The general solution for this equation is a combination of Bessel functions [3]. The gravitational potential is given by:

$$\hat{\Phi} \quad = \quad x^{-\nu}\left[A j_{\nu+\frac{1}{2}}(c_s x) + B n_{\nu+\frac{1}{2}}(c_s x)\right], \qquad (3.36)$$

where $j_{\nu+\frac{1}{2}}$ and $n_{\nu+\frac{1}{2}}$ are spherical Bessel functions. Due to the asymptotic nature of the Bessel functions,

- When $c_s x \ll 1$, the gravitational potential remains constant.
- When $c_s x \gg 1$ and $-\frac{1}{2} < w < \frac{1}{3}$, the gravitational potential shows damped oscillatory behaviour.
- When $c_s x \gg 1$ and $w = \frac{1}{3}$, the gravitational potential oscillates with a constant amplitude.

The Poisson equation (6.25) allows the density contrast to be obtained from the gravitational potential. When $c_s x \gg 1$, the mode also shows dampened oscillator behaviour. When $c_s x \ll 1$:

$$\delta^c \propto \frac{\Phi}{\bar{\rho} a^2} \quad \propto \quad a^2. \qquad (3.37)$$

Since $\bar{\rho} \propto a^{-4}$. Therefore, the density grows like the square of the scale factor when the mode is on super-Hubble scales.

Consider the case where $w = \frac{1}{3}$, Figure 3.1 illustrates how the choice of gauge affects the evolution of the density contrast. When $c_s x > 1$ there is virtually no difference between the density contrasts. The differences get larger as $c_s x < 1$. This serves to illustrate how in the observable universe the choice of gauge does not affect results. Once modes outside the observable universe are taken into consideration differences are expected.

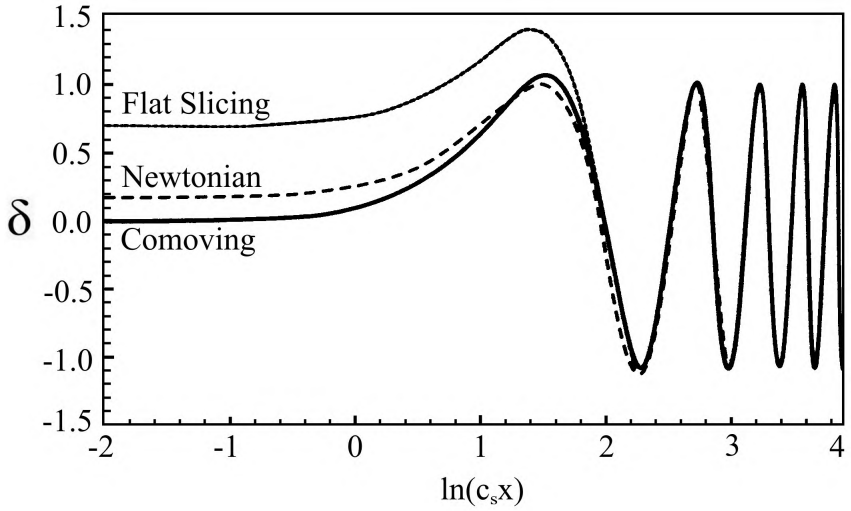

Figure 3.1: Evolution of the density contrast for different gauges. [3]

3.3.2 During the Matter Dominated Era:

Modes behave differently during the matter dominated era. Radiation has decoupled from matter, therefore $w = c_s^2 = 0$ and $\nu = 2$. The evolution equation of the gravitational potential takes the form [3]:

$$\frac{d^2 f}{dx^2} + \frac{2}{x}\frac{df}{dx} + \frac{6}{x^2} f = 0, \tag{3.38}$$

The general solutions of which lead to [3]:

$$\Phi = \Phi_+ + \Phi_- x^{-5}, \tag{3.39}$$

$$\delta^c = -\frac{1}{6} x^2 \Phi. \tag{3.40}$$

And since $a \propto \eta^2 \propto x^2$, the density contrast of matter grows like:

$$\delta_m^c \propto a. \tag{3.41}$$

Which is derived in more detail in Section 6.6.

3.3.3 Modes Entering the Horizon

In the previous two subsections the evolution of modes during the two eras was discussed. Not all modes remain sub-Hubble or super-Hubble at all times.

Consider the following k_i, where i = number:

1. The scale is always sub-Hubble.
2. The scale is super-Hubble and becomes sub-Hubble during the radiation dominated era.
3. The scale is super-Hubble until matter-radiation equality.
4. The scale is super-Hubble and becomes sub-Hubble during the matter dominated era.
5. The scale is still super-Hubble.

Since mode k_5 is not in the observable universe, its evolution will not be considered.

The rest of the modes are shown in Figure 3.2. The modes become sub-Hubble once they cross the red line in Figure 3.2(a). The area to the left of the eq[a_{eq}] line represents the radiation dominated era, while the right represents the matter dominated era.

Modes like k_1 oscillate during radiation domination and grow like a when matter domination begins. The k_2 modes grow like a^2 until they enter the horizon during radiation domination. They then proceed to evolve like k_1 modes.

k_3 is referred to as the scale of equality. It only becomes sub-Hubble at equality, and therefore never oscillates. It grows like a^2 during radiation domination and a when matter begins to dominate. Modes of the form k_4 grow in a similar way.

The growth of these modes determines how large the perturbations grow. During the radiation dominated era, the perturbations remain small due to the decaying oscillations. Once radiation has decoupled, the perturbations are free to grow large. This is why linear perturbation theory is adequate to describe the evolution of structure for most of the universe's evolution. It is only when the perturbations reach a large enough size that non-linear theory more accurately describes the universe.

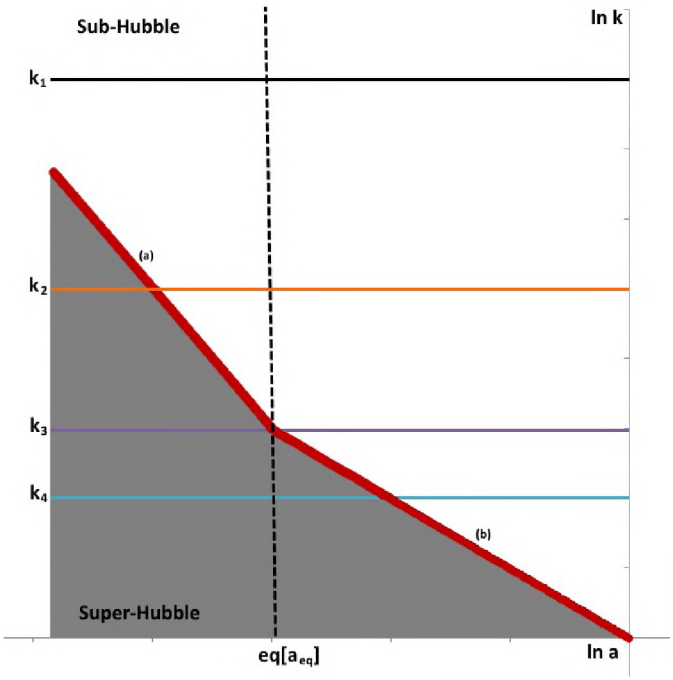

(a) Illustrates the time at which the modes k_i enter the Hubble radius. The red line represents the size of the comoving Hubble radius, where (a) $\mathcal{H} \propto a^{-1}$, and (b) $\mathcal{H} \propto a^{-1/2}$. The grey area represents scales larger than the comoving Hubble length.

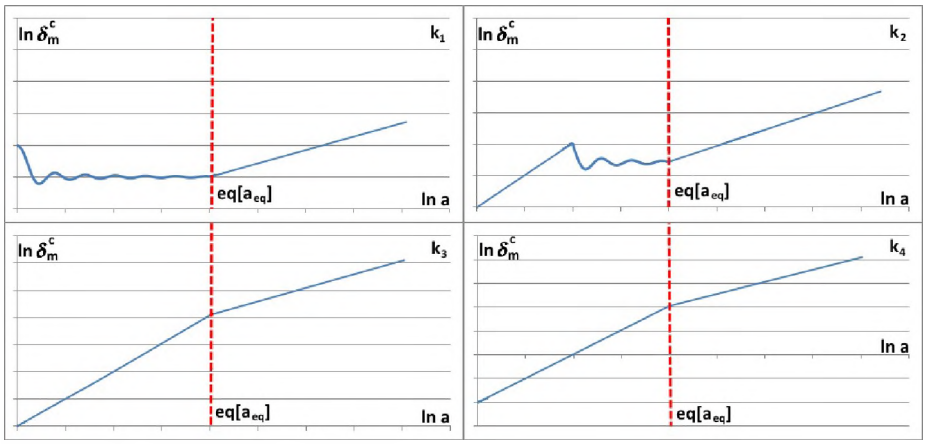

(b) The evolution of the density contrast for each mode from Figure (a).

Figure 3.2: Illustrates how modes behave as they enter the Hubble sphere. The comoving Hubble length grows like a^{-1} during radiation domination [left of figures] and $a^{-1/2}$ during matter domination [right of figures].

3.3.4 Growth of Small Scale Perturbations

During the radiation dominated era the amplitude of the density contrast shows oscillatory behaviour, as discussed above. This develops from the way radiation and matter are interacting. The gravitational force pulling the matter together opposes the pressure of the radiation pushing the matter apart. This is related to the concept of the Jeans length, defined as [3, 6, 1, 21]:

$$\lambda_J \equiv c_s \sqrt{\frac{\pi}{G_N \bar{\rho}}}, \tag{3.42}$$

where c_s is the speed of sound, G_N is the gravitational constant and $\bar{\rho}$ is the density. The Jeans length is the oscillation wavelength below which stable oscillations rather than gravitational collapse occurs.

This quantity appears in the propagation equation during radiation domination, see Section 6.4. Scales that are smaller than this value oscillate due to the pressure of the radiation. Larger scales do not overcome the gravitational force and undergo collapse.

During radiation domination $c_s = \frac{c}{\sqrt{3}}$ [21]. The comoving Hubble distance is given by:

$$\begin{aligned} ca^{-1}H^{-1} &= a\sqrt{\frac{3c^2}{8\pi G_N \bar{\rho}}} \\ &= \frac{3a}{2\pi\sqrt{2}}\lambda_J \\ &\approx \frac{a}{3}\lambda_J, \end{aligned}$$

where the Hubble distance is defined in Section 1.4. Since the comoving Jeans length, $a\lambda_J$, is larger than the observable universe during radiation domination, it is not surprising that the modes entering the horizon show oscillatory behaviour.

The Jeans length continues to grow with the universe until matter-radiation equality [21]. The radiation then decouples from the matter which removes the pressure force preventing gravitational collapse. The Jeans length shrinks. The perturbations, which have remained small due to the oscillation, are then free to grow.

The perturbations are initially small, $\delta \ll 1$, which is why linear growth can be assumed for most of matter domination. Once the perturbations grow in size the universe enters the non-linear regime, and deviations from the expected linear growth are observed.

The scales where the power spectrum becomes non-linear is $\lambda \approx 8h^{-1}$ Mpc [22] at the current epoch.

Chapter 4

Structure Formation: Non-linear Regime

4.1 Introduction to N-body Simulations

The models of the universe need to be verified by cosmologists. Einstein's prediction that light bends as it passes the Sun was testable in real life. Models of the universe cannot be tested in real life due to the scales of the experiment; see Chapter 1.

Numerical simulations, often referred to as N-body simulations, involve creating a grid that represents the system of interest on a computer. Models of how the particles interact over time are then written in code and the system is allowed to evolve in time. If the initial conditions are set according to observations, then the situation is effectively being recreating in a lab. The name N-body comes from the fact that the simulation could contain thousands of particles, i.e. N bodies.

The first application of numerical simulation to cosmology was in 1941, performed on an optical computer [23]. Digital computers were used in the early 1960s [20]. Simulations were relatively small, consisting of at most 100 particles [24].

As computers developed, cosmologists were able to create N-body simulations with a larger number of particles. In 1970, a cluster simulation of 300 particles was used to investigate whether a cluster of galaxies could have originated as a collapsing protocluster [25].

As discussed in Chapter 1, the study of cosmic structure formation is very important. This branch of cosmology gained particular attention in the 1980s due to several important developments:

- Several plausible physical models were proposed for dark matter [26, 27, 28] (such as massive neutrinos, hot dark matter, and cold dark matter).
- The scale-invariant Harrison-Zel'dovich spectrum of primordial fluctuations

in matter and radiation was shown to be produced by cosmic inflation [29].

- Thorough numerical calculations were done: [30] created a complete numerical understanding of linear, first-order density perturbations in a Friedmann-Lemaître cosmological model. [31] calculated the temporal evolution of the fluctuation spectrum by numerical integration to better understand dark matter and how it interacts.

- The theory of Gaussian random fields was developed and used in the generation of primordial density fields [32]. [33] and [34] investigated the effects of simulating Gaussian random fields with an arbitrary power spectrum.

- With the inclusion of grid-based algorithms, simulations with more than 10^5 particles became possible [20].

Due to the above advancements, the Cold Dark Matter (CDM) model was created and sophisticated tests were constructed to evaluate it. COBE (Cosmic Background Explorer) was used to measure the anisotropy in the cosmic microwave background radiation [35]. These observations presented a few problems with the model:

- The CDM model predicted more power on small scales than was observed [36].

- The velocity dispersion was too high on small-scales [37, 38].

- There were too many clusters of galaxies per unit volume [39].

The failure of the CDM model highlighted the complexity of the origin of structure. The model is being modified to improve its accuracy. These modifications involve including light massive neutrinos, including a cosmological constant, tilting the primordial spectrum, or including spatial curvature [20].

Regardless of the cosmological model, numerical simulations continue to be used. The machines have become more powerful and complex which has altered the method of the simulations. Studies continue to produce codes that are able to utilise this power and perform more accurate simulations.

Numerical simulations have been developed to study many areas of cosmology. Some examples include:

- Obtaining accurate predictions for the two-point correlation and power spectra of galaxy clusters [40].

- Studying galaxy cluster populations [41].

- Studying the large scale distribution of baryons [42].

- Testing a new method for constructing maps of temperature fluctuations on the CMB [43].

- Studying interacting galaxies [44].

- Large scale structure formation [45, 46, 47].

This thesis focuses on large-scale structure formation. There are two groups, the Virgo and DEUS consortiums, which have focused on this area of cosmology. What follows is a discussion of these groups and their codes.

4.2 The Virgo Consortium

The Virgo Consortium [48] is a collaboration of scientists that was founded in 1994. With access to the world class supercomputers COSMA4 and DiRAC-2, the Virgo Consortium can perform numerical simulations on a wide range of topics.

Some of the Virgo Consortium's projects are:

- The GIF project [49, 50] which was started to study the formation and evolution of galaxies in a cosmological context using semi-analytical galaxy formation models embedded in large high-resolution N-body simulations. The code used was Hydra [51].
- The Millennium Simulation [52] was the largest simulation of the formation of structure within the ΛCDM cosmology in 2005. The simulation was carried out using a specially adapted version of the publicly available code GADGET. The data was made available to the public and several publications have used this data. A list of publications can be found [53].
- EAGLE (Evolution and Assembly of GaLaxies and their Environments) [54] is a simulation aimed at understanding how galaxies form and evolve. It used the DiRAC-2 supercomputer to run and was performed by a heavily modified version of the public GADGET-2 simulation code [55].
- Copernicus Complexio (COCO) [48, 56, 57] is a dark matter only simulation. The project's goal is to resolve the formation and evolution of Milky Way sized haloes and their subhaloes. COCO simulates WDM (Warm Dark Matter) and CDM (Cold Dark Matter) cosmologies in order to observe the differences between them [48]. The code used is GADGET3, which is an updated version of GADGET2 [55].

The Virgo consortium make the data generated in their simulations free to the scientific community [58].

These projects may involve simulating different models. However, the codes used are very similar. Most use a version of GADGET, while the GIF project made use of Hydra. The mechanisms behind these codes is outlined in Section 4.4.

4.3 The DEUS Consortium

The DEUS Consortium [59] is another collaboration of scientists working on the DEUS (Dark Energy Universe Simulation) project. Their goal is to in-

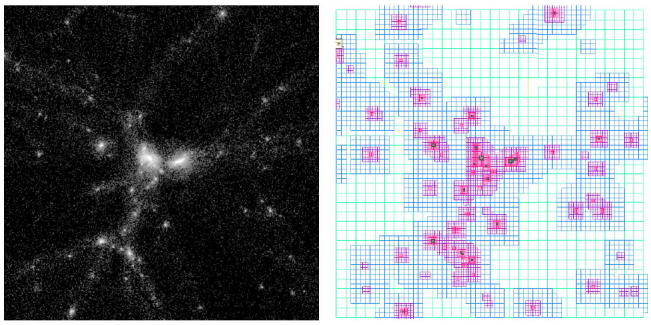

Figure 4.1: Left: The dark matter density field for two interacting halos. Right: The corresponding Adaptive Mesh Refinement (AMR) grid. [62]

vestigate the imprints of dark energy on cosmic structure formation through high-performance numerical simulations [59].

The DEUS project consists of two main components:

- DEUSS (Dark Energy Universe Simulation Series)
- DEUS - FUR (Dark Energy Universe Simulation Full Universe Run)

DEUSS is a large set of high performance cosmological DM simulations of realistic DE models with several billion particles and high spatial resolution.

DEUS-FUR was the first numerical N-body simulation of the full observable Universe [59].

Both projects were run by the code RAMSES_DEUS [59] which is a new version of the cosmological code RAMSES [60].

4.4 The Numerical Codes Used

Cosmologists have used many numerical codes to study the universe. The examples discussed in this section are

- Hydra [45, 51],
- GADGET [44, 55], and
- RAMSES_DEUS (paralleled version of RAMSES [60]).

Hydra is a parallel adaptive particle-particle-particle-mesh (P3M) code [45, 51]. The initial data is generated on a mesh grid and then evolved over time. The interparticle forces are split into two components: a long-range force which is calculated by a mesh-based method, and a short-range part which is summed directly from the contributions of nearby particles [61]. This code included a refinement grid for later evolutions to increase resolution of the galaxy clusters [51].

RAMSES is based on the Adaptive Mesh Refinement technique and has a tree-based data structure which allows for recursive grid refinements on a cell-by-cell basis ("Fully Threaded Tree") [60]. The N-body solver evolves particles using a Particle-Mesh (PM) method, while the Poisson equation is solved with a multi-grid technique [63].

This method is illustrated in Figure 4.1. The initial data is generated and enclosed inside a box, i.e. the root node of the tree. The box is then recursively divided until each particle is isolated inside its own box, i.e. the leaves of the tree [44, 55, 60]. The boxes that contain no particles do not have to be stored. This technique improves the memory usage and processing time/power needed to perform the simulation.

The codes GADGET-2 and -3 are hybrid codes. The long-range forces are computed using a particle-mesh method, while short-range forces are obtained using a hierarchical oct-tree algorithm [44, 55]. This particular heterogeneous architecture allows for a relatively easy follow-up of nested grids placed with increasing accuracy around the high-resolution region [44]. This results in proper long-range force accuracy throughout the box, while focusing most of the computational effort inside the high-resolution region of interest [44].

4.5 Initial Conditions

The initial data for structure formation is generated as the best fit for the highest precision observations of the time.

The Millennium simulation was carried out on a ΛCDM cosmology with a cubic region of $500\,h^{-1}$Mpc on a side with a spatial resolution of $5\,h^{-1}$kpc [52].

The cosmological parameters were based on the first-year data from WMAP. By 2012, these parameters were no longer consistent with improved parameter estimates based on more recent data [53], i.e. the WMAP-7yr data [64].

The DEUS-FUR simulation consists of a flat ΛCDM cosmology [47] best-fit to the WMAP-7yr data [64].

Gaussian initial conditions were generated with an optimised version of the code MPGRAFIC [65]. The box length is set to $21\,h^{-1}$ Gpc which encloses the horizon diameter in all three simulations, i.e. $d_H \approx 20.7h^{-1}$Gpc [47]. The initial redshift is set to $z_i = 106$ which is sufficiently high enough to avoid transient effects which occur in the case of a late start of the initial conditions using the Zel'dovich approximation [66, 67].

4.6 Call for Large Simulations

The design of a numerical simulation depends on the system being studied. The physical size of simulation depends on the physical size of the object or structure being observed. Consider the study of galaxy cluster formation: if a simulation of size 100 kpc was created then no conclusions could be drawn, since galaxy clusters are typically 2 to 10 Mpc in diameter [16].

Similarly, since the different models of the universe should only differ on scales larger than the Hubble distance, a study of galaxy filaments - typical length $\sim 100h^{-1}$Mpc [8, 9] - or imprints of dark energy [59] need to be performed on a grid the size of the observable universe.

All numerical simulations are created with a particular resolution, which determines the smallest scale. During linear evolution, all modes evolve independently. However, at late times non-linear effects are seen on small scales. If these scales are not present on the grid then coupling effects will not be seen, and an idealised representation of the evolution of the universe will be observed, as a result.

The finite size of cosmological simulations introduces two types of statistical errors [47]

1. It reduces the number of accessible modes, causing sample variance errors which dominate the error budget when probing scales near the size of the simulation box.

2. Modes that are larger than the simulation box length are absent [68], and since the gravitational coupling to these modes is missing, this results in a lower amplitude of the power spectrum [69].

Both problems can be handled either by averaging the spectra of a large number of different realisations (for example [70, 71]), or setting the simulation box length to be as large as possible. However, since observations are limited by the size of the cosmological horizon, statistical errors cannot be reduced to less than cosmic variance. Hence, by setting the box length of the DEUS-FUR simulations to the diameter of the observable universe the DEUS Consortium were guaranteed to derive cosmic variance limited (i.e. minimal sample variance) predictions for the matter power spectrum [47].

Carrying out the expansion in a box also imposes periodicity at the edges. However, these effects can be ignored as long as the box is much larger than the scales of interest [6]. Hence the need for simulations with a large number of grid points.

When conducting numerical simulations of isolated bodies or smaller regions of the observable universe it is necessary to correct for the aliasing effect. Aliasing and methods to prevent aliasing are discussed in Section 5.4.

4.7 Observational Results

The initial conditions of N-body simulations are set according to recent observational results in order to make comparisons and predictions of the numerical results.

The initial conditions can be measured by highly sensitive probes that can measure the slight variations in, for example, the CMB. There are other sources of structural information that can be observed in the Baryon Acoustic Oscillations (BAO) and galaxy surveys.

Table 4.1: WMAP 9 year results relevant to thesis

Parameter	Symbol	WMAP data
Curvature perturbations, $k_0 = 0.002\,\mathrm{Mpc}^{-1}$	$10^9 \triangle^2_{\mathcal{R}}$	2.41 ± 0.10
Scalar spectral index	n_s	0.972 ± 0.013
Age of the universe (Gyr)	t_0	13.74 ± 0.11
Hubble parameter, $H_0 = 100h\,\mathrm{kms}^{-1}\mathrm{Mpc}^{-1}$	H_0	70.0 ± 2.2
Redshift of matter-radiation equality	z_{eq}	3265^{+106}_{-105}

In this section these observable results are discussed, along with the implications on the thesis code and N-body codes in general.

4.7.1 Cosmic Microwave Background

The CMB was first discovered in 1965 [72]. It was assumed to be uniform until COBE DMR detected the 10^{-5} fluctuations in its temperature field across the sky [35]. These fluctuations illustrate the initial positions of matter at emission, which is important. The fluctuations were difficult to detect due to the size. This led to designing specialised probes.

One of the more recent probes was Wilkinson Microwave Anisotropy Probe (WMAP), which was launched in June 2001 [73]. This probe measured the differences in temperature of the CMB with changes in direction, anisotropy [73]. This probe measured the anisotropy with much finer detail and greater sensitivity than COBE [73] in order to detect smaller variations. The measurements were collected over multiple years with the following most recent results [74]:

These quantities are used in numerical simulations to determine the initial power spectrum of vacuum fluctuations. To guarantee that the thesis simulation takes place in the matter dominated era, the initial redshift must be greater than z_{eq}. This is why $z = 100$ is a common starting redshift.

4.7.2 Baryon Acoustic Oscillations

The Baryon Acoustic Oscillations (BAO) are another imprint observed in the oscillatory pattern of the matter power spectrum at later times [47]. Observations of the CMB have accurately determined the distance travelled by acoustic waves at decoupling. The distance these waves have travelled is called the sound horizon [13]. There is a slight increase in the chance of finding lumps of matter, and therefore galaxies, separated by the sound horizon distance.

WMAP is able to infer much more stringent bounds on the cosmological parameters [74]. In these observations, the BAO appear as a series of damped oscillations superimposed on the broadband shape of the matter power spectrum [47].

At lower redshifts, the non-linear clustering of matter induces deviations from the linear theory which are much harder to predict. The non-linearities

degrade the BAO pattern on the power spectrum and, if not accounted for, can alter the cosmological parameter inference [47].

BAO occur on relatively large scales ($\sim 100h^{-1}$ Mpc) [47] with a shape that depends on small-scale Lagrangian displacements $\sim 1 - 10h^{-1}$ Mpc [75]. Therefore, sample variance errors and a lack of large dynamical ranges will have a large impact on how accurate the numerical study will be.

Cosmic/sample variance is the error arising from trying the make predictions about scales outside the surveys size [76]. To minimise the cosmic variance, the sampling size must increase. Since the sampled area is the observable universe, there is a limit to how large the sample size can be [76].

The Dark Energy Universe Simulation - Full Universe Run (DEUS-FUR) [77] aimed to create a N-body simulation of size $21h^{-1}$ Gpc [47]. This size allowed them to develop cosmic variance limited predictions for the matter power spectrum.

4.8 Reason for Code Creation

With freely available codes and data for large-scale structure formation, it is becoming unnecessary to create new codes to investigate structure formation. The code GADGET can be edited to study many system of interest.

The drawback of using the existing codes is they require specialised hardware and particular coding knowledge, i.e. GADGET is written in ANSI C [55].

Although these codes construct the initial data in Fourier space, the time evolution is performed in physical-space. This thesis will discuss an alternative method, spectral method of evolution, discussed in Section 5. This is a method of evolution in Fourier space, which does not translate well to a tree based structure like GADGET.

Another focus of this thesis are the effects that aliasing has on Spectral methods. To investigate this effectively a new code needed to be developed.

Part II

Newtonian Spectral Code

Chapter 5

Principle of Spectral Methods

Numerical simulations and the methods for evolution were discussed in the previous part. This chapter presents a different method of evolving grids in time: *spectral methods*. Unlike conventional methods, which evolve data in real-space coordinates, spectral methods allow the evolution to be conducted in Fourier space. This is particularly useful since the initial data is set in Fourier space.

This chapter begins by discussing the basic theory behind spectral methods and how it can be used to perform the time evolution of the data on the grid. The effect of aliasing is then discussed with emphasis on the different types, how aliasing is created, and what can be done to limit the effects. This leads to the idea of filters. This chapter ends by illustrating the aliasing effects that could be present in the initial evolution, and how different filters can limit the effects.

5.1 Theory

To perform a numerical time evolution, it is necessary to calculate derivatives of the data on the grid with high accuracy, which is represented by a function. If the exact form of the function is known, the derivatives could be calculated manually. For complicated equations, it is often not possible to find an exact analytic solution. Therefore, it is necessary to develop a method for approximating the derivatives of data on a grid.

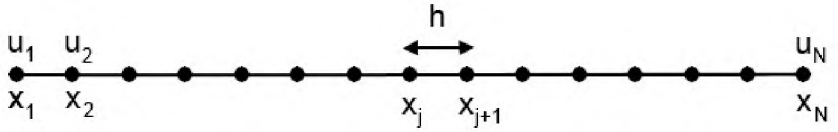

Figure 5.1: Grid of points $\{x_j\}$ and corresponding values $\{u(x_j)\}$ with grid-spacing h.

Consider the grid with the set of x values $\{x_j\}$ which correspond to values $\{u(x_j)\}$, where $j \in [1,\, N]$, Figure 5.1. Points are equally spaced with grid spacing $h = x_{j+1} - x_j$. The derivative, $u'(x_j)$, at point x_j can be approximated by calculating the slope between the points x_{j-1} and x_{j+1} by [78]:

$$D_2 u \;=\; \tfrac{u_{j+1}-u_{j-1}}{2h}\;, \tag{5.1}$$

where $u_{j-1} = u(x_{j-1})$ and $u_{j+1} = u(x_{j+1})$. The function $u'(x_j)$ is then calculated for each point. To minimise the amount of computing time, the above calculations can be done using a circulant matrix [78]:

$$\begin{pmatrix} w_1 \\ \\ \vdots \\ \\ w_N \end{pmatrix} = h^{-1} \begin{pmatrix} 0 & \frac{1}{2} & & & -\frac{1}{2} \\ -\frac{1}{2} & 0 & \ddots & & \\ & & \ddots & & \\ & & \ddots & 0 & \frac{1}{2} \\ \frac{1}{2} & & & -\frac{1}{2} & 0 \end{pmatrix} \begin{pmatrix} u_1 \\ \\ \vdots \\ \\ u_N \end{pmatrix}, \tag{5.2}$$

where $w_j = u'(x_j)$. All omitted entries in the circulant matrix (middle) are zero in order to calculate the derivative using equation (5.1). This results in $w_1 = h^{-1}\left[\frac{1}{2}u_2 - \frac{1}{2}u_N\right]$, $w_2 = h^{-1}\left[\frac{1}{2}u_3 - \frac{1}{2}u_1\right]$, etc.

When u is linear, equation (5.1) is sufficient to determine the derivative. However, if u is a sinusoidal wave and N is very small, then the approximated derivative will not be accurate. To improve the accuracy without increasing N, more points are included in the derivative equation. The following is an example of a fourth-order finite difference equation [78, 79]:

$$D_4 u \;=\; h^{-1}\left[\tfrac{1}{12}u_{j-2} - \tfrac{2}{3}u_{j-1} + \tfrac{2}{3}u_{j+1} - \tfrac{1}{12}u_{j+2}\right]\;. \tag{5.3}$$

Equation (5.3) has included two additional points and improved the accuracy. Including all available points should increase the accuracy to its limit. Spectral methods represent taking the limit of this process. Instead of concentrating on the interaction between individual points, the interactions between the constituent waves of u are considered.

In Fourier analysis [78], any function can be decomposed into a sum of sinusoidal waves. Consider a function $v(x)$, where $x \in \mathbb{R}$. The Fourier transform (FT) of $v(x)$ is the function $\hat{v}(k)$ which is defined as [79]:

$$\hat{v}(k) \equiv \frac{1}{(2\pi)^{n/2}} \int_{-\infty}^{\infty} e^{-ikx} v(x)\, d^n x, \qquad k \in \mathbb{R}, \tag{5.4}$$

where k is the wavenumber (alternatively referred to as the frequency or harmonic). The FT has an inverse which reconstructs $v(x)$ from $\hat{v}(k)$, defined as [79]:

$$v(x) \equiv \frac{1}{(2\pi)^{n/2}} \int_{-\infty}^{\infty} e^{ikx} \hat{v}(k)\, d^n k, \qquad x \in \mathbb{R}. \tag{5.5}$$

There are two conventions in defining the FT and inverse FT equations:

1. A factor of $\frac{1}{(2\pi)^n}$ is used in equation (5.4) and no factor is in equation (5.5) or vice versa, where n refers to the number of dimensions that the integral is calculated over (convention used in [7, 78]).

2. The factor of $\frac{1}{(2\pi)^n}$ is split over the two integrals to become $\frac{1}{(2\pi)^{n/2}}$, as in equation (5.4) & (5.5). (convention used in [6, 79]).

Fundamentally, any power of 2π can be used provided one equation has a factor of $(2\pi)^{1-a}$ while the other has $(2\pi)^{1+a}$. Option 2 has been adopted in this thesis to remain consistent with the initial data applied to the grid.

Equation (5.4) and (5.5) are defined on the whole $\mathbb{R}$ line. However, the function $u(x_j)$ is not defined by $x_j \in \mathbb{R}$. The grid points are contained on the infinite grid denoted by $h\mathbb{Z}$, where $x_j = jh$ for $j \in \mathbb{Z}$. Alterations to the real-space variable x place restrictions on the Fourier-space variable k.

The wavenumber k is now contained in a bounded interval of length $\frac{2\pi}{h}$, originally $k \in \mathbb{R}$. To maintain symmetry, the interval selected is $\left[-\frac{\pi}{h}, \frac{\pi}{h}\right]$. The relationship between x and k is now:

$$\begin{array}{ccccc} \text{Physical space} & : & \text{discrete, unbounded} & : & x \in h\mathbb{Z} \\ & & \updownarrow \quad \updownarrow & & \\ \text{Fourier space} & : & \text{bounded, continuous} & : & k \in \left[-\frac{\pi}{h}, \frac{\pi}{h}\right] \end{array}$$

A boundary is created for Fourier space to limit *aliasing* [78], which is discussed further in Section 5.4.

By bounding the wavenumbers a new transform is generated: the *semi-discrete Fourier transform* (sDFT) and its *inverse* (isDFT):

$$\hat{v}(k) = \frac{h}{(2\pi)^{1/2}} \sum_{j=-\infty}^{\infty} e^{-ikx_j} v_j, \qquad k \in \left[-\frac{\pi}{h}, \frac{\pi}{h}\right], \tag{5.6}$$

$$v_j = \frac{1}{(2\pi)^{1/2}} \int_{-\pi/h}^{\pi/h} e^{ikx_j} \hat{v}(k)\, dk, \qquad j \in \mathbb{Z}, \tag{5.7}$$

where $v(x)$ has become $v_j = v(x_j)$ which is discrete.

Fourier analysis has supplied a new perspective of the function on the grid. It is now possible to describe the process of differentiating in Fourier space, i.e. *spectral differentiation.*

Let $w(x_j) = \frac{\partial}{\partial x_j} v(x_j)$. Using equation (5.7):

$$\begin{aligned} w(x_j) = \frac{\partial}{\partial x_j} v(x_j) &= \frac{\partial}{\partial x_j} \frac{1}{(2\pi)^{1/2}} \int_{-\pi/h}^{\pi/h} e^{ikx_j} \hat{v}(k)\, dk \\ &= \frac{1}{(2\pi)^{1/2}} \int_{-\pi/h}^{\pi/h} ike^{ikx_j} \hat{v}(k)\, dk. \end{aligned}$$

This implies that $w(x_j)$ is the isDFT of $ik\hat{v}(k)$, which means,

$$\hat{w}(k) = ik\hat{v}(k). \tag{5.8}$$

In Chapter 3, the initial data for the cosmological problem was determined in the Fourier domain from the power spectrum of initial perturbations of the

vacuum field. A transformation to physical space is then performed to evolve the data in time. After the data has been evolved in time. a Fourier transform is performed. The power spectrum can then be calculated in Fourier space.

In performing the differentiation and time evolution in Fourier space. less processing power and time is required. This is only the case when the evolution equations contain linear terms. If there are non-linear terms, a conversion to real space is necessary to eliminate performing computationally intensive convolutions in Fourier space.

5.2 Boundary Conditions

In cosmology, space is homogeneous and isotropic on large scales, discussed in Chapter 3. Due to the homogeneous nature of the universe, it is unnecessary to recreate all of space on the grid. It is a reasonable approximation to create a portion of space and then extrapolate for the remainder of the universe. This extrapolation consists of setting up periodic boundaries.

The periodic boundaries modify the grid described in Section 5.1. The infinite grid is bounded to a smaller interval, in this case $(0,\ 2\pi]$. The physical length scales are mapped onto this numerical grid by including the appropriate scaling factors.

The grid is then partitioned into N points, as shown in Figure 5.2, with spacing:

$$h \quad = \quad \frac{2\pi}{N} \ . \tag{5.9}$$

To simplify the discussion, N is restricted to an even integer throughout this thesis. This preference is made to ensure the middle element in the array, $a\left[\frac{n}{2}\right]$ where $n = \text{length}\,(a)$, returned by fft.fft represents the spectra for both the positive and negative Nyquist frequency [80].

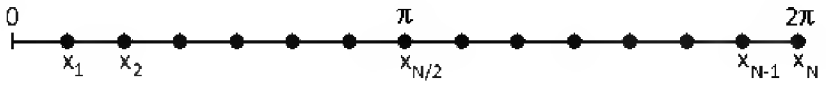

Figure 5.2: Grid of points $\{x_j\}$ where $x_j \in (0,\ 2\pi]$ and $j \in [1,\ N]$

Consider the grid from the previous section, where the x values were discrete, which limited k to the interval $\left[-\frac{\pi}{h},\ \frac{\pi}{h}\right]$. Using equation (5.9), the bounds can be written in terms of the number of points, $\left[-\frac{N}{2},\ \frac{N}{2}\right]$. The k values were bounded due to the discretisation of x; since x is now bounded, the k values need to be discretized. Physical space is contained in the interval $(0,\ 2\pi]$, where the available periodic waves have wavelength, λ:

$$\lambda \quad = \quad \frac{2\pi}{l} \ , \ l \in \mathbb{Z}^{+}. \tag{5.10}$$

This implies that the wavenumbers allowed on the grid must be integers, since:

$$k \;=\; \tfrac{2\pi}{\lambda} \;=\; l \;. \tag{5.11}$$

The relationship between physical space and Fourier space is:

$$\begin{array}{rcccl} \text{Physical space} & : & \text{discrete, bounded} & : & x \in \{h, 2h, \ldots, 2\pi - h, 2\pi\} \\ & & \updownarrow \quad\quad \updownarrow & & \\ \text{Fourier space} & : & \text{bounded, discrete} & : & k \in \left\{-\tfrac{N}{2}+1, -\tfrac{N}{2}+2, \ldots, \tfrac{N}{2}\right\} \end{array}$$

The sDFT is defined for an infinite grid. To perform the FT on the newly bounded grid, the sDFT is replaced by the *discrete Fourier transform* (DFT) [78]. When the new bounds are taken into consideration, the DFT and its inverse are defined by [78]:

$$\hat{v}_k \;=\; \frac{h}{(2\pi)^{1/2}} \sum_{j=1}^{N} e^{-ikx_j} v_j, \qquad k = -\frac{N}{2}+1, \ldots, \frac{N}{2}, \tag{5.12}$$

$$v_j \;=\; \frac{1}{(2\pi)^{1/2}} \sum_{k=-N/2+1}^{N/2} e^{ikx_j} \hat{v}_k, \qquad j = 1, \ldots, N. \tag{5.13}$$

Note that equation (5.13) is a summation over the integers $k \in \left[-\frac{N}{2}+1,\ \frac{N}{2}\right]$, which is asymmetric. Evaluating the x-derivative of the term with the highest wavenumber results in $\left(i\frac{N}{2}\right) e^{iNx/2}$. The derivative should be zero since $e^{iNx/2}$ represents a real, sawtooth wave on the grid. This is due to the asymmetric treatment of the largest wavenumber by equation (5.13). This treatment can be fixed by defining $\hat{v}_{-N/2} = \hat{v}_{N/2}$ and replacing (5.13) by:

$$v_j = \frac{1}{(2\pi)^{1/2}} {\sum_{k=-N/2}^{N/2}}' e^{ikx_j} \hat{v}_k, \qquad j = 1, \ldots, N, \tag{5.14}$$

where the prime indicates that the terms $k = \pm\frac{N}{2}$ are multiplied by $\frac{1}{2}$.

Since the proper form of the FT and its inverse on the grid have been derived, the derivative of the wave in Fourier space can now be determined. Equations (5.12) and (5.13) suggest the following algorithm for determining the derivative for a function v, defined at a set of discrete points in physical space:

1. Given v, compute $\hat{v}$ using the DFT, equation (5.12)
2. Define $\hat{w}_k = ik\hat{v}_k$ for all $k \in \left[-\frac{N}{2}+1,\ \frac{N}{2}-1\right]$, set $\hat{w}_{N/2} = 0$
3. Compute w from $\hat{w}$ using the inverse DFT, equation (5.13)

The resulting values of w give the pseudo-spectral approximation to the derivative of v evaluated on the grid.

The DFT can be calculated using the Fast Fourier Transform (FFT). Algorithms for which are contained in the numpy.fft library for python [80].

5.3 Time Evolution

In the previous sections, the grid was initialised and a method for calculating the derivative of a function on the grid was developed. This method is necessary to evolve the function in time.

There are many time evolution methods that have different orders of accuracy and different stability regions. The method this thesis uses for time evolution is a fourth-order Runge-Kutta (RK) method.

The principle idea of the RK method was proposed by C. Runge [81] and later developed by W. Kutta [82] and others. This class of methods can be implemented as either *explicit* [79] or *implicit* [83] schemes.

Explicit methods calculate the state of the system in the future by using the current state of the system. Alternatively, implicit methods determine the solution by solving an equation involving the current and future states. Implicit methods are necessary for stiff equations due to the unbounded stability regions. However, implicit methods are more complicated and processor intensive, depending on the number of steps involved, than explicit methods. This is why the explicit RK method is used in this thesis.

To define the RK method, let y_0 be the initial state of the system i.e. $y(t_0) = y_0$. The time-step size $\triangle t$ is chosen and y_0 is evolved in time to get y_1 by the following formula [79, 84]:

$$y_1 = y_0 + \triangle t\left(b_1 k_1 + \ldots + b_s k_s\right), \tag{5.15}$$

where the quantities k_j are calculated by:

$$\begin{aligned} k_1 &= f(x_0,\, y_0), \\ k_2 &= f(x_0 + c_2\triangle t,\, y_0 + \triangle t a_{21} k_1), \\ k_3 &= f(x_0 + c_3\triangle t,\, y_0 + \triangle t(a_{31}k_1 + a_{32}k_2)), \\ &\vdots \\ k_s &= f(x_0 + c_s\triangle t,\, y_0 + \triangle t(a_{s1}k_1 + \ldots + a_{s,s-1}k_{s-1})), \end{aligned} \tag{5.16}$$

where $a_{21}, a_{31}, a_{32}, \ldots, a_{s1}, a_{s2}, \ldots, a_{s,s-1}, b_1, \ldots, b_s, c_2, \ldots, c_s$ are real coefficients and s is an integer that represents the number of stages. The above is referred to as an s-stage explicit RK method. The following condition must hold for all RK methods [84]:

$$\sum_{j=1}^{s-1} a_{ij} = c_i \ . \tag{5.17}$$

The Butcher tableau for this method is [84]:

$$
\begin{array}{c|ccccc}
0 & & & & & \\
c_2 & a_{21} & & & & \\
c_3 & a_{31} & a_{32} & & & \\
\vdots & \vdots & \vdots & \ddots & & \\
c_s & a_{s1} & a_{s2} & \cdots & a_{s,s-1} & \\
\hline
 & b_1 & b_2 & \cdots & b_{s-1} & b_s
\end{array}
$$

The RK method used in this thesis is the fourth-order RK method. This has the additional condition:

$$\sum_{j=1}^{s} b_j \quad = \quad 1. \tag{5.18}$$

The coefficients can be calculated to get the fourth-order RK Butcher tableau [79, 84]:

$$
\begin{array}{c|cccc}
1 & & & & \\
\frac{1}{2} & \frac{1}{2} & & & \\
\frac{1}{2} & 0 & \frac{1}{2} & & \\
1 & 0 & 0 & 1 & \\
\hline
 & \frac{1}{6} & \frac{2}{6} & \frac{2}{6} & \frac{1}{6}
\end{array}
$$

That correspond to the following equations [79]:

$$
\begin{aligned}
v^1 &= u^i, \\
v^2 &= u^i + \tfrac{1}{2}\triangle t f\left(v^1, t_i\right), \\
v^3 &= u^i + \tfrac{1}{2}\triangle t f\left(v^2, t_i + \tfrac{\triangle t}{2}\right), \\
v^4 &= u^i + \triangle t f\left(v^3, t_i + \tfrac{\triangle t}{2}\right), \\
u^{i+1} &= u^i + \tfrac{1}{6}\triangle t\left[f\left(v^1, t_i\right) + 2f\left(v^2, t_i + \tfrac{\triangle t}{2}\right) + 2f\left(v^3, t_i + \tfrac{\triangle t}{2}\right) + f\left(v^4, t_i + \triangle t\right)\right],
\end{aligned}
$$

where u^i is the function on the grid and u^{i+1} is the function at the new time.

For a hyperbolic equation, the Courant-Friedrichs-Lewy (CFL) [85, 86] condition indicates that the time-step, $\triangle t$, and grid size, $\triangle x_i$, need to satisfy [87]:

$$C \quad = \quad \triangle t \sum_{i=1}^{n} \frac{u_{x_i}}{\triangle x_i} \quad \leq \quad C_{\max} \ . \tag{5.19}$$

To maintain stability. The variables in equation (5.19) are:

- C, the Courant number.
- u_{x_i}, the magnitude of the characteristic velocity in the dimension x_i.

The value of $C_{\max}$ changes depending on whether the method used is explicit or implicit. The actual value of $C_{\max}$, which allows for stable evolutions, may depend on the form of the equation - though $C_{\max} = 1$ is a typical guideline suggested by the theory of explicit methods [87].

5.4 Aliasing

As mentioned in Section 5.1, spectral methods require the use of discrete Fourier Transforms (DFT). The particular implementation of the DFT used is the Fast Fourier Transform (FFT). The FFT method requires the real-space and Fourier space coordinates to be discrete, with the real-space signal assumed to be periodic. The discretisation of real-space implies the Fourier coordinates are bounded.

Thus, the spatial resolution limits the physical frequencies that can be represented by the method. Aside from the inevitable loss of information, sampling artifacts such as aliasing and Gibbs ringing are introduced by the discretisation. To limit the effects of the sampling artifacts, filters are applied to the data. These filters can cause problems if applied incorrectly.

This section is organised as follows: The discretisation of a signal is discussed in more detail. The different sampling artifacts, created by discretisation, are identified and discussed. Finally, occurrences of sampling artifacts are discussed in the context of numerical simulations, which create initial data - instead of sampling physical data and putting it onto the grid.

5.4.1 Discretising Real-space

Signals can be represented or approximated by sums of trigonometric functions, e.g sine. These sums are referred to as a Fourier series [88]. The signals from distant galaxies are more accurately described by an infinite Fourier series [89].

When these signals are observed by scientific equipment the signal recorded is a *sampled signal*. The signal is sampled at regular intervals, as shown in Figure 5.3 (a).

Let $f(x)$ be the original signal travelling in space and $g(x)$ be the sampled signal. Since the signal can be represented as a scaled Dirac impulse function [89], the act of sampling a signal is equivalent to multiplying by a Dirac comb of the form:

$$\Pi(x) = \sum_{j=-\infty}^{\infty} \delta^D(x - j\triangle x), \tag{5.20}$$

where $\triangle x$ is the grid spacing. Therefore the sampled signal is $g(x) = \Pi(x) \cdot f(x)$.

Spectral methods involve a transformation to Fourier space. By using the definition that the product of two functions in real-space yields a convolution in Fourier space [89], the Fourier transform of the sampled signal $\hat{g}(k)$ is:

$$\hat{g}(k) = \left(\hat{\Pi} \star \hat{f}\right)(k), \tag{5.21}$$

where $\star$ represents a convolution. The function $\hat{\Pi}(k)$ can be shown to be a Dirac comb of the form [89]:

$$\hat{\Pi}(k) = \frac{1}{\triangle x} \sum_{j=-\infty}^{\infty} \delta^D \left(k - j \frac{1}{\triangle x} \right). \tag{5.22}$$

Therefore the convolution becomes [89]:

$$\begin{aligned} \hat{g}(k) &= \left(\hat{\Pi} \star \hat{f} \right)(k) \\ &= \frac{1}{\triangle x} \int_{-\infty}^{\infty} \sum_{j=-\infty}^{\infty} \delta^D \left(k' - j \frac{1}{\triangle x} \right) \hat{f}(k - k')\, dk' \\ &= \frac{1}{\triangle x} \sum_{j=-\infty}^{\infty} \hat{f} \left(k - j \frac{1}{\triangle x} \right). \end{aligned} \tag{5.23}$$

An example of the above multiplication and convolution is displayed in Figure 5.3. Figure 5.3 (a) shows the multiplication between $f(x)$ and the Dirac comb while Figure 5.3 (b) shows the convolution in Fourier space. It is clear that the signal $\hat{g}(k)$ is a periodic version of the original signal $\hat{f}(k)$. In this case the original spectrum is still present and can be obtained using a filter, which would remove the superfluous data. Both the periodic behaviour of the sampled signal and the period between the repetitions have different aliasing effects.

Aliasing is a signal processing term used to describe errors caused by an insufficient sampling rate. There are two types, characterised by the frequency terms that are effected: *low-frequency aliasing* and *high-frequency aliasing.* These terms are discussed below.

5.4.2 Low-frequency Aliasing

The previous subsection showed how the Fourier transform of the sampled function, $\hat{g}(k)$, is a periodic version of the original signal, $\hat{f}(k)$. The spectrum is no longer a one-to-one function. Consider two wavenumbers: q is located at the right peak in the centre part of the spectrum and p is located at the right peak in the repeat to the right. Both points correspond to the same value in the spectrum. Therefore, on the grid, q and p look identical.

To illustrate a specific example, Figure 5.4 shows the aliasing of two functions $\sin 2\pi x$ and $\sin 10\pi x$ on the interval $[-1, 1]$. The dots indicate the restriction of sampling with grid spacing $\triangle x = 0.25$. The dots correspond to points where the two functions are identical. This phenomenon is referred to as *low-frequency aliasing.* This name refers to the process of mapping high-frequency terms to low-frequency values.

In order to remove this aliasing effect, the frequencies are bounded. The bounding process removes the superfluous data from the spectrum and guarantees the uniqueness of waves on the grid. An interval centred on zero is chosen

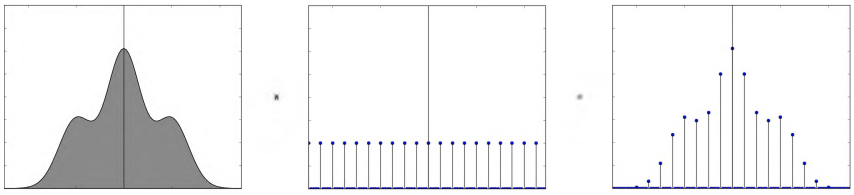

(a) Original signal multiplied by the Dirac comb in real-space

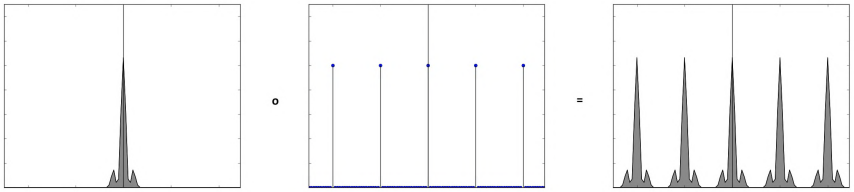

(b) The signal convolved with the Dirac comb in Fourier space

Figure 5.3: Multiplication and convolution with the sampling function

[78], with an upper bound referred to as the Nyquist frequency or folding frequency, n_s:

$$k\epsilon\left[-n_s, \cdots, -1, 0, 1, \cdots, n_s\right]. \tag{5.24}$$

The Nyquist frequency is half the sampling rate of the signal [89] which corresponds to $\frac{N}{2}$ in the code [78, 90].

The result is that the spectrum of the original signal is reconstructed. In Figure 5.3 (b), the signals do not overlap, and therefore the bounding process can remove the repetitions without altering the original signal. This is not always possible and results in high-frequency aliasing.

5.4.3 High-frequency Aliasing

As seen in Subsection 5.4.1, $\hat{g}(k)$ is a periodic version of $\hat{f}(k)$. The period of $\hat{g}(k)$ is determined by the Dirac comb, $\hat{\Pi}(k)$, with a grid spacing $\triangle x$. If $\triangle x$ decreases the period of $\hat{g}(k)$ increases, spreading the repetitions further apart. Alternatively, if $\triangle x$ increases, i.e. fewer points are sampled, the period of $\hat{g}(k)$ decreases. If the period of $\hat{g}(k)$ decreases sufficiently, the repetitions begin to overlap.

Filters can be used to remove the repetitions in the spectra. These filters are applied with a cut-off frequency equal to the Nyquist frequency, n_s. If the original spectrum does not overlap with the repetitions, the original signal can be obtained. However, if overlap does occur, the signal will be altered.

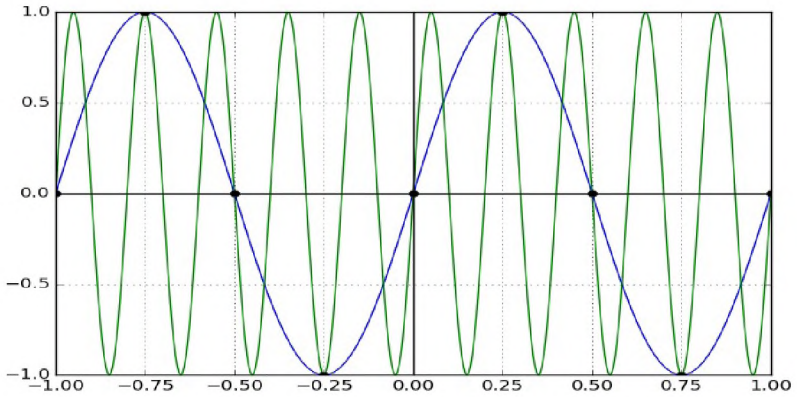

Figure 5.4: Demonstrating low-frequency alias

Alteration of the signal's spectrum occurs when there is insufficient space between signals. Figure 5.5 illustrates a spectrum where: a) there is sufficient space between signals, and b) where signals overlap. The Nyquist frequency, n_s, is the cut-off frequency of the filter. If the filter is applied to a) only the centre spectrum will remain, this is the original spectrum. Applying the filter to b) will result in a spectrum that increases as k approaches n_s. The high-frequency terms of the repetitions have altered the centre spectrum by the amount in the blue area. Since this type of aliasing affects high-frequency terms first, it will be referred to as *high-frequency aliasing.*

The most direct way of removing this aliasing effect is to decrease $\triangle x$. The repetitions will get further apart and remove the overlap. However, this is only effective if, at a sufficiently large frequency, the spectra is zero. Even if the spectra does reach zero, it might be impractical to create such a large grid. The process of pre-filtering is used in this case [89, 90]. The filter is applied before sampling to ensure the spectra reaches zero at a lower frequency. In this case, the reconstructed signal is not synonymous with the original signal, but is the reconstructed pre-filter signal.

5.4.4 The Effect of Convolutions and the 2/3 Rule

The above aliasing effects have been discussed strictly in transformations from a physical signal to a sampled signal. However, aliasing effects can occur due to the evolution methods used. Evolving data in numerical simulations requires using a time evolution method, for example Runge-Kutta, with situation specific evolution equations.

The evolution equations consist of linear and non-linear terms. The linear terms contain a multiplication between a field and a time-dependent value. In Fourier space it remains a multiplication since the time-dependent variable

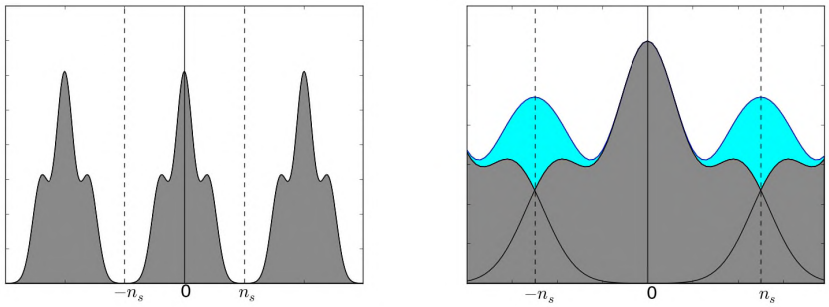

(a) Sampled signal with no distortion (b) Sampled signal with aliasing

Figure 5.5: Adequately (left) and poorly (right) sampled signals

remains the same after the application of a Fourier transform. However, the non-linear terms are characterised by a real-space multiplication of two fields. When this operation is converted to Fourier space it becomes a convolution. Since the fields contain the same number of harmonics, the resulting field has twice as many harmonics.

To justify the inclusion of more harmonics, consider the convolution of signal $f(k)$ (top hat) with signal $g(k)$ (triangle), in Figure 5.6 (a) and (b) respectively. The convolution takes the form:

$$(f \star g)(k) = \int_{-\infty}^{\infty} f(k')\, g(k - k')\, dk', \tag{5.25}$$

where $g(k - k')$ represents a reversed $g(k')$ signal that has been shifted along the k-axis, Figure 5.6 c) illustrates both functions during the convolution. The value of $(f \star g)(k)$ for each k is obtained by shifting the function $g(k - k')$ to the desired k and calculating the area common to both functions. Figure 5.6 (d) demonstrates a point where a common area exists (red). The area is calculated and plotted on the convolution result, arrow in Figure 5.6 e). Notice that $f(k)$ and $g(k)$ have domain $k \in [-1,\ 1]$ while the result of the convolution has domain $k \in [-2,\ 2]$. This indicates the inclusion of more harmonics, specifically double the original harmonics.

The inclusion of more harmonics is not allowed since the signal has already been filtered to remove low-frequency and high-frequency aliasing. As a result, the extra harmonics are aliased to low-frequency values.

This aliasing effect was experienced by |91| in a general circulation model. The simulation ran for a few days before the energy grew too large. The time-step and grid-spacing were greatly decreased in an attempt to correct the problem, however no noticeable improvements were made |88|.

It was noted that waves of $|k| = \frac{N}{2}$ were appearing shortly before the code failed |91|. This implied the excess energy was building up at high frequencies,

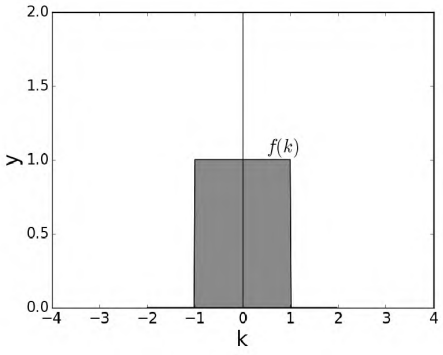

(a) Signal $f\,(k)$

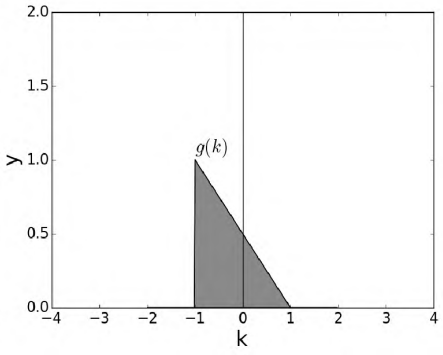

(b) Signal $g\,(k)$

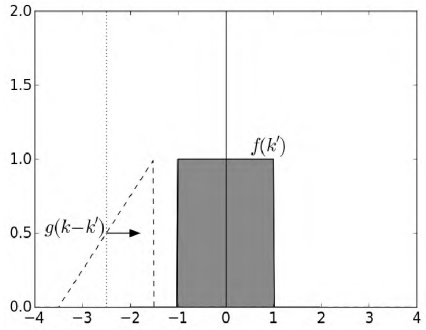

(c) Convolution in progress, $k = -2.5$

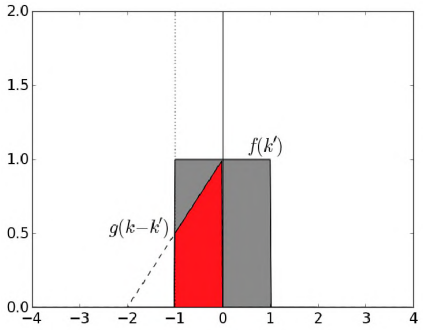

(d) The overlapping area

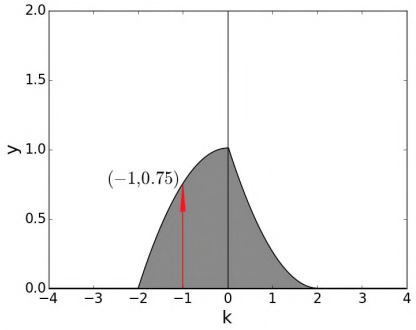

(e) The result of the convolution

Figure 5.6: The process of convolving two signals with the same size along the k-axis

near the aliasing limit [88]. To rectify the situation a filter was applied which removed half the harmonics. This solution allowed the simulation to evolve correctly and removed the energy build up.

This was successful however it was not necessarily the best method to remove aliasing. Two distinct methods have been developed since then, *phase-shift de-aliasing* [92] and *zero-padding* [93].

Phase-shift de-aliasing is accomplished by taking the difference between the FFT-based convolution and a convolution based on the shifted FFT [94]. This method is rarely used since it is always more processing intensive than zero-padding [95].

Zero-padding, as the name suggests, involves including points that are intentionally set to zero. There are two methods of achieving this, *padding* [96] and *truncation* [93].

Padding involves extending the numerical grid for the convolution process. After the convolution, the large grid is filtered to only contain harmonics present on the smaller grid. The results are then mapped onto the smaller grid and the time evolution method is continued.

The convolution can be done in two ways: explicit padding [96] or implicit padding [97]. Explicit padding creates the larger grid in memory and does the summations over points that are zero, which requires more processing time and memory. Implicit padding removes the need to explicitly create the larger grid and performs the calculations directly on the small grid, which requires less memory space and allows higher-dimensional convolutions to be calculated more efficiently.

An alternative method, truncation, removes wavenumbers that are affected by aliasing on the grid. Originally half the wavenumbers were removed [91]. However, it is sufficient to remove a third of the harmonics [93]. This became known as *Orszag's two-thirds rule* [88], which states that since the aliased wavenumbers must be multiples of $2K$, all wavenumber interactions larger than $\frac{2}{3}K$ are only aliased to wavenumbers that are removed [93].

To clarify, Figure 5.7 demonstrates a polar coordinate representation of wavenumbers k, where the circle represents $k \in [-K,\, K]$. The range $k \in \left[-\frac{2}{3}K,\, \frac{2}{3}K\right]$ is unaffected by the filters while wavenumbers $|k| > \frac{2}{3}K$ are set to zero at the end of every time-step.

The non-linear terms expand the range of wavenumbers to $k \in \left[-\frac{4}{3}K,\, \frac{4}{3}K\right]$ as a result of the convolution, discussed above. Since $|k| \in \left[\frac{2}{3}K,\, K\right]$ are removed by the filter automatically, the wavenumbers of concern are $|k| \in \left[K,\, \frac{4}{3}K\right]$.

The red arrow in Figure 5.7 represents $k = \frac{4}{3}K$. It is clear from the figure that this wavenumber is include in the range $k \in \left[-K,\, -\frac{2}{3}K\right]$, the bottom grey area. Points in this grey area are filtered out. Similarly, the green arrow represents $k = -\frac{4}{3}K$, which falls in the upper grey area and gets filtered away. In this way the points where aliasing can occur are not retained at the end of the time-step.

One might test a different cut-off frequency, for example $|k| = \frac{3}{4}K$. The range of wavenumbers after the convolution would be $k \in \left[\frac{6}{4}K,\, -\frac{6}{4}K\right]$. Wavenum-

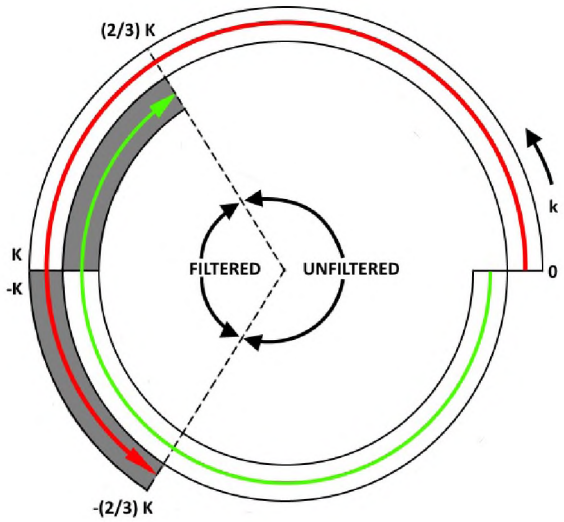

Figure 5.7: The "Aliasing Wheel" adapted from [88]. The arrows represent two aliased wavenumbers: $\frac{4}{3}K$ (red) and $-\frac{4}{3}K$ (green)

bers in $k \in \left[K,\ \frac{6}{4}K\right]$ would alias to $k \in \left[-K,\ -\frac{1}{2}K\right]$. As a result wavenumbers in $k \in \left[-\frac{3}{4}K,\ -\frac{1}{2}K\right]$ will develop aliasing errors due to the overlap. Therefore, the filter cut-off at $\frac{2}{3}K$ is necessary to maintain accuracy.

5.4.5 Gibbs Ringing

In Subsections 5.4.2-5.4.4 different types of aliasing effects were discussed. The common solution to each aliasing effect is to apply a low-pass filter. This filter, sometimes referred to as the "all-or-nothing" filter [88] or Boxcar filter, takes the form:

$$a_k \rightarrow [\text{filtered}] = \begin{cases} a_k & |k| < m, \\ 0 & |k| \geq m, \end{cases} \tag{5.26}$$

where m is the cut-off frequency. In Subsection 5.4.2 and 5.4.3 m is set to $\frac{N}{2}$, while Subsection 5.4.4 has set $m = \frac{N}{3}$.

This type of filter allows frequencies below the cut-off frequency through without modification and frequencies above the cut-off are set to zero. Signals that reach zero before the cut-off frequency remain unchanged. A discontinuity is created when the spectra does not reach zero before the cut-off. This discontinuity implies a truncation of the Fourier series, which can create oscillations in real-space known as the Gibbs Phenomenon.

The Gibbs phenomenon, discovered by Henry Wilbraham and rediscovered by J. Willard Gibbs [98], describes the way the Fourier series of a piecewise

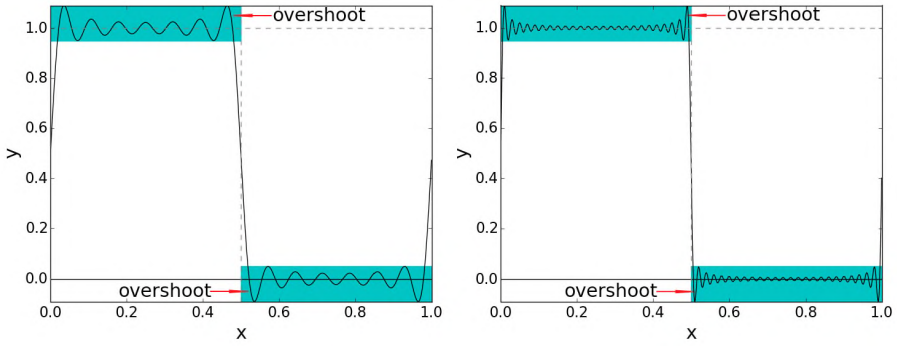

(a) Seven harmonics (b) Twenty-five harmonics

Figure 5.8: The Gibbs phenomenon on a square wave. The oscillations are contained in the shaded areas and the overshoots on either side of the discontinuity are labelled.

continuously differentiable periodic function behaves at a jump discontinuity [98]. The behaviour is characterised by an overshoot and Gibbs oscillations on either side of the discontinuity.

The overshoot and oscillations are shown in Figure 5.8, where the functions are square waves with seven harmonics (a) and twenty-five harmonics (b). As x moves further away from the discontinuity, the amplitude of the oscillations decreases. The figures show that including more harmonics creates more oscillations with smaller amplitudes however the amplitude of the initial overshoot does not change.

In order to understand the Gibbs phenomenon, the cause of the oscillations needs to be identified. The filter truncates the Fourier series by performing a multiplication between the original signal and the boxcar filter. To understand the effect in real-space, the inverse Fourier transform of the boxcar filter must be taken into consideration. This follows from the correlation between multiplication in Fourier space and convolutions in real-space, see Subsection 5.4.1.

The inverse Fourier transform of boxcar filter is the sinc function, Figure 5.9:

$$\text{Sinc} \equiv \frac{\sin ax}{ax}, \tag{5.27}$$

where $a = \pi$ corresponds to the normalized sinc function and $x = 0$ is defined to be 1. The convolution with the sinc function creates the oscillations observed.

As mentioned above, the amplitude of the overshoot is not affected by the number of harmonics included. The overshoot amount is related to the height of the discontinuity [88]. Since the height of the overshoot is the result of the convolution between the square wave and sinc function in real-space, the height of the overshoot is given by [99]:

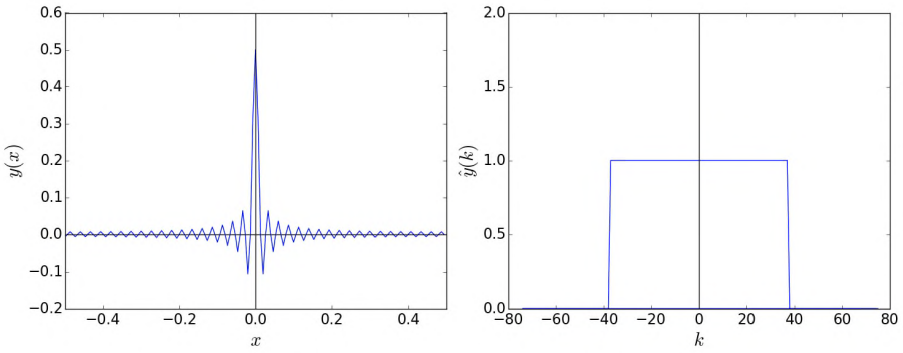

(a) The Sinc function (b) The boxcar filter

Figure 5.9: The Fourier transform pair

$$\frac{J}{\pi}\int_0^{\pi}\frac{\sin t}{t}dt + \frac{J}{2} \quad = \quad J * 1.0894908106 \ , \tag{5.28}$$

where J is the total height of the jump of the square wave in Figure 5.8, i.e. $J = 1$. The factor of $\frac{J}{2}$ is included to account for the vertical translation of the square wave in Figure 5.8 from the wave discussed in [99]. This value implies there will always be an overshoot of $\pm 9\%$ the height of the discontinuity.

The oscillations on either side of the discontinuity are referred to as Gibbs rings or ripples depending on whether they exist in real-space or Fourier space, respectively. Since the sinc function and boxcar filter are a Fourier transform pair, filtering real-space will create oscillations in Fourier space in a similar way.

To limit or remove the Gibbs oscillations that result from the use of a boxcar filter, smoother filters have been suggested to remove the discontinuity, these filters are discussed below.

5.4.6 Filters

As discussed above, the boxcar filter with $k_c = \frac{N}{3}$ removes the high-frequency aliasing however it may introduce Gibbs ripples.

Smoother filters have been suggested in order to remove the Gibbs effect. One such filter is suggested in [1], illustrated in Figure 5.10(a) (blue line). The filter, exponential filter, is:

$$F\left(\mathbf{k}\right) \quad = \quad \exp\left\{-36 * \left(\frac{2\left|\mathbf{k}\right|}{N}\right)^{36}\right\}. \tag{5.29}$$

This filter does not create a discontinuity, unlike the boxcar filter. However, zero is not reached before the cut-off frequency for the 2/3 rule. Therefore, Gibbs ripples may be reduced at the expense of introducing high-frequency aliasing.

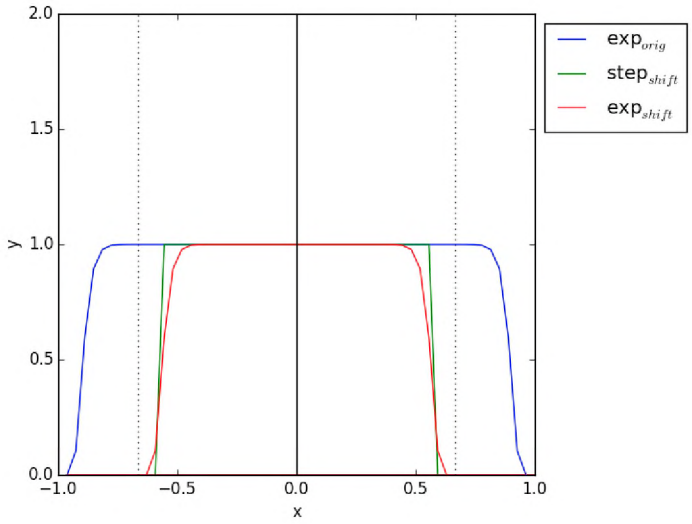

(a) The filters used. The dotted lines represent the 2/3 rule line. We can see that the suggested filter goes into this area. The green top_hat has been included to compare whether there is a noticeable Gibbs effect. Blue is the suggested filter [1].

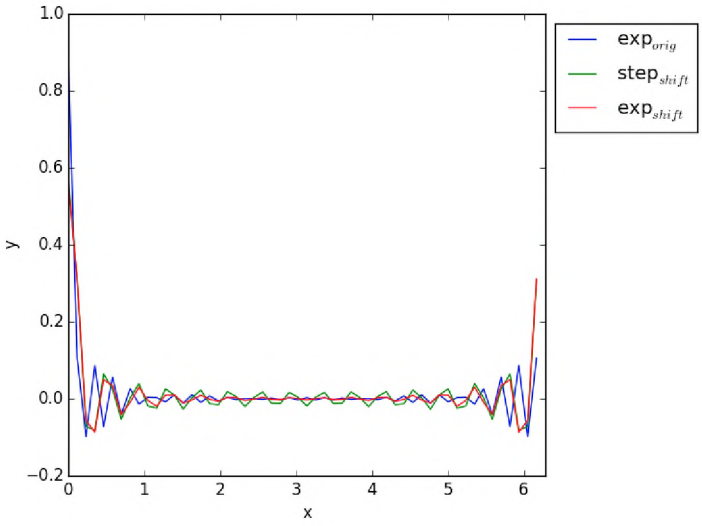

(b) The different filters in real space. Oscillations decrease faster for the smooth filters which suggests less Gibbs ripples will be created during the convolution.

Figure 5.10: Filters

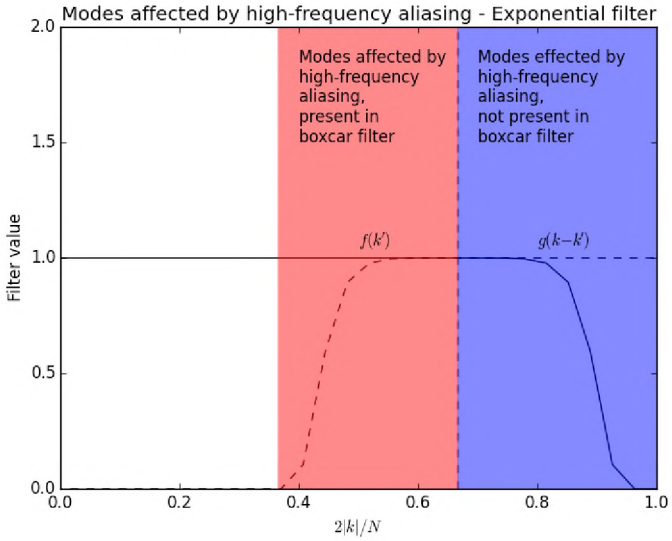

Figure 5.11: The modes where high-frequency aliasing will occur if the exponential filter is used.

Figure 5.11 illustrates the modes where high-frequency aliasing will occur between two fields that have been filtered by the exponential filter. The modes in blue ($\frac{2|\mathbf{k}|}{N} > \frac{2}{3}$) do not appear in the boxcar filter, therefore a comparison for those modes is not possible. However, the modes in red ($\frac{10}{27} \leq \frac{2|\mathbf{k}|}{N} \leq \frac{2}{3}$) are common to both filters and will experience high-frequency aliasing when using the exponential filter.

To investigate whether Gibbs ripples are reduced by the shape of the filter, high-frequency aliasing must not be occurring. A shifted filter is suggested:

$$F(\mathbf{k}) = \exp\left\{-36 * \left(\frac{2|\mathbf{k}|}{N} + \frac{1}{3}\right)^{36}\right\}. \tag{5.30}$$

Which becomes zero at $\frac{2|\mathbf{k}|}{N} \approx \frac{2}{3}$, see Figure 5.10(a) (red line). This filter is then compared to a boxcar filter with $k_c = \frac{5N}{18}$. This cut-off frequency is chosen to coincide with the frequency where the shifted exp filter has a value of 0.5 i.e $\frac{k_c}{N/2} = 0.562748886$.

Multiplying by these filters in Fourier space corresponds to a convolution in real space. Figure 5.10(b) illustrates what the inverse Fourier transform of each filter looks like. All the filters show oscillations near the peak however the oscillations die away faster for the two exponential filters. This suggests that the Gibbs oscillations will be much smaller than the boxcar filter.

5.4.7 Identifying Sampling Artifacts in the Simulation

The initial data for the gravitational potential $\hat{\Phi}$ in the simulation was generated with power spectrum according to equation (3.12) and (3.13) with n_s and $\mathcal{P}_0$ given by equation (3.14) and (3.15) respectively, see Section 3.1.

The gravitational potential is related to the density contrast δ via the Poisson equation (second derivative), and the velocity $\mathbf{v}$ via one derivative, see Chapter 6 for full relationship.

As shown in Section 5.1, a derivative in real-space corresponds to a multiplication by the wavenumber k in Fourier space. Therefore:

$$\begin{aligned} \hat{\delta} &\propto |k|^2 \hat{\Phi}, \\ \hat{v}_i &\propto ik_i \hat{\Phi}. \end{aligned}$$

These relationships will be derived in Section 6.7. The power spectrum of δ and v_i are related to $P_\Phi(k)$ via [100]:

$$\begin{aligned} P_\Phi(k) &\sim k^{-4} P_\delta(k), \\ P_\Phi(k) &\sim k^{-2} P_{v_i}(k). \end{aligned}$$

Since $\mathcal{P}_\Phi(k)$ is relatively flat, $n_s - 1 \approx 0$, the variance of $\hat{\Phi}$, σ_n^2, decreases with increasing $|k|$, see Figure 5.12. Due to the relationship in equation (3.12), the variance of $\hat{\Phi}$ is $\sigma_n^2 \propto k^{-3}$.

Figure 5.13(a) illustrates how $\hat{\Phi}$ decreases with increasing $|k|$. The same behaviour can be seen in $\hat{v}_x$, Figure 5.13(b), where the expected variance is $\sigma_n^2 \propto k^{-1}$. The density contrast increases as $|k|$ increases, Figure 5.13c). This is consistent with $\sigma_n^2 \propto k$.

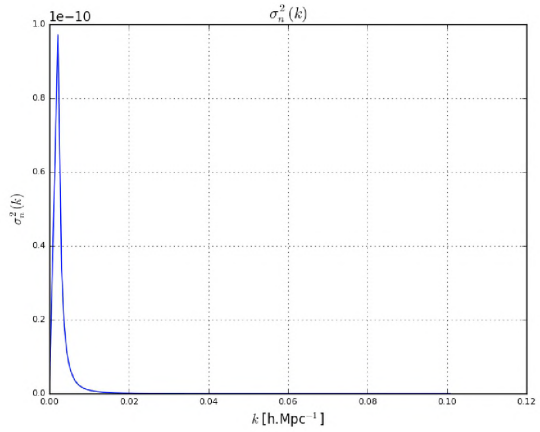

Figure 5.12: The variance of $\hat{\Phi}$ with respect to $|k|$

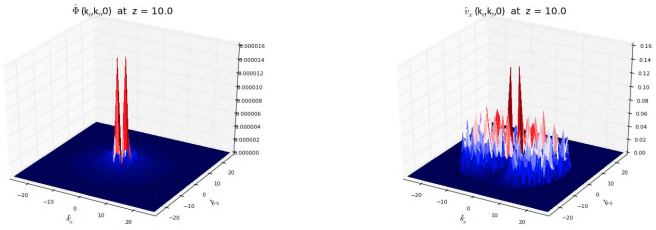

(a) A typical slice of the gravitational potential $\hat{\Phi}$

(b) A typical slice of the velocity $\hat{v}_x$

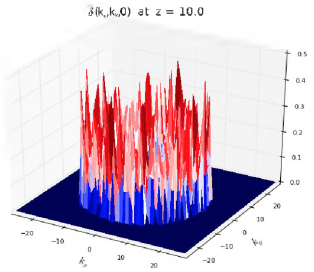

(c) A typical slice of the density contrast $\hat{\delta}$

Figure 5.13: These figures illustrate how the gravitational potential and velocity experience a general decrease as $|k|$ increases whereas the density contrast increases as $|k|$ increases. Graphs drawn where $L = 4166\,\text{Mpc}$

Since $\hat{\Phi}$ and $\hat{v}_i$ decrease with increasing $|k|$ and are of order $\mathcal{O}(\hat{\Phi}, \hat{v}_i) \lesssim 10^{-5}$ at $L = 4166$ Mpc, a boxcar filter will not cause a large discontinuity at the cut-off frequency.

The density contrast increases with increasing $|k|$. When the box is $L = 4166$ Mpc the maximum is $\mathcal{O}(\hat{\Phi}, \hat{v}_i) = 10^{-4}$. Although the maximum is still $\ll 1$ the general trend is increasing, therefore a discontinuity is created when using a boxcar filter. This could cause Gibbs rippling if non-linear terms are included in the evolution.

If a curved filter is used it could decrease aliasing effects. If, however, the filter has non-zero high frequency contributions (into the 2/3's region) it will introduce high-frequency aliasing.

Chapter 6

Evolution

The universe is modelled as a fluid [6, 16] to ensure the field varies smoothly as a function of position. This is true if it is assumed that topological defects play no role in structure formation. Present theories suggest that, after inflation, the fluid was a gas except during phase transitions. Once bounded structures (for example galaxies) form due to gravitational interaction, the structures are seen as *particles* of the cosmic *gas*, as described in Chapter 3. The cosmic fluid concept only applies after smoothing on a comoving scale containing many particles.

To observe the development of structures in the universe, an understanding of the motion of the particles needs to be discussed. The motion described will be in terms of different *observers*. An observer refers to a hypothetical person present in a particular reference frame that can observe different quantities. An important type of observer is the *comoving observer*. Who exists in the reference frame of the expanding universe and subsequently moves with the expanding universe, including the effect of its inhomogeneities. Comoving observers measure zero momentum density at their position and any other observer will see them moving with the flow of energy [6].

This chapter begins with describing the velocity of observers in the universe and the evolution of the perturbations using Newton's theory of gravity. In Section 6.3, it is shown that by using the fluid model Newton and Einstein theories agree. The rest of the chapter describes how the evolution equations can be written in comoving and then dimensionless coordinates. Finally the system of equations is linearised to determine the solutions, which are converted to Fourier space for convenience.

6.1 Peculiar Velocity

It is important to determine the velocity of a comoving observer. The observer will appear to move differently depending on the reference frame adopted. Let the 3-vector $\mathbf{r}$ describe the physical spatial positions, with respect to some ar-

bitrary specified origin, and t describe the universal time coordinate.

The velocity of the comoving observer is called the fluid velocity,

$$\mathbf{v}(\mathbf{x},t) = \frac{d\mathbf{r}}{dt}, \tag{6.1}$$

where $\mathbf{r}$ is time-dependent. In an unperturbed universe, the vector $\mathbf{r}$ is:

$$\mathbf{r}(t) = a(t)\,\mathbf{x}, \tag{6.2}$$

where $a(t)$ is the expansion factor and $\mathbf{x}$ is a fixed position vector. This position vector describes the position of a *uniform-expansion observer*, i.e. an observer that would observe galaxies expanding uniformly about their position. Uniform-expansion observers all measure the same value for Hubble's constant.

In an unperturbed universe the position of a comoving observer would be equation (6.2). However, when perturbations are taken into account the position of the comoving observer is given by:

$$\mathbf{r}(t) = a(t)\,\mathbf{x}(t), \tag{6.3}$$

where $\mathbf{x}$ is now time-dependent.

To determine the scale factor $a(t)$, and hence the Hubble parameter $H(t)$, the scales are chosen to be large enough for the perturbations to have a negligible effect, i.e. $\mathbf{r}$ very large. However, this result cannot be exact since the Newtonian viewpoint breaks down at $r \gtrsim H^{-1}$ [6].

To determine the total velocity of a comoving observer the derivative of equation (6.3) is obtained:

$$\begin{aligned}\mathbf{v}(\mathbf{x},t) &= H(t)\,\mathbf{r} + a(t)\,\frac{d\mathbf{x}}{dt} \\ &= \mathbf{v}_{rec} + \mathbf{u}(\mathbf{x},t),\end{aligned} \tag{6.4}$$

where $\mathbf{v}_{rec}$, recession velocity, is the velocity of the expanding universe and $\mathbf{u}$ is the peculiar velocity (or proper velocity [3]) of the object with respect to a uniform-expansion observer.

6.2 The Euler Equations

The compressible Euler equations describe the motion of a fluid with density, ρ, and pressure, P [101]:

$$\frac{\partial\rho}{\partial t} + \nabla\cdot(\rho\mathbf{v}) = 0, \tag{6.5}$$

$$\frac{\partial\mathbf{v}}{\partial t} + (\mathbf{v}\cdot\nabla)\,\mathbf{v} = -\frac{1}{\rho}\nabla P - \nabla\Psi, \tag{6.6}$$

where ρ is the density of the fluid, $\mathbf{v}$ is the velocity of the particles in the fluid, P is the pressure of the fluid, Ψ is the gravitational potential and ∇ is the gradient operator. These equations describe the Newtonian laws of *conservation of mass* and *momentum*, respectively. In cosmology the equations are referred to as the continuity and Euler equations, respectively.

The gradient operator ∇ is defined differently depending on the coordinate system used. In general rectangular coordinates, the gradient of a vector field $\mathbf{f} = (u,\ v,\ w)$ is defined as [2]:

$$\nabla f \equiv \frac{\partial f}{\partial u}\mathbf{e}^u + \frac{\partial f}{\partial v}\mathbf{e}^v + \frac{\partial f}{\partial w}\mathbf{e}^w, \tag{6.7}$$

where $\mathbf{e}$ are the basis coordinate vectors given by for example $\mathbf{e}^u = \frac{\partial u}{\partial x}$ [2]. When using curvilinear coordinates, or on a curved manifold, the gradient becomes the covariant derivative given by [2]:

$$\check{\nabla} f = \frac{\partial f}{\partial x^i}\mathbf{e}^i + \Gamma^i_{ij} f^j, \tag{6.8}$$

where Einstein summation notation [2] is used such that the first term is ∇f and the second term is a sum of terms containing the Christoffel symbol Γ. The Christoffel symbol [2] is defined as $\Gamma^a_{bc} = \frac{1}{2} g^{ad}\left(\partial_b g_{dc} + \partial_c g_{bd} - \partial_d g_{bc}\right)$ where g_{ij} are the components of the metric tensor, see Section 1.1.

6.3 Einstein to Euler

Equations (6.5) and (6.6) were derived by Euler in 1757 [101], many years before General Relativity was conceived by Einstein (in 1915) [5]. To ensure these equations still hold on intergalactic scales, a derivation from general relativity must be performed. To begin, consider the Einstein equation from Section 1.1, equation (1.7). This equation illustrates how the geometry of spacetime (left) is coupled to the arrangement of matter (right). For a perfect fluid, $T_{\mu\nu}$ is defined as [2]:

$$T^{\mu\nu} \equiv \left(\rho + \frac{P}{c^2}\right) u^\mu u^\nu - p\eta^{\mu\nu}, \tag{6.9}$$

where ρ is the rest density, P is the pressure, u^μ and u^ν are 4-velocities, and $\eta^{\mu\nu}$ is the metric of a flat spacetime, $\eta^{\mu\nu} \equiv [1, -1, -1, -1]$. The 4-velocity is defined as [2]:

$$\begin{aligned} u^\mu &\equiv \gamma v^\mu \\ &= \gamma\left(c, \mathbf{v}\right), \end{aligned} \tag{6.10}$$

where $\mathbf{v}$ is the particle's 3-velocity and $\gamma = \left(1 - \frac{|\mathbf{v}|^2}{c^2}\right)^{-1/2}$. Therefore $T^{\mu\nu}$ is symmetric and possesses one divergence, $T^{\mu\nu}_{,\mu}$. Since $T^{\mu\nu}_{,\mu} = G^{\mu\nu}_{,\mu}$ and $G^{\mu\nu}_{,\mu} = 0$, from the Bianchi identities [2, 3], the divergence is zero .

Taking the divergence of equation (6.9) gives [2]:

$$\begin{aligned} \left(\rho u^\mu\right)_{,\mu} u^\nu + \rho u^\mu u^\nu_{,\mu} + \left(\frac{P}{c^2}\right) u^\mu_{,\mu} u^\nu \\ + \left(\frac{P}{c^2}\right) u^\mu u^\nu_{,\mu} + c^{-2} P_{,\mu} u^\mu u^\nu - P_{,\mu}\eta^{\mu\nu} &= 0. \end{aligned} \tag{6.11}$$

Which can be projected along u_ν to obtain:

$$\left(\rho u^\mu\right)_{,\mu} + \left(\frac{P}{c^2}\right) u^\mu_{,\mu} = 0. \tag{6.12}$$

Which simplifies equation (6.11) to:

$$\left(\rho + \frac{P}{c^2}\right) u^\nu_{,\mu} u^\mu = \left(\eta^{\mu\nu} - c^{-2} u^\mu u^\nu\right) P_{,\mu}. \tag{6.13}$$

Note that contracting equation (6.11) with u_ν is equivalent to taking the zeroth component in an instantaneous rest system of the fluid at the point in question.

Equations (6.12) and (6.13) are the continuity and Euler equations from Section 6.2 before taking the classical limit. To take the limit, the fluid is assumed to be slow moving, $\frac{v}{c} \ll 1$, and experiences small pressures, $\frac{P}{c^2} \ll \rho$. Equation (6.12) reduces to:

$$\left(\rho u^\mu\right)_{,\mu} = 0. \tag{6.14}$$

Using equation (6.10) and $\gamma = 1$, due to slow moving particles, equation (6.14) becomes:

$$\begin{aligned} \left(\rho c\right)_{,0} + \left(\rho v^i\right)_{,i} &= 0 \\ \frac{\partial \rho}{\partial t} + \nabla \cdot (\rho \mathbf{v}) &= 0. \end{aligned} \tag{6.15}$$

Which is the continuity equation of Section 6.2.

Equation (6.13) reduces to:

$$\rho v^\nu_{,\mu} v^\mu = \left(\eta^{\mu\nu} - c^{-2} v^\mu v^\nu\right) P_{,\mu}. \tag{6.16}$$

In terms of v^μ. Since $c^{-2} v^\mu v^\nu = [1, 0, 0, 0]$, the right-hand side reduces the above to:

$$\rho v^i_{,\mu} v^\mu = -\delta^{ji} P_{,j}, \tag{6.17}$$

where $\delta^{ij} = 1$ when $i = j$ and zero otherwise. In 3-vector notation:

$$\begin{aligned} \rho \left[\frac{\partial v^i}{\partial t} + v^i_{,j} v^j \right] &= -P \\ \rho \left[\frac{\partial}{\partial t} + \mathbf{v} \cdot \nabla \right] \mathbf{v} &= -\nabla P. \end{aligned} \tag{6.18}$$

Which is the Euler equation of Section 6.2. Therefore, assuming the fluid is slow moving and experiences small pressure, the Einstein equation and stress-energy tensor lead to the continuity and Euler equations.

6.4 The Linearised Equations

The universe is modelled as a gas with mass density $\rho(\mathbf{x}, t)$ and pressure given by the equation of state in equation (3.21) [3]. Remember that pressure-less matter is described by $w = 0$ and radiation is described by $w = \frac{1}{3}$. For a barotropic fluid $w = c_s^2$ [3], so that w is a constant.

The gravitational potential, Ψ, satisfies the Poisson equation:

$$\triangle \Psi = 4\pi G \rho. \tag{6.19}$$

In Section 1.3, the different phases of the universe are discussed. Recall that, after the Big Bang and inflation, there are two major epochs [6]: the *matter-dominated* era and the *radiation-dominated* era.

Matter-radiation equality marks the time at which the density of matter equals the density of radiation. The ratio of the densities at the current epoch is [64, 102]:

$$\frac{\rho_{m,0}}{\rho_{r,0}} = \frac{\Omega_{m,0}}{\Omega_{r,0}} \approx \frac{0.259}{8.24 \times 10^{-5}} \approx 3140,$$

However, in the past, the ratio of matter density to energy density was:

$$\frac{\rho_m(a)}{\rho_r(a)} = \frac{\rho_{m,0}}{\rho_{r,0}} a.$$

Thus, the moment of radiation-matter equality took place when the scale factor was:

$$a_{rm} = \frac{\rho_{m,0}}{\rho_{r,0}} \approx \frac{1}{3140} \approx 3.18 \times 10^{-4},$$

and the redshift was [19]:

$$z = 3139.$$

Therefore, the redshift range of interest, $100 \leq z \leq 0$, is in the matter-dominated era.

The following sections discuss the evolution equations for the matter-dominated era and the radiation-dominated era. The derivation of the matter-domination equations is discussed first despite occurring after radiation-domination, see Section 1.3. This is due to their relevance for this thesis, i.e. redshift range on interest is $100 \leq z \leq 0$.

6.4.1 Matter-dominated Era

The universe is currently in the matter-domination era, discussed in Section 1.3. During this era, the average particle density in the universe is so low it can effectively be treated as a collisionless dust and the pressure term in equation (6.6) can be removed. To determine the evolution of structure as seen by a comoving observer, the evolution equations (6.5), (6.6) and (6.19) are re-written in comoving coordinates:

$$\frac{\partial \rho}{\partial t} + \frac{1}{a}\nabla_{\breve{\mathbf{x}}} \cdot (\rho \mathbf{u}) + 3\frac{\dot{a}}{a}\rho = 0, \tag{6.20}$$

$$\frac{\partial \mathbf{u}}{\partial t} + \frac{1}{a}(\mathbf{u} \cdot \nabla_{\breve{\mathbf{x}}})\,\mathbf{u} + \frac{\dot{a}}{a}\mathbf{u} = -\frac{1}{a}\nabla_{\breve{\mathbf{x}}}\Phi, \tag{6.21}$$

$$\triangle_{\breve{\mathbf{x}}}\Phi = 4\pi G a^2 (\rho - \bar{\rho}), \tag{6.22}$$

where $a(t)$ is the scale factor, $\mathbf{u}$ is the peculiar velocity, $\breve{\mathbf{x}}$ is the comoving space coordinate, Φ is the peculiar potential and $\bar{\rho}$ is the space-averaged background density. The above equations were derived in Appendix D.1.

The density can be decomposed into a time-dependent component and a component that depends on space and time:

$$\rho(\mathbf{x}, t) \equiv \bar{\rho}(t)\,[1 + \delta(\mathbf{x}, t)], \tag{6.23}$$

where δ is called the density contrast [3], and describes the perturbation of the local density from $\bar{\rho}$. In terms of the density contrast, the continuity and Poisson equations become:

$$\frac{\partial \delta}{\partial t} + \frac{1}{a}\nabla \cdot [(1 + \delta)\,\mathbf{u}] = 0, \tag{6.24}$$

$$\triangle\Phi = 4\pi G a^2 \bar{\rho}\delta, \tag{6.25}$$

as derived in Appendix D.2.

There exists a solution for the density contrast and peculiar velocity [3, 6] in the linear regime. To obtain this solution, the system is linearised by assuming the density perturbations are small,

$$\delta \ll 1 \quad ; \quad (\mathbf{u} \cdot \nabla)\,\mathbf{u} \approx 0. \tag{6.26}$$

The linearised evolution equations are:

$$\frac{\partial \mathbf{u}}{\partial t} + \frac{\dot{a}}{a}\mathbf{u} = -\frac{1}{a}\nabla\Phi, \tag{6.27}$$

$$\frac{\partial \delta}{\partial t} + \frac{1}{a}\nabla \cdot \mathbf{u} = 0, \tag{6.28}$$

By combining equations (6.27) and (6.28), the evolution equation for the density contrast during matter-domination is:

$$\frac{\partial^2 \delta}{\partial t^2} + 2\frac{\dot{a}}{a}\frac{\partial \delta}{\partial t} - 4\pi G\bar{\rho}\delta = 0. \tag{6.29}$$

The derivation of the evolution equations for the density contrast in the matter-dominated era can be found in Appendix D.3.

6.4.2 Radiation-dominated Era

In the radiation-dominated era, the energy densities were much higher and thus the fluid pressure is nonnegligible. Following the derivation in Appendix D.4, the evolution equation for the density contrast in this era is:

$$\frac{\partial^2 \delta}{\partial t^2} + 2\frac{\dot{a}}{a}\frac{\partial \delta}{\partial t} \quad -4\pi G\bar{\rho}\delta = \frac{c_s^2}{a^2}\triangle\delta, \tag{6.30}$$

where c_s is the speed of sound in the fluid. This equation is referred to as the *propagation equation* [3, 16].

By decomposing the perturbations into plane waves, i.e.

$$\delta(\mathbf{x}, t) = C\exp\left[i\left(\omega t - \mathbf{k}\cdot\mathbf{x}\right)\right]. \tag{6.31}$$

The dispersion relation is determined to be [3, 16]:

$$\omega^2 = \frac{c_s^2 k^2}{a^2} - 4\pi G\bar{\rho}. \tag{6.32}$$

Which has three solution types:

- $\omega^2 > 0$ - an oscillating solution.

- $\omega^2 < 0$ - a growing or decaying mode.
- $\omega^2 = 0$ - the Jeans limit.

The dispersion relation is commonly written in terms of the wavelength, λ,

$$\omega^2 = 4\pi^2 c_s^2 \left[\frac{1}{\lambda^2} - \frac{1}{\lambda_J^2}\right], \tag{6.33}$$

where λ_J is the Jeans length defined in Section 1.3 as equation (3.42).

6.5 Conversion to Dimensionless Units

All evolution equations thus far have been described using physical units. The simulated grid, as discussed in Chapter 5, is created with a length of 2π. Thus the evolution equations must be defined in terms of these variables instead of physical variables.

Variables with a $\sim$ represent the variables in physical units. The variable L will represent the largest physical scale observable on the grid at t_0 in Mpc.

The transformation between physical and coded space coordinates is:

$$\tilde{\mathbf{x}} = \frac{L}{2\pi}\mathbf{x}. \tag{6.34}$$

The wavenumbers are transformed using the relation:

$$\tilde{k} = \frac{2\pi}{L}k. \tag{6.35}$$

The power spectrum, discussed in Chapter 3, was defined in terms of the physical wavenumber and the variance. In terms of coded variables it becomes:

$$\begin{aligned} \mathcal{P}_\Phi\left(\tilde{k}\right) &= \left(\frac{L}{2\pi}\right)^3 4\pi\tilde{k}^3 \left\langle \left|\Phi_{\tilde{k}}\right|^2 \right\rangle \\ \mathcal{P}_\Phi\left(k\right) &= 8\pi k^3 \sigma^2. \end{aligned} \tag{6.36}$$

The power law equation, equation (3.13), remains unchanged due to the dimensionless nature of the power spectrum, i.e. regardless of whether k or $\tilde{k}$ is used the dimensions will be cancelled by the pivot wavenumber k_*.

In Subsection 3.2, the time dependent variables were expressed in terms of a dimensionless time coordinate τ, via:

$$\tau = \tfrac{t}{t_0} \quad \Longrightarrow \quad \tfrac{dt}{d\tau} = t_0 = \tfrac{2}{3}H_0^{-1} \ . \tag{6.37}$$

In what follows, a derivative with respect to cosmic time, t, is represented by a dot, for example $\dot{\mathbf{x}}$, and a derivative with respect to dimensionless time, τ, is represented by a dash, for example $\mathbf{x}'$. Derivatives with respect to spacial coordinates can also be converted using:

$$\frac{d\tilde{\mathbf{x}}}{d\mathbf{x}} = \frac{L}{2\pi}. \tag{6.38}$$

The proper velocity:

$$\tilde{\mathbf{u}}(\mathbf{x},t) = a\frac{d\tilde{\mathbf{x}}}{dt} \quad \Longrightarrow \quad \tilde{\mathbf{u}} = \frac{d\tau}{dt}\frac{d\tilde{\mathbf{x}}}{d\mathbf{x}}\mathbf{u} = \frac{3LH_0}{4\pi}\mathbf{u}\ , \tag{6.39}$$

where $\mathbf{u}$ is chosen so that $\mathbf{u} = a\frac{d\mathbf{x}}{d\tau}$. Using all the above conversions the Poisson, continuity and Euler equations become:

$$\delta = \frac{2}{3}\left(\frac{2\pi c}{LH_0}\right)^2 \tau^{2/3}\triangle\Phi, \tag{6.40}$$

$$\delta' + \frac{1}{a}\nabla\left[(1+\delta)\,\mathbf{u}\right] = 0, \tag{6.41}$$

$$\mathbf{u}' + \frac{2}{3}\frac{1}{\tau}\mathbf{u} + \frac{1}{a}\left(\mathbf{u}\cdot\nabla_{\mathbf{x}}\right)\mathbf{u} = -\frac{1}{a}\left(\frac{4\pi c}{3LH_0}\right)^2 \nabla_{\mathbf{x}}\Phi, \tag{6.42}$$

where factors of c have been included to guarantee the physical units are cancelled.

6.6 Growing Mode

In Section 6.4, the propagation equation for the density contrast was derived for two epochs. Using this equation particular solutions for the density contrast can be derived.

Recall that during the matter domination era, the propagation equation is:

$$\frac{\partial^2\delta}{\partial t^2} + 2\frac{\dot{a}}{a}\frac{\partial\delta}{\partial t} - 4\pi G\bar{\rho}\delta = 0. \tag{6.43}$$

In a flat universe with no cosmological constant, the Friedmann equation implies that $6\pi G\bar{\rho}t^2 = 1$ during the matter-dominated era (since $a \propto t^{2/3}$) [3]. Therefore the mean matter density can be expressed as $4\pi G\rho_m(t) = \frac{3}{2}H^2\Omega_m(t)$ [3] and equation (6.43) becomes:

$$\ddot{\delta} + 2H(t)\,\dot{\delta} - \frac{3}{2}H^2(t)\,\Omega_m(t)\,\delta = 0. \tag{6.44}$$

The above equation is a second-order linear differential equation involving only time. The solution is of the form [3]:

$$\delta(\mathbf{x},t) = D_+(t)\,\varepsilon_+(\mathbf{x}) + D_-(t)\,\varepsilon_-(\mathbf{x}), \tag{6.45}$$

where the functions $\varepsilon_\pm(\mathbf{x})$ correspond to the initial density field, D_+ is the growing mode and D_- is the decaying mode. The functions D are solutions of the equation [3]:

$$\ddot{D} + 2H(t)\,\dot{D} - \frac{3}{2}H^2(t)\,\Omega_m(t)\,D = 0. \tag{6.46}$$

For a flat universe with no cosmological constant $\left(\Omega_m = \Omega_{m0} = 1,\ a \propto t^{2/3}\right)$, the solutions are:

$$\begin{aligned} D_+(t) &\propto t^{2/3} \propto a(t), \\ D_-(t) &\propto t^{-1} \propto a^{-3/2}(t). \end{aligned}$$

In the general case, this equation needs be integrated numerically. It is more convenient to solve the equation by using the scale factor, a, as the time coordinate. Equation (6.46) takes the form [3]:

$$\frac{d^2D}{da^2} + \left(\frac{1}{H}\frac{dH}{da} + \frac{3}{a}\right)\frac{dD}{da} - \frac{3}{2}\frac{\Omega_{m0}}{a^5}\left(\frac{H}{H_0}\right)^{-2} D = 0, \tag{6.47}$$

where the relation $4\pi G\bar{\rho} = 4\pi G\rho_{m0}a^{-3}$ was used with the assumption that $a_0 = 1$. The decaying mode solution is found to be $D_- = H$. The second solution is then obtained from the method of variation of parameters [3]:

$$D_+(a) = \frac{5}{2}\frac{H(a)}{H_0}\Omega_{m0}\int_0^a \frac{da'}{\left[a'E(a')\right]^3}, \tag{6.48}$$

where $E(a) = \frac{H(a)}{H_0}$ [3]. The normalization constant was chosen such that in a flat matter-dominated universe the solution $D_+ = a$ is recovered.

The above solutions hold when derived in dimensionless coordinates $\tau = \frac{t}{t_0}$. So the density contrast solution is:

$$\delta(\mathbf{x},\tau) = a(\tau)\,\varepsilon_+(\mathbf{x}) + H(\tau)\,\varepsilon_-(\mathbf{x}). \tag{6.49}$$

For the purpose of this thesis, the decaying mode is set to zero. The evolution of the growing mode can then be calculated and compared with existing data. If the decaying mode is removed then the density contrast is:

$$\delta(\mathbf{x},\tau) = \left(\frac{\tau}{\tau_i}\right)^{2/3}\delta_{ini}(\mathbf{x}). \tag{6.50}$$

Using equation (6.41) and remembering that $\delta \ll 1$, due to linearising, the continuity equation becomes:

$$\delta' = -\frac{1}{a}\nabla\mathbf{u}. \tag{6.51}$$

Using equation (6.50) and the Poisson equation, the relationship between the gravitational potential and the velocity is derived as:

$$\mathbf{u}(\mathbf{x},\tau_i) = -\tau_i^{1/3}\left(\frac{4\pi c}{3LH_0}\right)^2\nabla\Phi(\mathbf{x},\tau_i), \tag{6.52}$$

in physical space with dimensionless coordinates. Calculations for the above may be found in Appendix E.2.

6.7 Fourier Space

The evolution of data will be performed using spectral methods which requires that all evolution equations are expressed using the Fourier components. The Fourier decomposition used is [16]:

$$f(\tau,\mathbf{x}) = \frac{1}{(2\pi)^{3/2}}\int \hat{f}(\tau,\mathbf{k})\exp(i\mathbf{x}\cdot\mathbf{k})\,d^3k, \tag{6.53}$$

$$\hat{f}(\tau,\mathbf{k}) = \frac{1}{(2\pi)^{3/2}}\int_V f(\tau,\mathbf{x})\exp(-i\mathbf{x}\cdot\mathbf{k})\,d^3\mathbf{x}, \tag{6.54}$$

where V represents the volume being integrated over. The evolution equations (6.41) and (6.42) become:

$$\hat{\delta}' = -\frac{1}{a}\sum_{l=1}^{3}\left[ik_l\hat{u}_l + ik_l\left(\hat{\delta}\star\hat{u}_l\right)\right], \tag{6.55}$$

$$\hat{u}_j' + \frac{2}{3}\frac{1}{\tau}\hat{u}_j + \frac{1}{a}\sum_{l=1}^{3}\hat{u}_l\star ik_l\hat{u}_j = -\frac{1}{a}\left(\frac{4\pi c}{3LH_0}\right)^2 ik_j\hat{\Phi}, \tag{6.56}$$

where $\sum$ represents a summation of all the terms and $\star$ represents a convolution between the two variables. The initial density contrast is determined from equation (6.40):

$$\hat{\delta}(\mathbf{k}) = -\frac{2}{3}\left(\frac{2\pi c}{LH_0}\right)^2 \tau_i^{2/3} |\mathbf{k}|^2 \hat{\Phi}(\mathbf{k}). \tag{6.57}$$

And the initial velocity is:

$$\hat{u}_j(\mathbf{k}) = -\tau_i^{1/3}\left(\frac{4\pi c}{3LH_0}\right)^2 ik_j \hat{\Phi}(\mathbf{k}). \tag{6.58}$$

Chapter 7

Results

This chapter outlines the results of investigations into spectral methods, and the effects of aliasing on this method. We begin with a discussion of the set up of the initial conditions, and then the evolution equations used are outlined.

The consistency of the code to the continuum solutions can be verified by establishing the convergence rate of the numerical scheme. Section 7.3 discusses the convergence and stability of the evolution. This is done for both the linear and nonlinear evolutions in this section.

The solutions for the density contrast and velocity contain growing and decaying mode terms. The decaying mode is set to zero as described in Section 6.6. Therefore, the growth factor of the density contrast and velocity during linear evolution is known, and can be verified. This verification is performed in Section 7.4.

Non-linear terms are then included in the evolution system. Their effect on the growth is shown in Section 7.5.

Since spectral evolution is susceptible to aliasing, Section 7.6 focusses on identifying and mitigating these effects using filters. Evolving the system when no filter is applied is discussed first. The modes that show non-linear effects are discussed, with emphasis on the time and amount of deviation. The 2/3rd boxcar filter is then introduced - and its stability discussed.

The suggested exponential filter is then applied to the data. We emphasise the merits of this filter, compared to the boxcar, while identifying the introduction of high-frequency aliasing. To determine whether the shape of the exponential filter shows a noticeable improvement in the amount of deviations, while removing the high-frequency aliasing, a shifted-exponential filter is suggested and investigated.

7.1 Initial Data Specification

The spectral code, described in Chapter 5 and 6, was developed to evolve data from an initial redshift until the current epoch. The initial data, for the grav-

itational potential $\hat{\Phi}$, was generated using the power spectrum according to equations (3.12) and (3.13) with n_s and $\mathcal{P}_0$ given according to Table 7.1 (see Section 3.1). A flat spectrum was used for simplicity.

Table 7.1: Initial data parameters based on WMAP measurements [74]

Parameter	Symbol	WMAP data
Curvature perturbations, $k_0 = 0.002\,\mathrm{Mpc}^{-1}$	$\mathcal{P}_0$	2.41 ± 0.10
Scalar spectral index	n_s	0.972 ± 0.013
Age of the universe (Gyr)	t_0	13.74 ± 0.11
Hubble parameter, $H_0 = 100h\,\mathrm{kms}^{-1}\mathrm{Mpc}^{-1}$	H_0	70.0 ± 2.2
Initial Redshift	z	100

The age of the universe, t_0, and the Hubble parameter, H_0, determine the background parameters a, $\bar{\rho}$, and H, in equations (3.29), (3.30), (3.31) - see Section 3.2 for more details. The values of t_0 and H_0 are set according to Table 7.1. The initial redshift is chosen such that the evolution begins in the matter-dominated era - see Section 6.4.

The initial Fourier components of the density contrast, $\hat{\delta}$, and velocity, $\hat{u}_i$, are calculated from $\hat{\Phi}$ using equations (6.57) and (6.58) respectively, see Section 6.7 for details and derivations.

7.2 Evolution

The evolution method implemented was the fourth-order Runge-Kutta time evolution algorithm, as described in Section 5.3. The evolution was conducted in Fourier space, using spectral methods (discussed in Chapter 5). The *linear* evolution equations of the density contrast and velocity are, respectively:

$$\hat{\delta}' = -\tau^{-2/3}\sum_{j=1}^{3} ik_j\hat{u}_j, \tag{7.1}$$

$$\hat{u}_j + \frac{2}{3\tau}\hat{u}_j = -\tau^{-2/3}\left(\frac{4\pi c}{3LH_0}\right)^2 ik_j\Phi. \tag{7.2}$$

The *non-linear* evolution equations are:

$$\hat{\delta}' = -\tau^{-2/3}\sum_{j=1}^{3} ik_j\hat{u}_j - \tau^{-2/3}\sum_{j=1}^{3} ik_j\left(\hat{\delta}\star\hat{u}_j\right), \tag{7.3}$$

$$\hat{u}_j' = -\frac{2}{3\tau}\hat{u}_j - \tau^{-2/3}\sum_{g=1}^{3}\hat{u}_g\star(ik_g\hat{u}_j) - \tau^{-2/3}\left(\frac{4\pi c}{3LH_0}\right)^2 ik_j\Phi, \tag{7.4}$$

where $j = x,\ y,\ z$ for both the linear and non-linear equations. See Section 6.7 for derivations. We will carry out evolutions of both the linear and nonlinear systems, clearly indicating which case is being considered in each section.

The behaviour of the mode, $\mathbf{k}$, will be discussed, which represents a particular physical scale. Variables with a ' $\sim$ ' represent physical variables, all other variables refer to quantities evaluated on the discrete numerical grid.

7.3 Code Convergence

To measure how stable and consistent a numerical simulation is, the convergence of the simulation must be determined. Due to the discretisation of signals when represented on a grid - see Chapter 5 - the evolution of the signal is not identical to the expected signal. As the number of wavenumbers in the numerical model increases, the signal better approximates the continuum solution, therefore the difference should decrease as the spacing decreases. The grid spacing h is determined by the highest wavenumber included on the grid.

If g_j is the calculated signal, then $(g_e)_j$ is the expected signal at the points, j. The convergence can be obtained by [103]:

$$\left\| g_j - (g_e)_j \right\| \simeq C h^p, \tag{7.5}$$

where C is a constant, h is the space or time resolution, and p is the order of convergence. The convergence is calculated for different resolutions to determine the order.

The relationship between the convergence order and total difference gives the expression for the L_1-norm, defined as:

$$\begin{aligned} L_1\text{–norm} &= \left(\frac{2\pi}{N}\right)^3 \sum_j \left\| g_j - (g_e)_j \right\| \\ &= (d\tau)^p \,, \end{aligned} \tag{7.6}$$

where p will determine the order of convergence.

The time evolution method used is the fourth-order Runge-Kutta algorithm, see Section 5.3. Since the spatial variables are initially continuous and differentiable at all orders, the expected spatial convergence is exponential. As the dust collapses, non-linear terms grow, the continuity assumptions may break down so that the spatial order may degrade. Initially, we expect the convergence rate to be determined by the fourth-order time integrator.

The evolution equations used contain both linear and non-linear terms. The order of convergence of the linear equations is expected to be fourth-order. The space resolution can remain constant, while the time resolution is decreased to obtain the order of convergence. However, in order to obtain the non-linear convergence, the time and space resolution need to be reduced by the same

ratio. This is due to the coupling of the space and time components in non-linear terms.

The remainder of this section is dedicated to calculating the convergence of the linear and non-linear evolution equations.

Unless otherwise stated, the linear evolutions use a grid-size of $N = 54$ wavenumbers in each dimension. The largest physical scale value of 4166 Mpc ($|\tilde{\mathbf{x}}|$) - which corresponds to $|\tilde{\mathbf{x}}| = L$.

In the non-linear section the grid size and time-step size must be decreased by the same ratio. The smallest grid size is $N = 12$, and with each doubling of the number of wavenumbers the time-step size, $\triangle\tau$, is halved.

7.3.1 Linear Convergence

The numerical scheme was first tested by performing evolutions of the linear system, equations (7.1) and (7.2). Since the evolution only contains linear terms, the expected results for the dynamical variables as a function of τ are:

$$\hat{\delta}_\epsilon(\mathbf{k},\tau) = \left(\frac{\tau}{\tau_i}\right)^{2/3} \hat{\delta}_{ini}(\mathbf{k}), \tag{7.7}$$

$$\hat{u}_{j_\epsilon}(\mathbf{k},\tau) = \left(\frac{\tau}{\tau_i}\right)^{1/3} (\hat{u}_j)_{ini}(\mathbf{k}). \tag{7.8}$$

One expects to see convergence of the same order regardless of the physical size of the grid, since the growth does not depend on it.

The L_1-norm is calculated by decreasing the time resolution, and keeping the spatial resolution constant, equation (7.6). The spatial resolution can remain constant since it has no effect on the linear system's convergence, because all modes evolve independently. This allows us to establish convergence by changing the time-step size while keeping the spatial resolution fixed. Figure 7.1 shows the L_1-norm for $\hat{\delta}$ and $\hat{\mathbf{v}}$. The slope, and therefore the order of convergence, is 3.933 for $\hat{\delta}$ and 4.084 for $\hat{\mathbf{v}}$ - these values are consistent with the order of the Runge-Kutta algorithm. Changing L does not affect the gradients significantly.

Another graph of interest is the L_1-norm for different τ values and time-step sizes - as shown in Figure 7.2 (a) and (c). Since the evolution equations converge, multiplying by the ratio of $\left(\frac{d\tau_{min}}{d\tau_i}\right)^4$ should result in all the curves overlapping (where $d\tau_i$ is the time-step size of the current curve, and $d\tau_{min}$ is the smallest time-step size). This is shown in Figure 7.2 (b) and (d). The curves for $d\tau$ larger than 0.0091 do not overlap, which suggests that there is a slight curve in Figure 7.1 which cannot be easily observed. As long as the time-step size is smaller than 0.0091 convergence is verified at all times.

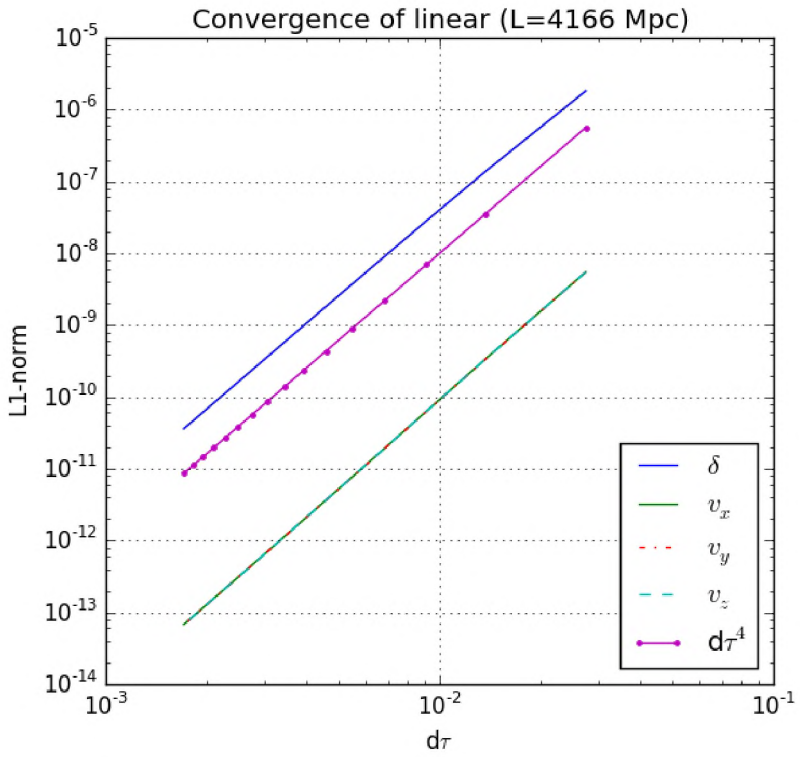

Figure 7.1: The L_1-norm for $\hat{\delta}$ and $\hat{\mathbf{v}}$ at $\tau = 0.2467$ on a grid with $L = 4166$Mpc. The lines are parallel to $d\tau^4$, indicating fourth-order convergence.

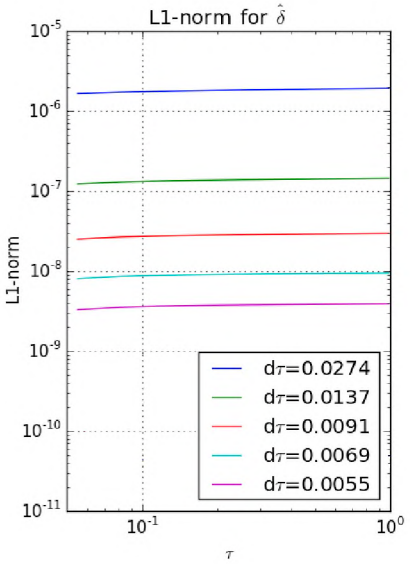

(a) L_1-norm for $\hat{\delta}$. The lines show an increase in the norm as time increases. Notice the spacing between lines gets smaller as the time-step is halved.

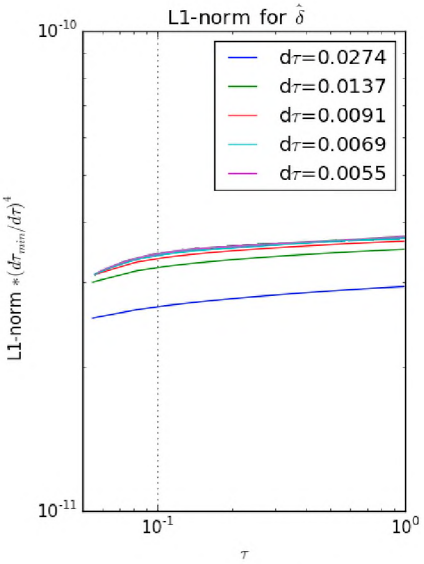

(b) L_1-norm for $\hat{\delta}$ scaled by $\left(\frac{d\tau_{min}}{d\tau}\right)^4$. The lines begin to overlap indicating convergence.

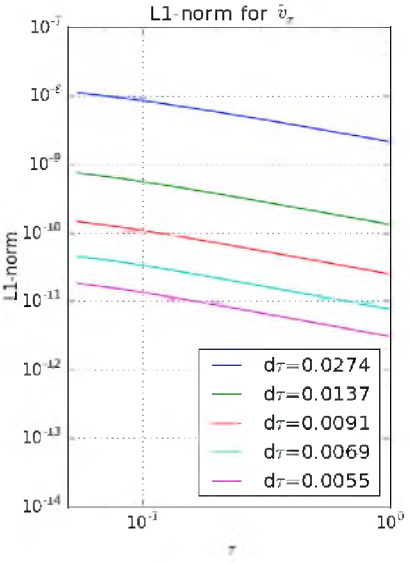

(c) L_1-norm for $\hat{v}_x$. The lines show an decrease in the norm as time increases. Notice the spacing between lines gets smaller as the time-step is halved.

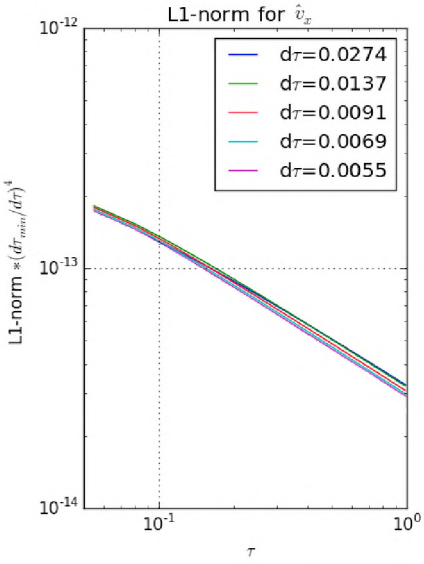

(d) L_1-norm for $\hat{v}_x$ scaled by $\left(\frac{d\tau_{min}}{d\tau}\right)^4$. The lines begin to overlap indicating convergence.

Figure 7.2: The L_1-norm for $\hat{\delta}$ and $\hat{v}_x$ vs τ.

7.3.2 Non-linear Convergence

The convergence rate was then verified for the set of nonlinear equations (7.3) and (7.4). The non-linear contributions are small, when working at large scales, for all τ. Initially, where $|\tilde{\mathbf{x}}| \lesssim 10\text{Mpc}$, the scales contain small non-linear terms. Then at later τ these terms become larger than the linear ones.

Notice that, as mentioned in the beginning of Section 7.3, it is not sufficient to decrease the time-step size alone in order to obtain the non-linear system's convergence. Modes become coupled in this scenario which results in the spatial discretisation affecting the accuracy and convergence rate of the numerical solution. This is verified in Figure 7.3(a), where the L_1-norm decreases for the first time-step sizes, but remains constant for the remaining time-step sizes. Therefore, the results fail to converge due to the fixed spatial resolution.

To obtain the convergence of the non-linear evolution, the time resolution and spatial resolution are halved together ($d\tau$ and h respectively). Since $h = \frac{2\pi}{N}$ this means N must be doubled. This is equivalent to including more wavenumbers ($|\mathbf{k}|$) on the grid in Fourier space. These new $|\mathbf{k}|$ values have delta and velocity set to zero initially. When calculating the L_1-norm the only $|\mathbf{k}|$ points included in the sum are the ones common to all the grids.

In Figure 7.3(b), the smallest N value is 12 and $d\tau = \frac{2\pi}{10N}\tau_i$ - where τ_i is the initial time. The factor of 10 is to ensure that the grid has linear convergence. The data converges with order 3.004, even when L is small enough to introduce significant non-linear effects.

The L_1-norm versus τ is plotted in Figure 7.4. Similar to Figure 7.2, a factor of $\left(\frac{d\tau_{max}}{d\tau_i}\right)^3$ is included which makes all the graphs overlap (where $d\tau_{max}$ is the largest time-step size).

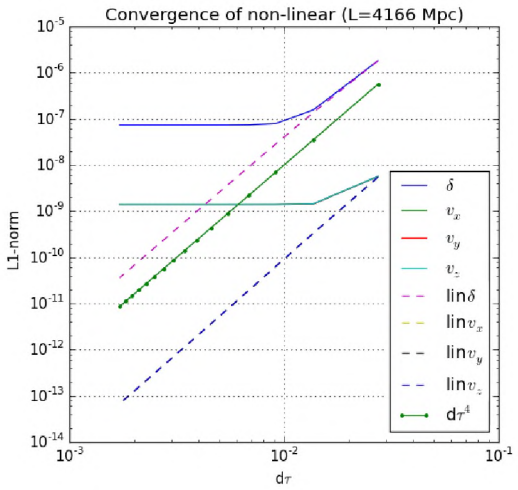

(a) The L_1-norm for $\tilde{\delta}$ and $\tilde{\mathbf{v}}$ at $\tau = 0.2467$ on a grid with $L = 4166$Mpc. Note the lack of convergence for non-linear evolution.

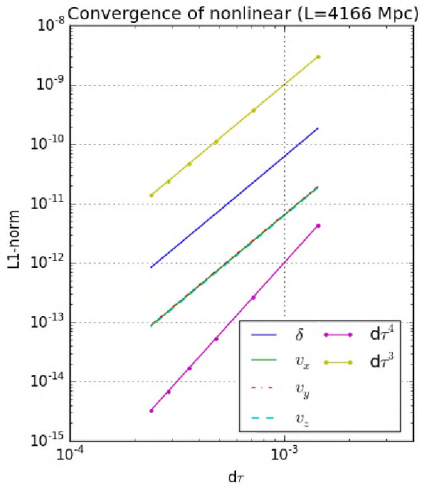

(b) The L_1-norm for $\tilde{\delta}$ and $\tilde{v}_x$ at $\tau = 0.2467$ on a grid with $L = 4166$Mpc. Note the third-order convergence for both variables.

Figure 7.3: Convergence for the nonlinear system. In (a) the spatial grid is kept fixed as the time-step is halved. The results fail to converge. In (b) the spatial resolution is halved along with the time-step which results in third-order convergence.

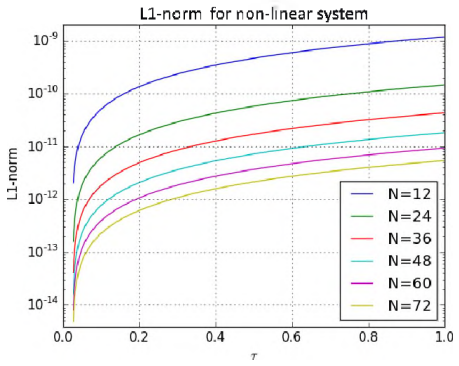

(a) L_1-norm for $\hat{\delta}$. The lines show an increase in the norm as time increases. Notice the spacing between lines gets smaller as the time-step and spatial resolution are halved.

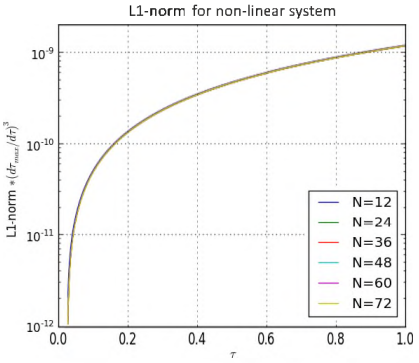

(b) L_1-norm for $\hat{\delta}$, multiplied by $\left(\frac{d\tau_{max}}{d\tau}\right)^3$. The lines overlap implying convergence.

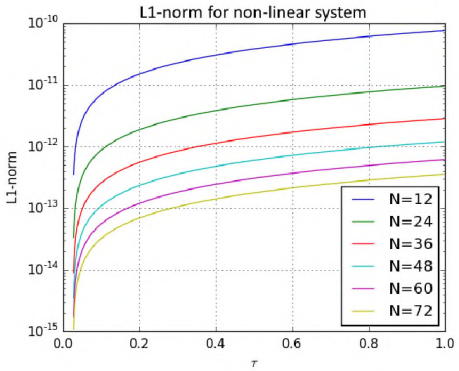

(c) L_1-norm for $\hat{v}_x$. The lines show an increase in the norm as time increases. Notice the spacing between lines gets smaller as the time-step and spatial resolution are halved.

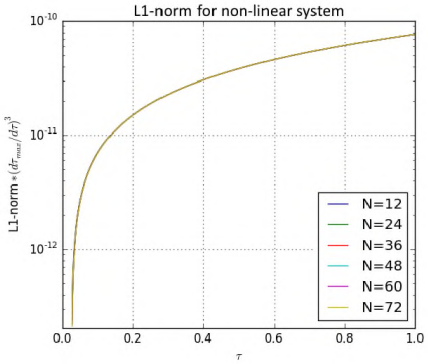

(d) L_1-norm for $\hat{v}_x$, multiplied by $\left(\frac{d\tau_{max}}{d\tau}\right)^3$. The lines overlap implying convergence.

Figure 7.4: The L_1-norm for $\hat{\delta}$ and $\hat{v}_x$ vs τ.

7.4 Simulation Accuracy

7.4.1 Expected Results

As discussed in Section 6.6, the solution of the propagation equation during matter domination takes the form of equation (6.45).

The decaying mode is set to zero initially. Therefore, the expected growth should correspond to the growing mode, growth similar to $D_+ = a$. When for example $\frac{\delta}{\delta_i}$ is plotted, henceforth referred to as the growth of the variable, it is expected to reproduce the solid line shown in Figure 7.5. This is because $\Omega_{m0} = 1$ was assumed in Section 6.6.

Similarly, the solution for the velocity takes the form of equation (6.45) with a growing mode of $D_+ = t^{1/3} = a^{1/2}$.

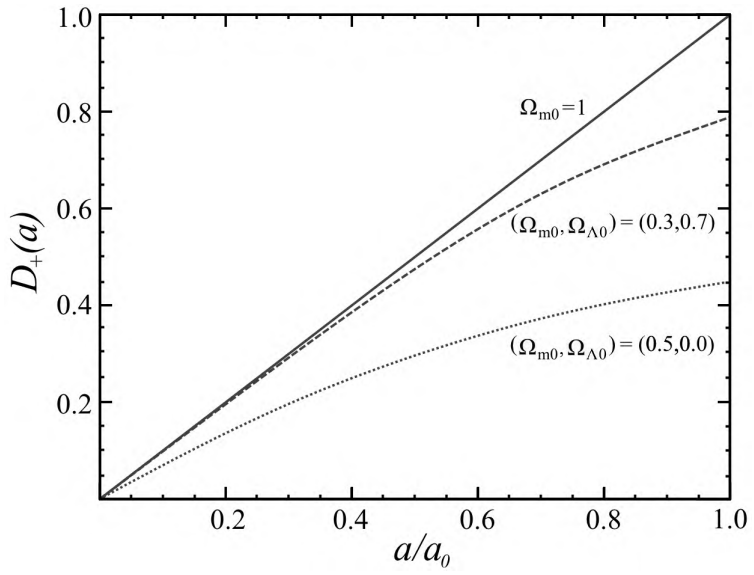

Figure 7.5: Evolution of the growing mode of the density contrast, $D_+(a)$, as a function of the scale factor, a. Adapted from [3]

7.4.2 Growing Rate of the dynamical variables

To investigate whether the data evolves with the expected growth, the initial data is generated and evolved for comparison against the expected. The grid dimensions are set according to Table 7.2.

Table 7.2: Initial conditions

Variable	Value
N	54
z	100
L	4166 Mpc

The total number of grid points is N^3, z is the initial redshift, and L is the physical size of the box at redshift $z = 0$.

The physical modes, $\left|\tilde{\mathbf{k}}\right|$, presented on the grid are contained in:

$$\left|\tilde{\mathbf{k}}\right| \quad \in \quad [1.5, \ldots, 27.2] \times 10^{-3}\ \mathrm{Mpc}^{-1}, \tag{7.9}$$

where the smallest physical scale observable is $|\tilde{\mathbf{x}}| = 231.4$ Mpc.

The numerical scheme was tested using the linear evolution system, equations (7.1) and (7.2). Figure 7.6(a) illustrates the ratio

$$\log\left(\frac{\hat{\delta}}{\hat{\delta}_i}\right), \tag{7.10}$$

for every mode, where $\hat{\delta}_i$ is the initial density contrast, and $\hat{\delta}$ is the density contrast at the current time τ. This ratio is referred to as the *growth* of the variable.

The expected density contrast, $\hat{\delta}_e$, is given by equation (7.7) as stated in section 7.3. The *difference* between the numerical and expected variable is given by:

$$\epsilon_\tau \quad \equiv \quad \left|\frac{\left(\hat{\delta} - \hat{\delta}_e\right)}{\hat{\delta}_e} \times 100\right|. \tag{7.11}$$

This difference is a measure of the error in the numerical solution from the analytical result, which may contain non-linear corrections and aliasing effects. The difference in the velocity $\hat{u}_j$ is expressed in the same way. The difference for $\hat{\delta}$ is shown in Figure 7.6(b). The slope of the growths for $\hat{\delta}$ and $\hat{v}_{x_i}$ are shown in Table 7.3.

All lines in Figure 7.6 overlap which indicates that over time the growth and difference is identical for every mode. The growth is plotted versus time τ,

therefore the slope of the growth of $\hat{\delta}$ and $\hat{v}_{x_i}$ should correspond to $\frac{2}{3}$ and $\frac{1}{3}$, respectively. The slope is extremely close to the expected gradient, shown in Table 7.3.

Table 7.3: Results for growing mode

Quantity	Measured slope	Expected slope	Difference
$\hat{\delta}$	0.666666664588	$\frac{2}{3}$	$\epsilon_\tau \leq 3.5 \times 10^{-6}$
$\hat{v}_i$	0.333333333237	$\frac{1}{3}$	$\epsilon_\tau \leq 3.0 \times 10^{-7}$

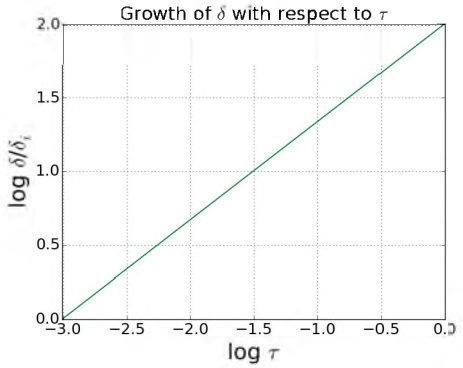

(a) The growth $\log\left(\hat{\delta}/\hat{\delta}_i\right)$ versus $\log(\tau)$, for all modes $|\mathbf{k}|$

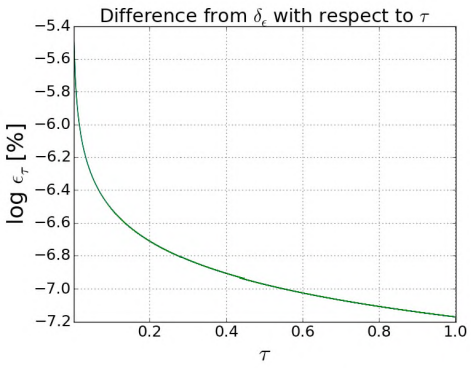

(b) The difference ϵ_τ for the density contrast, for all modes $|\mathbf{k}|$

Figure 7.6: The linear evolution of the data from $z = 100$ to $z = 0$. The final physical box size is $L - 4166\,\mathrm{Mpc}$. Observable modes are contained in equation (7.9).

7.5 Emergence of Non-linearity

As discussed in Chapter 2, cosmological perturbation theory explains that there were small perturbations in the CMB that gave rise to the current structure of the universe. From matter-photon decoupling, to the present day, the evolution of the fields has been linear on large scales - as shown by the homogeneous and isotropic nature of the universe on large scales.

However, the non-linear terms have grown as well, and are visible on smaller scales. We expect to see deviations from linear behaviour on scales $\sim 8h^{-1}\,\mathrm{Mpc}$ [74] at $z = 0$. The quasi-linear regime extends to about $30h^{-1}\,\mathrm{Mpc}$ [76] at $z = 0$ but is significantly smaller at higher redshifts [76].

On scales $\left|\tilde{\mathbf{k}}\right|^{-1} \gtrsim 10h^{-1}\,\mathrm{Mpc}$ at $z = 0$, bound objects have yet to form, and linear theory is still valid [6]. On small scales, the regime of linear theory ends at an epoch $z_{\mathrm{nl}}(\mathbf{k})$, after which non-linearity sets in [6].

7.5.1 Effect on Growing Mode

To investigate the effect that the non-linear terms have on the growth of the fields $\hat{\delta}$ and $\hat{\mathbf{v}}$, the initial data is generated using the variables from Table 7.2 - as before. Where the smallest scale observable is $|\tilde{\mathbf{x}}| = 231.4\mathrm{Mpc}$. The evolution is then conducted using the evolution equations with non-linear terms included, equations (7.3) and (7.4).

With the inclusion of non-linear terms the evolution of modes changes. In the linear system, each mode $\mathbf{k} = (k_x, k_y, k_z)$ with magnitude $|\mathbf{k}|$ evolved with the same growth and ϵ_τ. When non-linear terms are included, not only do modes with different $|\mathbf{k}|$ values evolve differently, but modes that share the same $|\mathbf{k}|$ do not evolve in the same way. This is not observable in Figure 7.7(a), however it is observable in the difference over time in Figure 7.7(b).

Figure 7.7(a) illustrates that the non-linear effects, while present, create no observable corrections to the growth due to their size at these scales. This is the expected behaviour for these scales.

The ϵ_τ, calculated using equation (7.11), now contains the deviation caused by the non-linear terms. The change in behaviour of ϵ_τ over time - shown in Figure 7.7(b) - indicates that the observed ϵ_τ is not due to the evolution method used. There are two possible sources of these deviations: non-linear terms, and aliasing effects - to be considered in Section 7.6. If ϵ_τ was larger on these scales, the graphs would indicate that aliasing is definitely occurring. This is because differences are not expected to be observable on these scales.

Generally, ϵ_τ shows the same behaviour for all modes and grows linearly after $\tau = 0.2$.

In Figure 7.7(b), a few modes' difference initially decrease, and at some later time increase again resulting in the dips in graph. After the decrease the shape becomes consistent with the other modes. These dips occur in modes which initially deviate to the 'right' of the expected value. The evolution causes the mode to tend closer to the expected value, i.e. the spike down. At some time the mode passes to the 'left' of the expected value and the difference continues to grow in that direction.

Since the shape of ϵ_τ generally increases as time progresses, more information can be obtained from considering the difference from linear growth at particular epochs, for example $z = 0$. Figure 7.8 illustrates what ϵ_τ looks like on each axis at times $\tau \in [0.25, 0.50, 1.00]$. All modes show an increase in ϵ_τ as time increases, and ϵ_τ generally increases as k_i increases. The differences remain small for these scales, as expected.

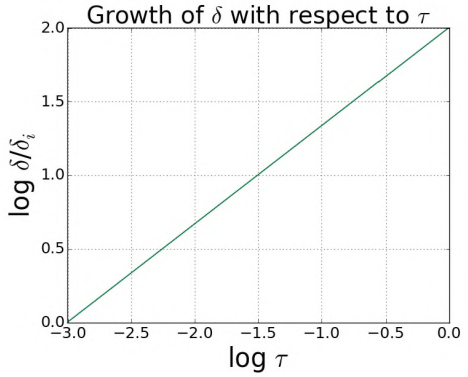

(a) The growth of $\log\left(\hat{\delta}/\hat{\delta}_i\right)$ versus $\log(\tau)$ for all modes $|\mathbf{k}|$

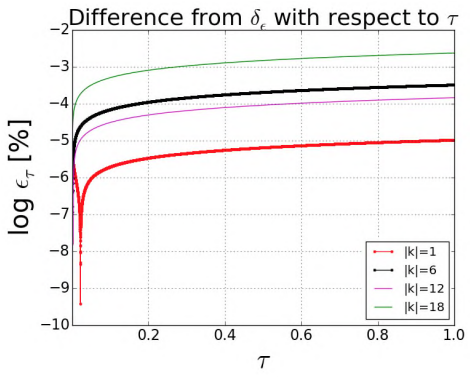

(b) The non-linear difference ϵ_τ for the density contrast over time. Each line represents the difference of a mode $\mathbf{k} = (k_x, k_y, k_z)$, where the magnitude $|\mathbf{k}|$ is: 1 (red), 6 (black), 12 (pink), and 18 (green). Notice how each mode, with the same magnitude $|\mathbf{k}|$, evolves differently.

Figure 7.7: The non-linear evolution of the data from $z = 100$ to $z = 0$. Modes are contained in equation (7.9) and $L = 4166\,\text{Mpc}$.

7.5.2 Nonlinear Scale

Minimal ($\ll 1\%$) non-linear differences were observed on a box of size 4166 Mpc, see Section 7.5.1 for detailed results. The differences are not expected to become *percent differences* on a box of that size - a percent difference is defined as having a value greater than or equal to 1 percent of the expected linear evolution value. The scales where non-linear deviations are expected to become observable are where $|\tilde{\mathbf{x}}| \leq 8h^{-1}$ Mpc.

To observe these non-linear differences, the physical size of the numerical grid needs to be decreased in order to resolve smaller scales at the same computational cost. With this in mind, the initial data for this section is generated from the variable values in Table 7.4.

Table 7.4: Initial conditions

Variable	Value
N	54
z	100
L	100 Mpc

Figure 7.9 illustrates the change over time of the growth and ϵ_τ from linear behaviour at the present epoch, for this initial data. The differences in Figure 7.9(a) indicate when non-linear growth begins for the mode - these deviations

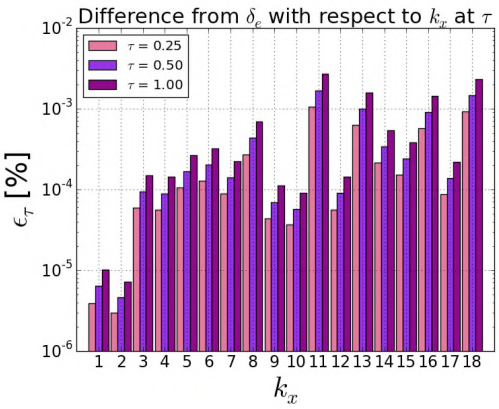

(a) The non-linear differences ϵ_τ for the $\tilde{\delta}$, for modes along the x-axis.

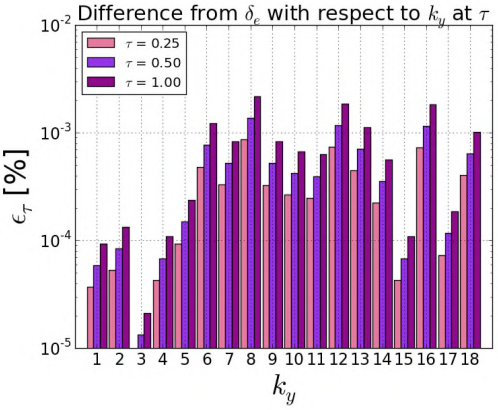

(b) The non-linear differences ϵ_τ for the $\tilde{\delta}$, for modes along the y-axis.

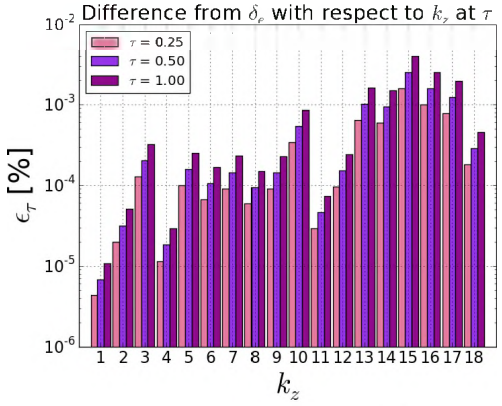

(c) The non-linear differences ϵ_τ for the $\tilde{\delta}$, for modes along the z-axis.

Figure 7.8: The non-linear differences ϵ_τ for the $\tilde{\delta}$ along the x, y and z axis.

are relatively small, and grow as time increases. Small differences are expected at the current epoch, and this is consistent with what is shown in the graphs.

The ϵ_τ over time for modes $|\mathbf{k}| = [1, 6, 12, 18]$ are illustrated in Figure 7.9(b). All the modes where $|\mathbf{k}| = 1$ and $|\mathbf{k}| = 6$ have ϵ_τ less than 1%. However, many modes like $|\mathbf{k}| = 12$ and $|\mathbf{k}| = 18$ have ϵ_τ in the range $1 - 20\%$. Non-linear deviations are expected to become observable on the modes $|\mathbf{k}| \geq 9$, since those are the modes on the grid that correspond to $|\tilde{\mathbf{x}}| \leq 8h^{-1}\,\text{Mpc}$. This explains why ϵ_τ are too small to be observed on $|\mathbf{k}| = [1, 6]$ and are visible on $|\mathbf{k}| = [12, 18]$.

Figure 7.10 illustrates the differences for all modes along the axis's at times $\tau \in [0.25, 0.50, 1.00]$. Many of these modes have minimal differences, however the difference for the mode $\mathbf{k} = (0, 11, 0)$ is of order 10% at $\tau = 1$. Generally, the difference increases with increasing $|\mathbf{k}|$.

The largest scale that experiences multiple differences of order 1% is $|\tilde{\mathbf{x}}| = 14.29\,\text{Mpc}$ (i.e. $|\mathbf{k}| = 7$), however there is one $|\mathbf{k}| = 3$ point that shows such a difference. This indicates that the differences are becoming large enough to observe on scales larger than expected.

The modes where $|\mathbf{k}| \geq 9$ (scales $|\tilde{\mathbf{x}}| \leq 11.11\,\text{Mpc}$) experience many differences of between $1 - 20\%$ and begin to show percent differences at early times in the evolution, i.e. $z \approx 100$. One expects to see differences on these scales, however **percent differences** should only become visible at later times. This indicates that the differences are being influenced by aliasing effects - Section 5.4 discusses this in more detail.

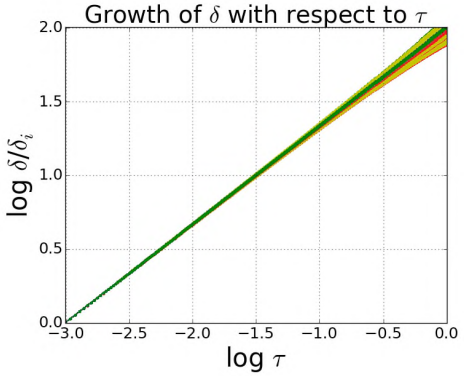

(a) The growth for all modes $|\mathbf{k}|$.

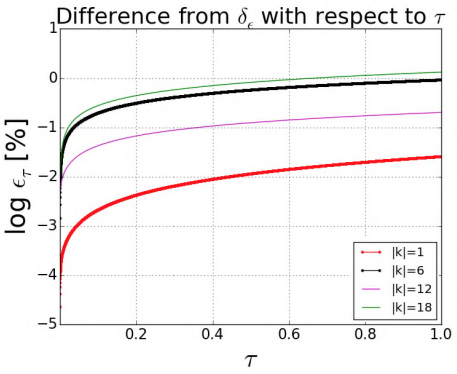

(b) The non-linear difference ϵ_τ for the density contrast over time. Each line represents the difference of a mode $\mathbf{k} = (k_x, k_y, k_z)$, where the magnitude $|\mathbf{k}|$ is: 1 (red), 6 (black), 12 (pink), and 18 (green). Notice how each mode, with the same magnitude $|\mathbf{k}|$, evolves differently.

Figure 7.9: The non-linear evolution of the data from $z = 100$ to $z = 0$. The box size is $L = 100\,\text{Mpc}$ and the smallest scale observable is $|\tilde{\mathbf{x}}| = 5.55\,\text{Mpc}$.

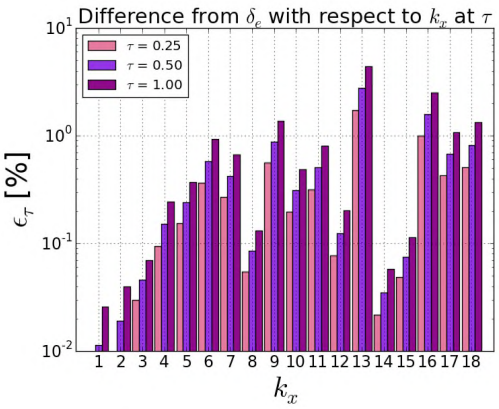

(a) The non-linear differences ϵ_τ for the $\hat{\delta}$, for modes along the x-axis.

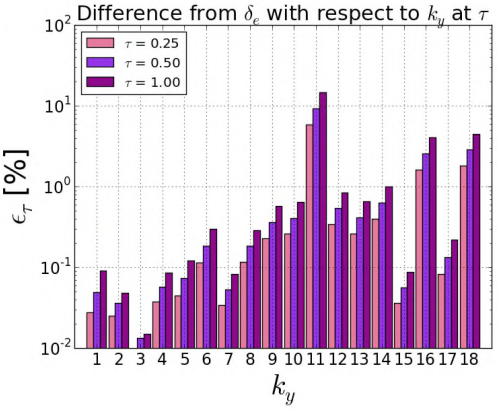

(b) The non-linear differences ϵ_τ for the $\hat{\delta}$, for modes along the y-axis.

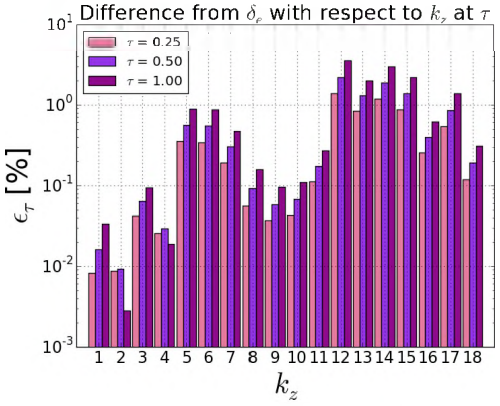

(c) The non-linear differences ϵ_τ for the $\hat{\delta}$, for modes along the z-axis.

Figure 7.10: The non-linear differences ϵ_τ for the $\hat{\delta}$ along the x, y and z axis.

7.6 Aliasing Effects

The previous sections have verified that the code is stable - see Section 7.3 - and is evolving the data correctly - see Section 7.4. This section will discuss the presence of aliasing effects on the grid.

Aliasing is not present in the linear evolution due to the independent nature of the evolution of modes. To observe aliasing effects, all tests are performed with the inclusion of non-linear terms. This means conducting the evolution using equations (7.3) and (7.4).

Four tests have been performed: no filter, 2/3rd boxcar filter, exponential filter, and shifted filters. The first serves to illustrate why filters are necessary and the remaining tests are performed to compare the merits of each filter in question.

7.6.1 Evolution of Unfiltered Data

To verify the necessity for applying a filter in the non-linear evolution, we considered the case where no filter is applied to the data - where there is no initial filtering, and no filtering after each time-step. The initial data is generated using the values from Table 7.1 and 7.2. Since no filter is applied, the smallest scales present are: 154 Mpc and 3 Mpc for the 4166 Mpc and 100 Mpc grids, respectively.

Growth and ϵ_τ graphs were generated for each grid size: Figure 7.11(a) and (b) for the 4166 Mpc grid, and Figure 7.11(c) and (d) for the 100 Mpc grid.

On the 4166 Mpc grid, none of the scales should experience observable non-linear differences. No non-linear contributions can be seen in Figure 7.11(a), and the differences remain less than 0.1% for all times, as expected.

The non-linear differences should be significant on the $L = 100$ Mpc grid, and this was confirmed by observation of the time-evolution data. The largest scale where percent differences occur is $|\tilde{\mathbf{x}}| = 50$ Mpc, however these differences occur late in the time evolution. Comparatively, percent differences at early times ($z \approx 100$) are first observed on the scale $|\tilde{\mathbf{x}}| = 33.33$ Mpc.

Since the differences should only become observable on scales of the order $|\tilde{\mathbf{x}}| \leq 11.43$ Mpc, this indicates that errors **are** being introduced. These errors are due to the occurrence of high-frequency aliasing - see Sections 5.4.3 and 5.4.4.

Since the convolution present in the non-linear terms creates a signal that contains twice the number of modes as the terms being convolved - see Section 5.4 for further details - the high-frequency aliasing is expected to influence all modes present on the grid. This can be seen when comparing Figure 7.7(b) to Figure 7.11(b), where modes show larger differences in the latter. Similarly, the differences present in Figure 7.11(d) are larger than those present in Figure 7.9(b).

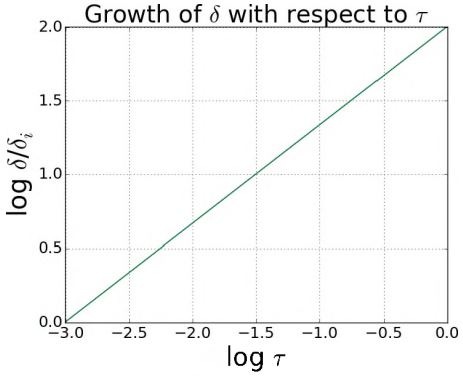

(a) The growth of $\hat{\delta}$ on grid $L = 4166$ Mpc

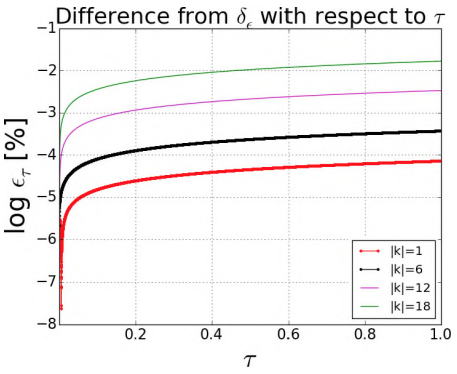

(b) The non-linear differences ϵ_τ for the density contrast over time, on grid $L = 4166$ Mpc. Each line represents the difference of a mode $\mathbf{k} = (k_x, k_y, k_z)$, where the magnitude $|\mathbf{k}|$ is: 1 (red), 6 (black), 12 (pink), and 18 (green).

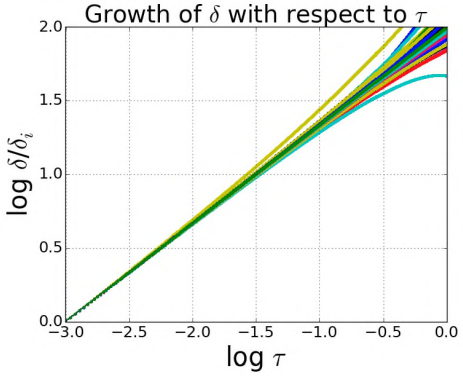

(c) The growth of $\hat{\delta}$ on grid $L = 100$ Mpc

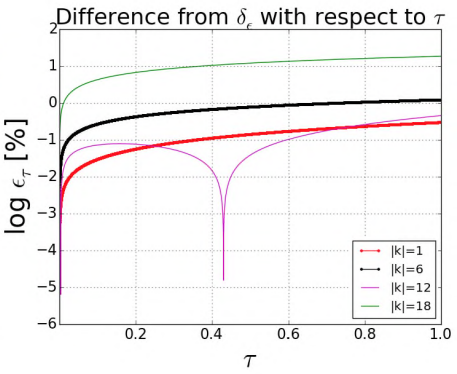

(d) The non-linear differences ϵ_τ for the density contrast over time, on grid $L = 100$ Mpc. Each line represents the difference of a mode $\mathbf{k} = (k_x, k_y, k_z)$, where the magnitude $|\mathbf{k}|$ is: 1 (red), 6 (black), 12 (pink), and 18 (green).

Figure 7.11: No filter has been applied to the data during time evolution. Only scales $0 \leq |\mathbf{k}| \leq \frac{N}{3}$ are shown.

7.6.2 Boxcar Filter with 2/3rd Cutoff

To remove the effects of high-frequency aliasing, a filter is applied to the data. This filter is applied before the evolution starts, and at the end of every time-step. The boxcar filter used in this Subsection has a cut-off frequency of $|\mathbf{k}| = \frac{N}{3} = 18$.

Due to the chosen cut-off frequency, the smallest observable scales are: 231.4 Mpc and 5.5 Mpc on grids of size 4166 Mpc and 100 Mpc, respectively.

This filter was applied when generating the results for Section 7.5.

The scale where percent differences begin to be observable has gone from 50 Mpc, in the no filter case, to 33.33 Mpc, which is closer to expected. Percent differences at early times become visible on the scale 10 Mpc. This is an improvement from the no filter case, however the differences still occur at early times, which is a concern. Fortunately, the scales where these errors are observed is closer to the expected scale. Graphs for L of 4166 Mpc and 100 Mpc are shown in Figure 7.7 and 7.9, respectively.

This filter may create Gibbs ripples, as discussed in Section 5.4.5. In order to observe the ripples that may be created, consider the *norm*, $\|\mathrm{X}\|_\tau$, at a particular time - Figure 7.12. The norm will be defined as:

$$\begin{aligned} \left\|\hat{\delta}\right\|_\tau &\equiv \hat{\delta}\left(\mathbf{k},\tau\right) \div \left(\left(\frac{\tau}{\tau_i}\right)^{2/3} \hat{\delta}_{ini}\left(\mathbf{k}\right)\right) \\ &= \frac{\hat{\delta}}{\hat{\delta}_e}. \end{aligned} \tag{7.12}$$

This ratio is equivalent to 1 for linear evolution since the difference ϵ_τ was of order $10^{-7}\%$.

The $\|\mathrm{X}\|_\tau$ is plotted for all points $\mathbf{k} = (k_x, k_y, k_z)$, where the magnitude of the mode $|\mathbf{k}|$ is an integer, at four τ values during the evolution i.e. $\tau \in [0.25,\ 0.5,\ 0.75,\ 1]$ (Figure 7.12). The solid red line represents the average value for the mode $|\mathbf{k}|$, the dashed black lines indicate one standard deviation from the average, and the grey shaded area covers all points within one standard deviation of the average. Near the start of the evolution, i.e. $\tau = 0.25$, the points of a particular magnitude are collected around one. The points are more spread out for the larger $|\mathbf{k}|$ values which indicates that the non-linear contributions are already visible, however the average line shows only slight ripples. As the evolution progresses the points of the large modes become more spread out, and the oscillations in the average line grow larger.

Notice how the height of the oscillations in the average line increases as the mode gets closer to the discontinuity, which is indicative of Gibbs ripples. To reduce the oscillations a smoother filter is considered in the next subsection.

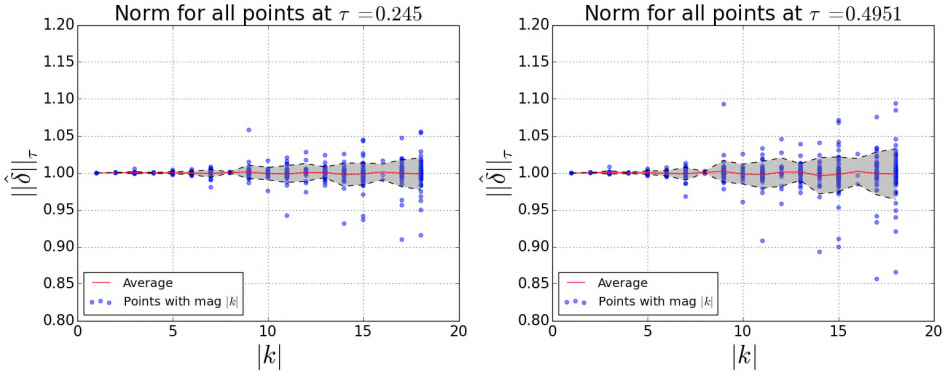

(a) Norm at $\tau \approx 0.25$

(b) Norm at $\tau \approx 0.50$

(c) Norm at $\tau \approx 0.75$

(d) Norm at $\tau \approx 1.00$

Figure 7.12: The norm $\left\|\hat{\delta}\right\|_\tau$ at particular times for a grid $L = 100$ Mpc are shown. Only integer modes between $0 \leq |\mathbf{k}| \leq \frac{N}{3}$ are shown. The average (solid red line) and standard deviation (dashed black lines) for each mode is shown. The shaded area contains the points enveloped within one standard deviation of the average. Notice the oscillations present in the average line and the general increase in the spread of the points as time progresses.

7.6.3 The Exponential Filter

By including the boxcar filter, in the last section, the evolution became more stable, and smaller differences from the linear behaviour were observed. However, including this filter introduced Gibbs ripples - as seen by the shape of the average, over time, in Figure 7.12.

To potentially reduce the Gibbs ripples, the smooth exponential filter (suggested by Hou and Li [1]) is considered. The benefits of this filter are that: it has a smooth cutoff which should reduce ripple effects, and it allows 20% more modes than the 2/3rd boxcar filter [1]. For further details see Subsection 5.4.6.

The exponential filter takes the form of equation (5.29) from Section 5.4.6. The initial data is generated for the two box sizes, and evolved with and without non-linear terms. The exponential filter is applied to the initial data, and again after every time-step. The expected solution is modified since the filter is smooth, and not zero or unity at every point;

$$\delta(\mathbf{k},\tau) = \left(\frac{\tau}{\tau_i}\right)^{2/3} [\delta_{ini}(\mathbf{k}) \times F(\mathbf{k})] \times [F(\mathbf{k})]^{\#\triangle\tau}, \tag{7.13}$$

where $\#\triangle\tau$ is the number of times the time evolution has been performed, and $\delta_{ini}(\mathbf{k})$ is the density contrast before any filter has been applied.

Since the filter is not 1 or 0 at every mode, and instead curved, the ϵ_τ over time graphs show a different behaviour to the linear and non-linear systems presented in Section 7.4 and 7.5. The linear and non-linear evolution ϵ_τ graphs are shown for the 4166 Mpc grid in Figure 7.13.

For the linear system: although points of a particular mode (example $|\mathbf{k}| = 2$) all evolve the same way, modes with different $|\mathbf{k}|$ values evolve differently - see Figure 7.13(a). Points where $|\mathbf{k}| \geq 14$ experience an increase in ϵ_τ over time, $|\mathbf{k}| \leq 11$ experience a decrease in ϵ_τ over time, and the remaining modes experience a mixture.

The same behaviour is present in the non-linear system in Figure 7.13(b) for modes where $|\mathbf{k}| \geq 16$. This indicates that either the expected solution is not correct, or the filter changed the growth of modes where the filter is not equal to 1 up to an order of 10^{-12}. Since the linear system cannot contain aliasing effects or non-linear effects, a comparison between the linear and non-linear systems can be performed in order to compare the accuracy of the boxcar and exponential filters. Therefore, only the effects of aliasing and non-linear terms will be present.

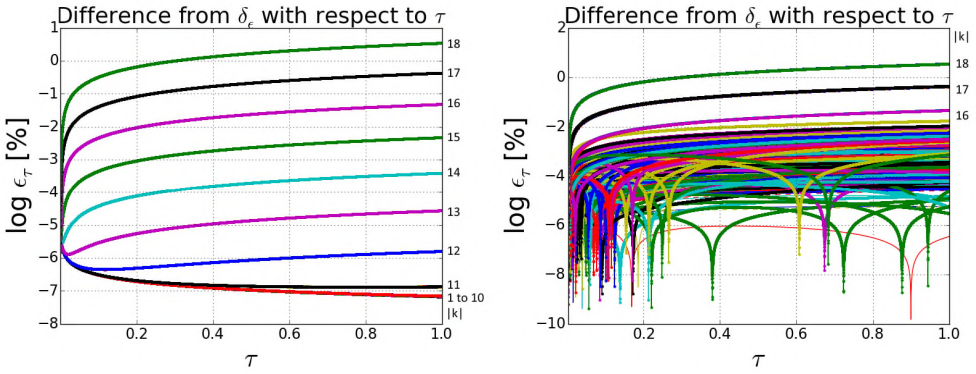

(a) Linear evolution

(b) Non-linear evolution

Figure 7.13: Differences ϵ_τ, calculated using equation (7.11), for the evolution of the exponential filter. Linear evolution (left), and non-linear evolution (right). The box size is $L = 4166\,\text{Mpc}$. Only scales $0 \leq |\mathbf{k}| \leq \frac{N}{3}$ are shown.

The new equation for the difference is:

$$\epsilon_{exp} \quad = \quad \epsilon_{nl} - \epsilon_l, \tag{7.14}$$

where ϵ_{nl} and ϵ_l are the non-linear and linear differences calculated from equation (7.11). The growth of the exponential filter is now calculated using:

$$\text{growth} \quad = \quad \begin{cases} (\epsilon_{nl} - \epsilon_l + 1) * \left(\frac{\tau}{\tau_i}\right)^{2/3}, & \text{for } \hat{\delta} \\ (\epsilon_{nl} - \epsilon_l + 1) * \left(\frac{\tau}{\tau_i}\right)^{1/3}, & \text{for } \hat{v}_i \end{cases} \tag{7.15}$$

These quantities are illustrated in Figure 7.14. The difference and growth of the boxcar filter could have been calculated in this way, however due to the relative size of ϵ_{nl} and ϵ_l there would have been no noticeable difference.

The ϵ_{exp} values present on the $L = 4166\,\text{Mpc}$ grid are of the same order as the boxcar filter. Whereas the $L = 100\,\text{Mpc}$ grid contains larger differences than the boxcar. However, percent differences first occur on smaller scales, that is $|\tilde{\mathbf{x}}|$ equals $16.67\,\text{Mpc}$ ($|\mathbf{k}| = 6$). While modes that show percent differences at early times are still $10\,\text{Mpc}$.

The ϵ_{exp} over time for modes $|\mathbf{k}| = [1, 6, 12, 18]$ are illustrated in Figure 7.9(b) and (d) for grids $4166\,\text{Mpc}$ and $100\,\text{Mpc}$, respectively. The ϵ_{exp} for modes on the $4166\,\text{Mpc}$ grid remains less than 0.1% for all modes. The modes on the $100\,\text{Mpc}$ grid show a similar behaviour to Figure 7.9(b): where modes $|\mathbf{k}| \leq 8$ have differences less than 1%, and the rest of the modes have some differences in the range $1 - 20\%$.

Along the axis's, the ϵ_{exp} does not show a general trend as k_i increases. The ϵ_{exp} for each mode does not generally increase as time progresses. This indicates that many modes start with a difference to the 'left' and then travel

to the 'right'. By comparing Figure 7.10 and 7.15, the general change in the axis behaviour can be observed: along the x-axis the differences have generally increased, along the y-axis the modes where $k_y < 8$ have increased differences while the rest show a decrease, and along the z-axis some modes have decreased differences but many remain the same.

Figure 7.16 illustrates the norm $\left\|\hat{\delta}\right\|_\tau$ at times $\tau \in [0.25,\ 0.5,\ 0.75,\ 1]$: the average line (solid red) still shows oscillations, which are larger than the boxcar filter for certain modes. There is an increase in the standard deviation envelope for scales ≤ 12.5 Mpc.

Increases in the magnitude of differences and oscillations could be due to the increased number of modes or high-frequency aliasing. If high-frequency aliasing is occurring, the modes affected are $|\mathbf{k}| \geq 11$, see Subsection 5.4.6. These modes have larger standard deviations than before.

To accurately determine whether the smooth filter reduces Gibbs ripples the high-frequency aliasing must be removed.

The norm for each point is now calculated like:

$$\|\mathrm{X}\|_\tau \quad = \quad \epsilon_{nl} - \epsilon_l + 1. \tag{7.16}$$

This ratio is plotted for all points $\mathbf{k} = (k_x, k_y, k_z)$, where the magnitude of the mode $|\mathbf{k}|$ is an integer, at four τ values during the evolution i.e. $\tau \in [0.25,\ 0.5,\ 0.75,\ 1]$ (Figure 7.16). The solid red line represents the average value for the mode $|\mathbf{k}|$, the dashed black lines indicate one standard deviation from the average, and the grey shaded area covers all points within one standard deviation of the average. The graphs look similar to Figure 7.12, including the oscillations noted earlier. This indicates that the exponential filter has not removed the Gibbs ripples.

Since the exponential filter does not obey Orszag's two-thirds rule, the filter may be reducing the Gibbs ripples while introducing high-frequency aliasing. To determine whether this is the case we suggest a comparison between an exponential filter that has been shifted and a boxcar filter with cutoff frequency such that both filters allow the same number of modes through.

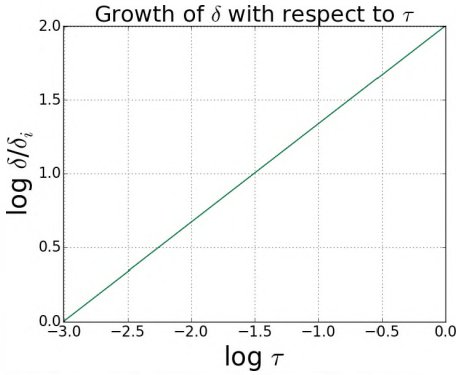

(a) The growth, equation (7.15), of $\dot{\delta}$ for the box size $L = 4166$ Mpc.

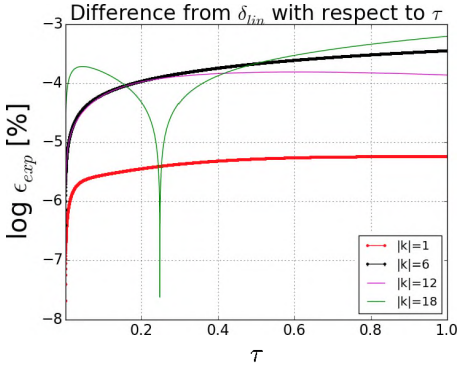

(b) The non-linear difference ϵ_{exp} for the density contrast over time, on grid $L = 4166$ Mpc. Each line represents the difference of a mode $\mathbf{k} = (k_x, k_y, k_z)$, where the magnitude $|\mathbf{k}|$ is: 1 (red), 6 (black), 12 (pink), and 18 (green). Notice how each mode, with the same magnitude $|\mathbf{k}|$, evolves differently.

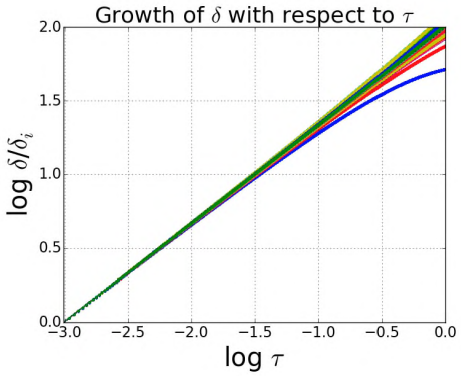

(c) The growth, equation (7.15), of $\dot{\delta}$ for the box size $L = 100$ Mpc.

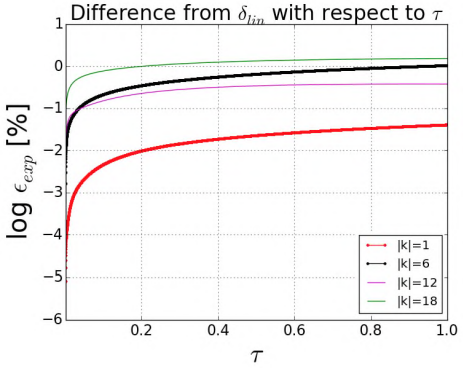

(d) The non-linear difference ϵ_{exp} for the density contrast over time, on grid $L = 100$ Mpc. Each line represents the difference of a mode $\mathbf{k} = (k_x, k_y, k_z)$, where the magnitude $|\mathbf{k}|$ is: 1 (red), 6 (black), 12 (pink), and 18 (green). Notice how each mode, with the same magnitude $|\mathbf{k}|$, evolves differently.

Figure 7.14: The evolution of the data when the exponential filter is applied. Only scales $0 \leq |\mathbf{k}| \leq \frac{N}{3}$ are shown.

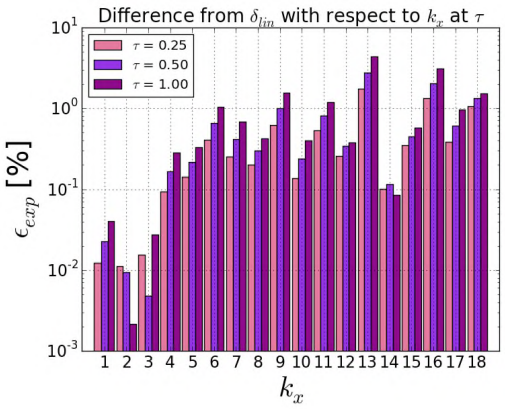

(a) The differences, ϵ_{exp}, for the $\tilde{\delta}$, for modes along the x-axis. Grid $L = 100$ Mpc.

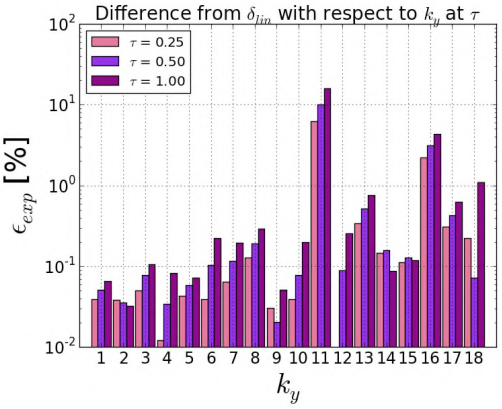

(b) The differences, ϵ_{exp}, for the $\tilde{\delta}$, for modes along the y-axis. Grid $L = 100$ Mpc.

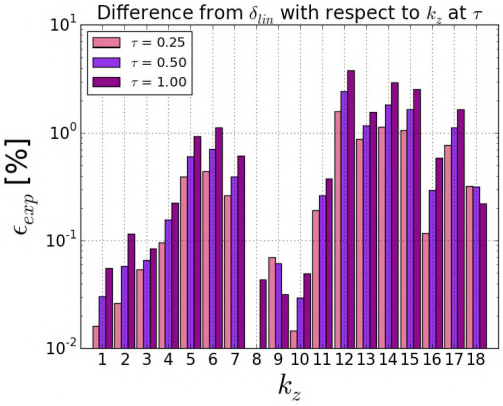

(c) The differences, ϵ_{exp}, for the $\tilde{\delta}$, for modes along the z-axis. Grid $L = 100$ Mpc.

Figure 7.15: The differences, ϵ_{exp}, for the $\tilde{\delta}$ along the x, y and z axis.

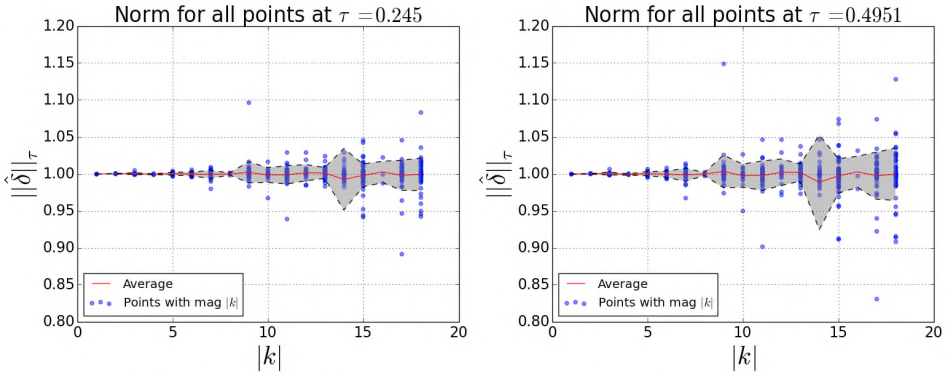

(a) Norm at $\tau \approx 0.25$

(b) Norm at $\tau \approx 0.50$

(c) Norm at $\tau \approx 0.75$

(d) Norm at $\tau \approx 1.00$

Figure 7.16: The norm $\left|\left|\hat{\delta}\right|\right|_\tau$ at particular times for a grid $L = 100\,\text{Mpc}$ are shown. Only integer modes between $0 \leq |\mathbf{k}| \leq \frac{N}{3}$ are shown. The average (solid red line) and standard deviation (dashed black lines) for each mode is shown. The shaded area contains the points enveloped within one standard deviation of the average. Notice that the oscillations are present in the average line and the mode $|\mathbf{k}| = 14$ has a larger standard deviation envelope compared to the boxcar filter.

7.6.4 Removal of Gibbs Ripples

The results have shown that Gibbs ripples are present, however the suggested exponential filter in [1] does not limit the aliasing effects. Although Gibbs ripples may be removed, the filter has introduced high-frequency aliasing. To investigate whether the smooth filter does reduce the Gibbs ripples, consider the shifted-exponential filter equation (5.30) of Section 5.4.6. This filter is illustrated in Figure 7.17.

To compare the effects of Gibbs ripple reduction, consider the shifted-boxcar filter with cut-off frequency $|\mathbf{k}| = \frac{5N}{18} = 15$, see Figure 7.17. The shifted-exponential filter could not be compared to the filter from Section 7.4 since the filters allow through a different number of modes. Since the modes couple when non-linear terms are included, evolving without the contributions for these modes will skew the results.

The modes present on the grids are: $|\mathbf{k}| \leq 15$ for shifted-boxcar filter, and $|\mathbf{k}| \leq 16$ for the shifted-exponential filter. However, not all modes for the exponential filter are multiplied by 1. Modes equivalent to 1 at order $\mathcal{O}\left(10^{-2}\right)$ are $|\mathbf{k}| \leq 10$. The modes $|\mathbf{k}| > 10$ do not experience semi-linear growth, therefore we were unable to reconstructed them correctly.

The slope of the growth for the two shifted filters is shown in Table 7.5, where the growth is calculated by using equation (7.15). The average slopes for the two filters are similar in size for $|\mathbf{k}| \leq 10$.

The largest ϵ_τ for modes $|\mathbf{k}| \leq 10$ are: 13% for the shifted-boxcar filter, and 9% for the shifted-exponential filter. The Gibbs ripples are still present on the shifted exponential filter's average line, however they might be slightly reduced for some modes.

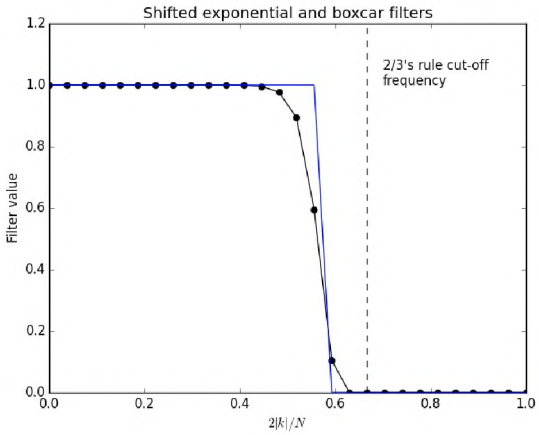

Figure 7.17: The shifted-exponential and boxcar filters compared

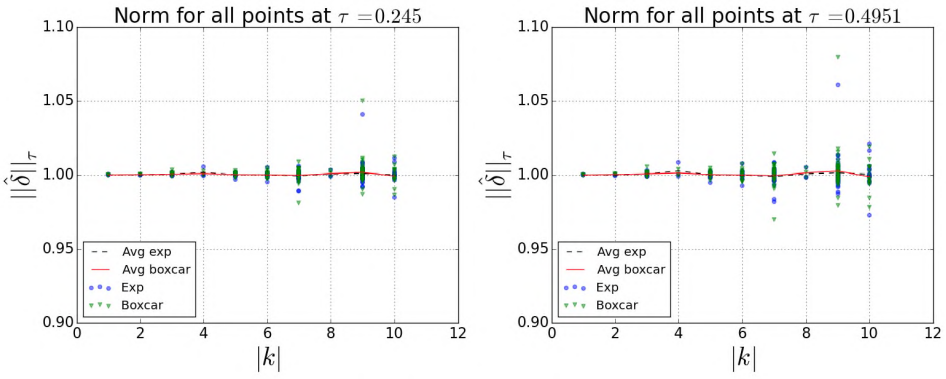

(a) Norm at $\tau \approx 0.25$

(b) Norm at $\tau \approx 0.50$

(c) Norm at $\tau \approx 0.75$

(d) Norm at $\tau \approx 1.00$

Figure 7.18: The norm $\left\|\hat{\delta}\right\|_\tau$ at particular times for a grid $L = 100$ Mpc. Only integer modes $0 \leq |\mathbf{k}| \leq 10$ are shown. The average (solid red and dashed black lines) for each filter is shown. Notice that although the Gibbs ripples might be slightly reduced for the shifted-exponential filter, they are still present.

Table 7.5: Results for growing mode - shifted filters

Shifted-boxcar filter				
Quantity	Average slope of growth		Expected slope	Difference
	$\lvert\mathbf{k}\rvert \in [1,\ldots,10]$	$\lvert\mathbf{k}\rvert \in [11,\ldots,15]$		$\lvert\mathbf{k}\rvert \leq 10$
$\hat{\delta}$	0.666909115	0.666051900	$\frac{2}{3}$	$\epsilon_\tau \leq 13\%$
$\hat{v}_x$	0.333261017	0.333342068	$\frac{1}{3}$	$\epsilon_\tau \leq 8\%$
$\hat{v}_y$	0.333330810	0.333249744	$\frac{1}{3}$	$\epsilon_\tau \leq 8\%$
$\hat{v}_z$	0.333337382	0.333263786	$\frac{1}{3}$	$\epsilon_\tau \leq 8\%$

Shifted-exponential filter				
Quantity	Average slope of growth		Expected slope	Difference
	$\lvert\mathbf{k}\rvert \in [1,\ldots,10]$	$\lvert\mathbf{k}\rvert \in [11,\ldots,13]$		$\lvert\mathbf{k}\rvert \leq 10$
$\hat{\delta}$	0.666764516	14.33251454	$\frac{2}{3}$	$\epsilon_{exp} \leq 9\%$
$\hat{v}_x$	0.333344597	13.62405652	$\frac{1}{3}$	$\epsilon_{exp} \leq 2\%$
$\hat{v}_y$	0.333290361	13.74438222	$\frac{1}{3}$	$\epsilon_{exp} \leq 2\%$
$\hat{v}_z$	0.333366689	13.61942314	$\frac{1}{3}$	$\epsilon_{exp} \leq 2\%$

Chapter 8

Conclusions

The goal of the thesis was to implement a numerical simulation for evolving a Newtonian model of cosmology using spectral methods, verify its stability and convergence, and investigate the affects of aliasing - with a specific comparison between the suggested exponential filter [1].

The spectral method of evolving data on a grid is a natural formulation for the problem of evolving a spectrum of perturbations, and only requires a conversion to physical space when the evolution equations contain non-linear terms - shown in Chapter 5. This spectral method of evolution is both stable and convergent. For the linear and non-linear evolutions the order of convergence was 4 and 3, respectively - see Section 7.3.

The growth, $\frac{\hat{\delta}}{\hat{\delta}_i}$, for the linear evolution was $a(\tau)$, as expected for all modes, see Section 7.4. Deviations from linear behaviour on scales $\sim 8h^{-1}$ Mpc $= 11.42$ Mpc [74] at $z = 0$ were expected. However, when the full non-linear system was evolved, the scales where $|\tilde{\mathbf{x}}| \leq 50$ Mpc showed deviations from linear growth, see Section 7.5.

The spectral method of evolution was sensitive to aliasing effects when non-linear terms were present in the evolution equations, as shown in the no-filter scenario. The growth showed large deviations from linear behaviour, which developed at early times. These differences were only expected on smaller scales, and at later times, however this was not the case when no filter was applied - it was determined that the cause of this unexpected behaviour was high-frequency aliasing (see Section 7.6.1). Percent differences are first observed on the scale where $|\tilde{\mathbf{x}}| = 50$ Mpc, while $|\tilde{\mathbf{x}}| = 33.33$ Mpc is the scale that experiences the first percent differences at high redshift.

To reduce the aliasing artifacts alternate filters were applied to the high-wavenumber modes: the 2/3rd boxcar filter, the exponential filter, and shifted versions of both.

The first filter applied was the 2/3rd boxcar filter (see Section 7.6.2). The percent differences only started on the scale where $|\tilde{\mathbf{x}}| = 33.33$ Mpc, which is an improvement, and the scale where $|\tilde{\mathbf{x}}| = 11.11$ Mpc is the largest mode

where percent differences are observed at high redshifts. It was shown that the aforementioned filter introduced Gibbs ripples, this caused the filter to create oscillations in the data which made the graphs inaccurate.

An exponential filter, following the suggestion of [1] was tested. The smooth profile of the window was expected to reduce the effect of Gibbs ripples (see Section 7.6.3). Unfortunately, in practical use it had the effect of introducing additional high-frequency aliasing effects. The scale where percent differences are first seen is $|\tilde{\mathbf{x}}| = 16.67$ Mpc, while percent differences at high redshift are first observed on the scale where $|\tilde{\mathbf{x}}| = 14.29$ Mpc. The scales where non-linear differences are observed suggests that the filter may have helped improve the differences. This was only a preliminary assumption, and more tests needed to be conducted to verify whether this was the case or not.

To investigate the exponential filter's ability to reduce Gibbs ripples, a shifted-exponential filter was created, which was then compared to a shifted-boxcar filter - see Section 7.6.4.

Due to the shape of the shifted-exponential filter, we were unable to accurately reconstruct the density contrast and velocity for the modes where $|\mathbf{k}| \geq 11$. Therefore, a comparison between the $|\mathbf{k}| < 11$ modes was performed. It was found that the shifted-exponential filter may reduce Gibbs ripples but not significantly.

This suggests that the exponential filter creates high-frequency aliasing and does not significantly reduce Gibbs ripples for the non-linear system studied here, as was suggested in [1].

Based on the results above we conclude that applying a filter is necessary when using spectral methods - primarily due to of high-frequency aliasing. Additionally while the 2/3rd boxcar creates Gibbs ripples, it is more accurate than the exponential filter, and should therefore take preference when performing similar simulations. This decrease in accuracy is due to the exponential filter introducing high-frequency aliasing, if said aliasing could be removed either method would become equally viable. It can also be concluded that a smooth filter is not significantly better, or more accurate, than a boxcar filter - this is supported by the strong similarities shown between the two shifted filters in Section 7.6.4.

As explained above, the spectral method was both efficient and produced the expected growth of the density contrast. The simulation's efficiency is demonstrated by the system on which it was run, which had 16.5 GBs of RAM and 4 CPUs running at 3.5GHz. This set-up took 45 minutes to run the linear system to completion, and 6 hours to complete a run of the non-linear system - both of which were from an initial redshift of $z = 100$, with a time-step of $d\tau = \frac{\tau_i}{10}$. For future work, the code could either be re-written in a lower level language, run on a better system, or parallelised in order to improve the time taken and to allow for larger grids - which would in turn improve the accuracy of the results.

Spectral simulations usually experience problems when handling hydro-effects, such as shocks - these were not observed, but could be investigated in future works.

The cosmological model investigated in this thesis did not contain a cosmo-

logical constant, and was purely contained within the matter dominated era. The affects of this could be investigated in future works via the inclusion of a cosmological constant, evolving the initial data from a higher redshift, or use of a dynamical background spacetime (such as ADM+hydro formalism). Further calculations, and their implementation in numerical simulations, could be done to solve the constraints in GR - this would result in simulating curved spacetimes instead of just the flat spacetime, which would in turn allow for investigations into structural formation in the early universe.

Bibliography

[1] Thomas Y. Hou and Ruo Li. Computing nearly singular solutions using pseudo-spectral methods. 2008.

[2] James Foster and J. David Nightingale. *A Short Course in General Relativity.* Springer, 3 rd edition, 2006.

[3] P. Peter and J. Uzan. *Primordial Cosmology.* Oxford University Press, 2009.

[4] Robert M. Wald. *General Relativity.* The University of Chicago Press, 1984.

[5] Miguel Alcubierre. *Introduction to 3+1 Numerical Relativity.* Oxford University Press, 2008.

[6] Andrew R. Liddle and David H. Lyth. *Cosmological Inflation and Large-Scale Structure.* Cambridge University press, 2000.

[7] F. Bernardeau, S. Colombi, E. Gaztanaga, and R. Scoccimarro. Large-scale structure of the universe and cosmological perturbation theory. arXiv:astro-ph/0112551v1, 2001.

[8] Neta A. Bahcall. Large-scale structure in the universe indicated by galaxy clusters. *Annu. Rev. Astron. Astrophys*, 26:631–86, 1988.

[9] Neta A. Bahcall and William S. Burgett. Are superclusters correlated on a very large scale? *Astrophysical Journal, Part 2 - Letters to the Editor (ISSN 0004-637X)*, 300:L35–L39, 1986.

[10] Misner, Thorne, and Wheeler. *Gravitation.* Freeman, 1973.

[11] Wiki. Picture from "big bang", 2014.

[12] James M. Bardeen. Gauge-invariant cosmological perturbations. *Physical Review D*, 22:1882–1905, 1980.

[13] Wayne Hu and Scott Dodelson. Cosmic microwave background anisotropies. *Annu. Rev. Astron. Astrophys*, 40:171–216, 2002.

[14] Patrick Billingsley. *Probability and Measure.* Wiley-Interscience, 3rd edition, 1995. ISBN 0-471-00710-2.

[15] Laurent Baulieu, Jan de Boer, Boris Pioline, and Eliezer Rabinovici, editors. *String Theory: From Gauge Interactions to Cosmology: Proceedings of the NATO Advanced Study Institute on String Theory: From Gauge Interactions to Cosmology, Carg?se, France, from 7 to 19 June 2004*, volume 208 of *Nato Science Series II.* Springer Science & Business Media, illustrated edition, 2006.

[16] Houjun Mo, Frank van den Bosch, and Simon White. *Galaxy Formation and Evolution.* Cambridge University Press, illustrated edition, 2010.

[17] J. Weller G. Efstathiou S. L. Bridle, A. M. Lewis. Reconstructing the primordial power spectrum. *MNRAS*, 342, 2003.

[18] J. Dunkley, E. Komatsu, M.R. Nolta, D.N. Spergel, D. Larson, G. Hinshaw, L. Page, C.L. Bennett, B. Gold, N. Jarosik, J.L. Weiland, M. Halpern, R.S. Hill, A. Kogut, M. Limon, S.S. Meyer, G.S. Tucker, E. Wollack, and E.L. Wright. Five-year wilkinson microwave anisotropy probe? observations: Likelihoods and parameters from the wmap data. *The Astrophysical Journal Supplement Series*, 180:306–329, 2009.

[19] E. Komatsu, K. M. Smith, J. Dunkley, C. L. Bennett, B. Gold, G. Hinshaw, N. Jarosik, D. Larson, M. R. Nolta, L. Page, D. N. Spergel, M. Halpern, R. S. Hill, A. Kogut, M. Limon, S. S. Meyer, N. Odegard, G. S. Tucker, J. L. Weiland, E. Wollack, and E. L. Wright. Seven-year wilkinson microwave anisotropy probe (wmap1) observations: Cosmological interpretation. *Astrophysical Journal supplement series*, 2010. arXiv:1001.4538v3.

[20] Edmund Bertschinger. Simulations of structure formation in the universe. *Annu. Rev. Astron. Astrophys*, 36:599–654, 1998.

[21] J. A. Peacock. *Cosmological Physics.* Cambridge University press, 1999.

[22] Jaan Einasto. Large scale structure. *New Astronomy Reviews*, 45:355–372, 2001.

[23] Erik Holmberg. On the clustering tendencies among the nebulae. ii. a study of encounters between laboratory models of stellar systems by a new integration procedure. *The Astrophysical Journal*, 94:385–395, 1941.

[24] S. J. Aarseth. Dynamical evolution of clusters of galaxies, i. *MNRAS*, 126:223, 1963.

[25] P.J.E. Peebles. Structure of the coma cluster of galaxies. *The Astrophysical Journal*, 75:13, 1970.

[26] J.R. Bond, G. Efstathiou, and Silk J. Massive neutrinos and the large-scale structure of the universe. *Physical Review Letters*, 45:1980–1984, 1980.

[27] Benjamin Lee and Steven Weinberg. Cosmological lower bound on heavy-neutrino masses. *Physical Review Letters*, 39:165–168, 1977.

[28] J. Cowsik, R.; McClelland. *Physical Review Letters*, 29:669–670, 1972.

[29] Alan H. Guth. Inflationary universe: A possible solution to the horizon and flatness problems. *Physical Review D (Particles and Fields)*, 23:347–356, 1981.

[30] P.J.E. Peebles and J.T. Yu. Primeval adiabatic perturbation in an expanding universe. *Astrophysical Journal*, 162:815, 1970.

[31] J.R. Bond and A.S. Szalay. The collisionless damping of density fluctuations in an expanding universe. *Astrophys.J, Part 1 (ISSN 0004-637X)*, 274:443–468, 1983.

[32] J. M. Bardeen, J.R. Bond, Kaiser N., and A.S. Szalay. The statistics of peaks of gaussian random fields. *Astrophys.J, Part 1 (ISSN 0004-637X)*, 304:15–61, 1986.

[33] G. Efstathiou, M. Davis, C.S. Frenk, and S. D. M. White. Numerical techniques for large cosmological n-body simulations. *The Astrophysical Journal Supplement Series (ISSN 0067-0049)*, 57:241–260, February 1985.

[34] J.A. Peacock and A.F. Heavens. The statistics of maxima in primordial density perturbations. *MNRAS (ISSN 0035-8711)*, 217:805–820, 1985.

[35] G. F. Smoot, C. L. Bennett, A. Kogut, E. L. Wright, J. Aymon, N. W. Boggess, E. S. Cheng, G. de Amici, S. Gulkis, M. G. Hauser, G. Hinshaw, P. D. Jackson, M. Janssen, E. Kaita, T. Kelsall, P. Keegstra, C. Lineweaver, K. Loewenstein, P. Lubin, J. Mather, S. S. Meyer, S. H. Moseley, T. Murdock, L. Rokke, R. F. Silverberg, L. Tenorio, R. Weiss, and D. T. Wilkinson. Structure in the cobe differential microwave radiometer first-year maps. *Astrophys.J, Part 2 - Letters (ISSN 0004-637X)*, 396, 1992.

[36] G. Efstathiou, J. R. Bond, and S. D. M. White. Cobe background radiation anisotropies and large-scale structure in the universe. *MNRAS (ISSN 0035-8711)*, 258, 1992.

[37] E. Bertschinger, A. Dekel, S. M. Faber, A. Dressler, and D. Burstein. Potential, velocity, and density fields from redshift-distance samples: Application - cosmography within 6000 kilometers per second. *Astrophys.J, Part 1 (ISSN 0004-637X)*, 364:370–395, 1990.

[38] H. Ueda, M. Itoh, and Y. Suto. Clusters and groups of galaxies as cosmological probes. *Astrophys.J, Part 1 (ISSN 0004-637X)*, 408:3–16, 1993.

[39] N. A. Bahcall and R. Cen. Galaxy clusters and cold dark matter - a low-density unbiased universe? *Astrophys.J, Part 2 - Letters (ISSN 0004-637X)*, 398:L81–L84, 1992.

[40] J. M. Colberg, S. D. M. White, N. Yoshida, T. J. MacFarland, A. Jenkins, C. S. Frenk, F. R. Pearce, A. E. Evrard, H. M. P. Couchman, G. Efstathiou, J. A. Peacock, and P.A. Thomas. Clustering of galaxy clusters in cdm universes. arXiv:astro-ph/0005259v2, 2000.

[41] A.E. Evrard, T.J. MacFarland, H.M.P. Couchman, J.M. Colberg, N. Yoshida, S.D.M. White, A. Jenkins, C.S. Frenk, F.R. Pearce, J.A. Peacock, and P.A. Thomas. Galaxy clusters in hubble volume simulations: Cosmological constraints from sky survey populations. arXiv:astro-ph/0110246v2, 2002.

[42] S. Gottlöber, G. Yepes, A. Khalatyan, R. Sevilla, and V. Turchaninov. Dark and baryonic matter in the marenostrum universe. arXiv:astro-ph/0610622v2, 2006.

[43] Yan-Chuan Cai, Shaun Cole, Adrian Jenkins, and Carlos S. Frenk. Full-sky map of the isw and rees-sciama effect from gpc simulations. arXiv: 1003.0974v2, 2010.

[44] Volker Springel, Naoki Yoshida, and Simon D.M. White. Gadget: a code for collisionless and gasdynamical cosmological simulations. *New Astronomy*, 6:79–117, 2001.

[45] Peter A. Thomas, Jorg M. Colberg, Hugh M. P. Couchman, George P. Efstathiou, Carlos S. Frenk, Adrian R. Jenkins, Alistair H. Nelson, Roger M. Hutchings, John A. Peacock, Frazer R. Pearce, and Simon D. M. White (the Virgo Consortium). The structure of galaxy clusters in different cosmologies. *MNRAS*, 2008.

[46] A. Jenkins, C. S. Frenk, F. R. Pearce, P. A. Thomas, J. M. Colberg, S. D. M. White, H. M. P. Couchman, J. A. Peacock, G. Efstathiou67, and A. H. Nelson (The Virgo Consortium). Evolution of structure in cold dark matter universes. *Astrophys.J*, 499:20, 1998.

[47] Yann Rasera, Pier-Stefano Corasaniti, Jean-Michel Alimi, Vincent Bouillot, Vincent Reverdy, and Ir?ne Balm?s. Cosmic variance limited baryon acoustic oscillations from the deus-fur ?cdm simulation. *MNRAS*, 440:1420, 2014.

[48] The virgo consortium: For cosmological supercomputer simulations. http://www.virgo.dur.ac.uk/.

[49] Guinevere Kauffmann, Joerg M. Colberg, Antonaldo Diaferio, and Simon D. M. White. Clustering of galaxies in a hierarchical universe - i. methods and results at z =0. *MNRAS*, 303:188–206, 1999.

[50] Guinevere Kauffmann, Joerg M. Colberg, Antonaldo Diaferio, and Simon D. M. White. Clustering of galaxies in a hierarchical universe - ii. evolution to high redshift. *MNRAS*, 307:529–536, 1999.

[51] H.M.P. Couchman, P.A. Thomas, and F.R. Pearce. Hydra: An adaptive-mesh implementation of pppm-sph. *Astrophys.J*, 452:797, 1995.

[52] G. Lemson and the Virgo Consortium. Halo and galaxy formation histories from the millennium simulation: Public release of a vo-oriented and sql-queryable database for studying the evolution of galaxies in the lambdacdm cosmogony. 2006.

[53] Gerard Lemson and the Virgo Consortium. Halo and galaxy formation histories from the millennium simulation. http://wwwmpa.mpa-garching.mpg.de/millennium/, 10 2012.

[54] Joop Schaye, Robert A. Crain, Richard G. Bower, Michelle Furlong, Matthieu Schaller, Tom Theuns, Claudio Dalla Vecchia, Carlos S. Frenk, I. G. McCarthy, John C. Helly, Adrian Jenkins, Y. M. Rosas-Guevara, Simon D. M. White, Maarten Baes, C. M. Booth, Peter Camps, Julio F. Navarro, Yan Qu, Alireza Rahmati, Till Sawala, Peter A. Thomas, and James Trayford. The eagle project: simulating the evolution and assembly of galaxies and their environments. *MNRAS*, 446:521–554, 2015.

[55] Volker Springel. The cosmological simulation code gadget-2. *MNRAS*, 364:1105–1134, 2005.

[56] Wojciech A. Hellwing, Carlos S. Frenk, Marius Cautun, Sownak Bose, John Helly, Adrian Jenkins, Till Sawala, and Maciej Cytowski. The copernicus complexio: a high-resolution view of the small-scale universe. *preprint May 2015.*

[57] Sownak Bose, Wojciech A. Hellwing, Carlos S. Frenk, Adrian Jenkins, Mark R. Lovell, John C. Helly, and Baojiu Li. The copernicus complexio: Statistical properties of warm dark matter haloes. preprint July 2015.

[58] C. S. Frenk, J. M. Colberg, H. M. P. Couchman, G. Efstathiou, A. E. Evrard, A. Jenkins, T. J. MacFarland, B. Moore, J. A. Peacock, F. R. Pearce, P. A. Thomas, S. D. M. White, and N. Yoshida. Public release of n-body simulation and related data by the virgo consortium. *MNRAS*, 2008.

[59] Deus consortium. http://www.deus-consortium.org/, 9 2015.

[60] R Teyssier. Cosmological hydrodynamics with adaptive mesh refinement. a new high resolution code called ramses. *Astronomy and Astrophysics*, 385:337–364, 2002.

[61] H. M. P. Couchman. Mesh-refined p3m - a fast adaptive n-body algorithm. *Astrophys.J*, 368:L23–L26, 1991.

[62] DEUSS consortium. Deuss consortium run. http://www.deus-consortium.org/. [viewed 7 Sep 2015].

[63] Thomas Guillet and Romain Teyssier. A simple multigrid scheme for solving the poisson equation with arbitrary domain boundaries. *J.Comput.Phys*, 230:4756–4771, 2011.

[64] D. N. Spergel, R. Bean, O. Doré, M. R. Nolta, C. L. Bennett, J. Dunkley, G. Hinshaw, N. Jarosik, E. Komatsu, L. Page, H. V. Peiris, L. Verde, M. Halpern, R. S. Hill, A. Kogut, M. Limon, S. S. Meyer, N. Odegard, G. S. Tucker, J. L. Weiland, E. Wollack, and E. L. Wright. Wilkinson microwave anisotropy probe (wmap) three year results: Implications for cosmology. *Astrophys. J.Suppl*, 170:377, 2007.

[65] S. Prunet, C. Pichon, D. Aubert, D. Pogosyan, R. Teyssier, and S. Gottloeber. Initial conditions for large cosmological simulations. *ApJS*, 178:179–188, 2008.

[66] Roman Scoccimarro. Transients from initial conditions: a perturbative analysis. *MNRAS*, 299:1097–1118, 1998.

[67] M. Crocce, S. Pueblas, and R. Scoccimarro. Transients from initial conditions in cosmological simulations. *MNRAS*, 373:369–381, 2006.

[68] J. S. Bagla and S. Ray. Comments on the size of the simulation box in cosmological n-body simulations. *MNRAS*, 358:1076, 2005.

[69] Katrin Heitmann, Martin White, Christian Wagner, Salman Habib, and David Higdon. The coyote universe. i. precision determination of the nonlinear matter power spectrum. *Astrophys.J*, 715:104, 2010.

[70] Ryuichi Takahashi, Naoki Yoshida, Takahiko Matsubara, Naoshi Sugiyama, Issha Kayo, Takahiro Nishimichi, Akihito Shirata, Atsushi Taruya, Shun Saito, Kazuhiro Yahata, and Yasushi Suto. Simulations of baryon acoustic oscillations - i. growth of large-scale density fluctuations. *MNRAS*, 389:1675–1682, 2008.

[71] R. Takahashi, N. Yoshida, M. Takada, T. Matsubara, N. Sugiyama, I. Kayo, T. Nishimichi, A. Shirata, A. Taruya, and S. Saito. Simulations of baryon acoustic oscillations ii: Covariance matrix of the matter power spectrum. *Astrophys.J*, 700:479–490, 2009.

[72] A. A. Penzias and R. W. Wilson. A measurement of excess antenna temperature at 4080 mc/s. *Astrophysical Journal*, 142:419–421, 1965.

[73] Britt Griswold. Wilkinson microwave anisotropy probe. http://map.gsfc.nasa.gov/, 12 2012.

[74] G. Hinshaw, D. Larson, E. Komatsu, D. N. Spergel, C. L. Bennett, J. Dunkley, M. R. Nolta, M. Halpern, R. S. Hill, N. Odegard, L. Page, K. M. Smith, J. L. Weiland, B. Gold, N. Jarosik, A. Kogut, M. Limon, S. S. Meyer, G. S. Tucker, E. Wollack, and E. L. Wright. Nine-year wilkinson microwave anisotropy probe (wmap) observations: Cosmological parameter results. *The Astrophysical Journal Supplement Series*, 208, 2013.

[75] Daniel J. Eisenstein, Hee-Jong Seo, and Martin White. On the robustness of the acoustic scale in the low-redshift clustering of matter. *The Astrophysical Journal*, 664:660–674, 2007.

[76] Bruce A. Bassett and RenŽee Hlozek. Baryon acoustic oscillations. *Dark Energy: Observational and Theoretical Approaches*, page 246, 2010.

[77] J.M. Alimi, A. Fuzfa, V. Boucher, Y. Rasera, J. Courtin, and P.S. Corasaniti. Imprints of dark energy on cosmic structure formation i) realistic quintessence models and the non-linear matter power spectrum. *MNRAS*, 401:775, 2010.

[78] Lloyd N. Trefethen. *Spectral Methods in Matlab.* SIAM, Philadelphia, 2000.

[79] Andrei D. Polyanin and Alexander V. Manzhirov. *Handbook of Mathematics for Engineers and Scientists.* CRC Press, illustrated edition, 2006.

[80] Jose Unpingco. *Python for Signal Processing.* Springer.

[81] C. Runge. Ueber die numerische auflösung von differentialgleichungen. *Math. Ann.*, 46:167–178, 1895. (German).

[82] W. Kutta. Beitrag zur naherungsweisen integration von differentialgleichungen. *Zeit. Math. Physik*, 46:435–453, 1901.

[83] J. C. Butcher. Implicit runge-kutta processes. *Mathematics of Computation*, 18:50–64, 1964.

[84] E. Hairer, S.P. Norsett, and G. Wanner. *Solving Ordinary Differential Equations I: Nonstiff Problems.* Springer-Verlag, 2nd edition, 1991.

[85] R Courant, K Friedrichs, and H Lewy. Über die partiellen differenzengleichungen der mathematischen physik. *Mathematische Annalen*, 100:32–74, 1928.

[86] R Courant, K Friedrichs, and H Lewy. On the partial difference equations of mathematical physics. *IBM Journal of Research and Development*, 11:215–234, 1967.

[87] Richard H. Pletcher, John C. Tannehill, and Dale Anderson. *Computational Fluid Mechanics and Heat Transfer.* CRC Press, 3 edition, 2012.

[88] John P. Boyd. *Chebyshev and Fourier Spectral Methods.* DOVER Publications, 2 edition, 2000.

[89] Jens Jasche, Francisco S. Kitaura, and Torsten A. Enßlin. Digital signal processing in cosmology. *MNRAS*, 000:1–17, 2006.

[90] Don P. Mitchell and Arun N. Netravali. Reconstruction filters in computer graphics.

[91] Norman A. Phillips. The general circulation of the atmosphere: a numerical experiment. *Q. J. R. Meteorol. Soc.*, 82(352):123–164, 1956.

[92] G.S. Patterson and Steven A. Orszag. Spectral calculations of isotropic turbulence: Efficient removal of aliasing interactions. *Phys. Fluids*, 14:2538, 1971.

[93] Steven A. Orszag. On the elimination of aliasing in finite-differenceschemes by filtering high-wavenumber components. *Journal of the Atmospheric Sciences*, 28:1074, 1971.

[94] C. Canuto, M.Y. Hussaini, A. Quarteroni, and T.A. Zang. *Spectral Methods Fundamentals in Single Domains.* Springer, 2006.

[95] C. Canuto, M.Y. Hussaini, A. Quarteroni, and T.A. Zang. *Spectral Methods in Fluid Dynamics.* Springer, 1988.

[96] John C. Bowman. How important is dealiasing for turbulence simulations. www.math.ualberta.ca/ bowman/talks/, September 2014.

[97] J.C. Bowman and M. Roberts. Efficient dealiased convolutions without padding. *SIAM J. Sci. Comput.*, 2011.

[98] A.J. Jerri. *The Gibbs Phenomenon in Fourier Analysis, Splines and Wavelet Approximations.* Mathematics and Its Applications. Springer, 1998.

[99] A. Zygmund. *Trigonometric Series*, volume 1 & 2. Cambridge University press, 3rd edition, 2002.

[100] Nora Bretón, Jorge L. Cervantes-Cota, and Marcelo Salgado, editors. *The Early Universe and Observational Cosmology*, volume 646. Springer Science & Business Media, 2004.

[101] B. Lautrup. *Physics of Continuous Matter, Second Edition: Exotic and Everyday Phenomena in the Macroscopic World.* CRC Press, 2nd edition, 2011.

[102] Barbara Ryden. *Introduction to Cosmology.* Addison-Wesley, 2006.

[103] Li Shoufu. Stability and b-convergence of general linear methods. *Journal of Computational and Applied Mathematics*, 28:281–296, 1989.

[104] P. Watts and P. Coles. Statistical cosmology with quadratic density fields. *MNRAS*, 338:806–815, 2003.

Part III

Calculations/Appendices

Appendix A

Time dependent variables

Beginning with the Friedmann and conservation equations, equation (3.18) and (3.20) respectively. The equation of state is given by equation (3.21). This is substituted into equation (3.20):

$$\begin{aligned} \frac{\dot{\rho}}{\rho} &= -3\left(1+w\right)H \\ &= -3\left(1+w\right)\frac{\dot{a}}{a}. \end{aligned} \tag{A.1}$$

Then integrated on both sides with respect to time:

$$\frac{\rho}{\rho_0} = \left(\frac{a}{a_0}\right)^{-3(1+w)}, \tag{A.2}$$

where both quantities have been normalised with respect to their values at the current epoch. a_0 is arbitrary so it is set to unity. There are only a few simple cases where the expression for a in terms of the time can be determined. The case where $K = \Lambda = 0$ is chosen. Which simplifies equation (3.18) to:

$$\begin{aligned} H^2 &= \frac{\kappa}{3}\rho \\ &= \frac{\kappa}{3}\rho_0 a^{-3(1+w)} \\ H &= \pm\sqrt{\frac{\kappa}{3}\rho_0}\, a^{-3(1+w)/2}. \end{aligned} \tag{A.3}$$

The positive case is chosen because it corresponds to an expanding universe. Using the definition of H:

$$\begin{aligned}
\frac{\dot{a}}{a} &= \sqrt{\frac{\kappa}{3}\rho_0}a^{-3(1+w)/2} \\
\dot{a} &= \sqrt{\frac{\kappa}{3}\rho_0}a^{-(1+3w)/2} \\
a^{(1+3w)/2}\dot{a} &= \sqrt{\frac{\kappa}{3}\rho_0}. \qquad \text{(A.4)}
\end{aligned}$$

This can be integrated with respect to time to get:

$$\begin{aligned}
\frac{2}{3(1+w)}\left[a^{3(1+w)/2}\right]_{a_0}^{a} &= \sqrt{\frac{\kappa}{3}\rho_0}\left[t-t_0\right] \\
\frac{2}{3(1+w)}\left[a^{3(1+w)/2}-1\right] &= \sqrt{\frac{\kappa}{3}\rho_0}\left[t-t_0\right] \\
\frac{2}{3(1+w)}a^{3(1+w)/2} &= \sqrt{\frac{\kappa}{3}\rho_0}t - \sqrt{\frac{\kappa}{3}\rho_0}t_0 + \frac{2}{3(1+\omega)}. \qquad \text{(A.5)}
\end{aligned}$$

Notice that if the following are set $H = H_0$, $a = a_0 = 1$ and $K = \Lambda = 0$ in equation (3.18) then the density is given by $\frac{\kappa}{3}\rho_0 = H_0^2$. So the expression above becomes:

$$\frac{2}{3(1+w)}a^{3(1+w)/2} = H_0 t - H_0 t_0 + \frac{2}{3(1+w)}. \qquad \text{(A.6)}$$

Since $a_0 = 1$ the Hubble parameter is given by $H_0 = \frac{2}{3(1+w)}\frac{1}{t_0}$. After some more manipulation the expression for a is:

$$a(t) = \left(\frac{t}{t_0}\right)^{2/3(1+w)}. \qquad \text{(A.7)}$$

Consider that $t_0 = 13.76 * 10^9 yr$ [19] and the initial redshift is 100. Using the relationship between the scale-factor and the redshift [3]:

$$\begin{aligned}
\frac{a_0}{a} &= 1+z \\
\frac{1}{a} &= 101.
\end{aligned}$$

Using equation (A.7) and pressure-less matter, i.e. $w = 0$, the starting time is $t = 1.35 * 10^7 yr$.

Appendix B

Correlation function

Beginning with the correlation function of Section 3.1, equation (3.4) [3]. Assuming statistical isotropy and homogeneity, the correlation function depends only on $r \equiv |\mathbf{r}|$, i.e. equation (3.5) [3, 7].

The field, $g(\mathbf{x})$, is usually written in terms of its Fourier modes, $g(\mathbf{k})$, [3, 7], the Fourier and inverse Fourier transform pairs for a field are given by equations (6.53) and (6.54) respectively. This implies that the quantities $g(\mathbf{k})$ are complex random variables.

The quantity $g(\mathbf{x})$ is a real-valued field [3, 7] so $g_{\mathbf{k}}$ needs to satisfy the conjunction relation:

$$g_{\mathbf{k}}^{\star} = g_{-\mathbf{k}}. \tag{B.1}$$

The random field is thus completely characterized by the statistical properties of the random variables $g_{\mathbf{k}}$. The correlators are computed in Fourier space, [3, 6]:

$$\begin{aligned}
\langle g_{\mathbf{k}} g_{\mathbf{k}'} \rangle &= \int \langle g(\mathbf{x})\, g(\mathbf{x}+\mathbf{r}) \rangle \exp\left[-i(\mathbf{k}+\mathbf{k}')\cdot\mathbf{x} - i\mathbf{k}'\cdot\mathbf{r}\right] \frac{d^3\mathbf{x}}{(2\pi)^{3/2}} \frac{d^3\mathbf{r}}{(2\pi)^{3/2}} \\
&= \frac{1}{(2\pi)^3} \int \xi(r) \exp\left[-i(\mathbf{k}+\mathbf{k}')\cdot\mathbf{x} - i\mathbf{k}'\cdot\mathbf{r}\right] d^3\mathbf{x} d^3\mathbf{r} \\
&= \delta_D(\mathbf{k}+\mathbf{k}') \int d^3\mathbf{r} \xi(r) \exp(i\mathbf{k}\cdot\mathbf{r}) \\
&\equiv \delta_D(\mathbf{k}+\mathbf{k}')\, P_g(k),
\end{aligned} \tag{B.2}$$

where δ_D is the Dirac distribution in D dimensions, not to be confused with the density contrast, and $P_g(k)$ is by definition the power spectrum of the field g.

Then we have the relation [6]:

$$P_g \equiv L^3 \left\langle |g_{\mathbf{k}}|^2 \right\rangle = \frac{2\pi^2}{k^3} \mathcal{P}_g(k), \tag{B.3}$$

because [6]:

$$\mathcal{P}_g(k) \equiv \left(\frac{L}{2\pi}\right)^3 4\pi k^3 \left\langle |g_{\mathbf{k}}|^2 \right\rangle = 8\pi \left(\frac{L}{2\pi}\right)^3 k^3 \sigma^2. \tag{B.4}$$

This σ^2 is put into the Gauss or Rayleigh distribution.

There is another method where the Fourier transform is defined by [34]:

$$g(\mathbf{x}) = \frac{V_u}{(2\pi)^3} \int g_{\mathbf{k}} \exp(-i\mathbf{k}\cdot\mathbf{x})\, d^3k, \tag{B.5}$$

$$g_{\mathbf{k}} = \frac{1}{V_u} \int g(\mathbf{x}) \exp(i\mathbf{k}\cdot\mathbf{x})\, d^3x. \tag{B.6}$$

Then the factor of V_u is included in the probability distribution, i.e. [34, 104]:

$$\mathbf{P}(g) = \sqrt{\frac{V_u}{2\pi\sigma^2}} \exp\left(-\frac{g^2 V_u}{2\sigma^2}\right). \tag{B.7}$$

The grid constructed in this thesis is $[0,\, 2\pi]$ which implies $V_u = (2\pi)^3$. If the factor of V_u is included the same linear to non-linear behaviour is observed.

This is similar to [7] which set:

$$g(\mathbf{x}) = \int g_{\mathbf{k}} \exp(-i\mathbf{k}\cdot\mathbf{x})\, d^3k, \tag{B.8}$$

$$g_{\mathbf{k}} = \frac{1}{(2\pi)^3} \int g(\mathbf{x}) \exp(i\mathbf{k}\cdot\mathbf{x})\, d^3x, \tag{B.9}$$

and then defined the power spectrum to be smaller by a factor of $(2\pi)^3$. So:

$$P_g(k) = \frac{1}{4\pi k^3} \mathcal{P}_g(k). \tag{B.10}$$

Appendix C

Rayleigh and Gauss equivalence

Consider a complex number $z = u + iv$ and where the magnitude is set to x. The real and imaginary parts are Gaussian distributed:

$$f_U(u) = \frac{1}{\sqrt{2\pi\sigma^2}} \exp\left(\frac{-u^2}{2\sigma^2}\right), \tag{C.1}$$

where σ^2 is the variance or spectrum. v is defined by a similar expression. For these distributions it is assumed that the real and imaginary parts have the same spectrum.

To find the distribution of the magnitude of z, i.e. x, the above equations are multiplied and integrated:

$$\begin{aligned} f(x,\sigma) &= \frac{1}{2\pi\sigma^2} \int_{-\infty}^{\infty} du \int_{-\infty}^{\infty} dv \exp\left(\frac{-u^2}{2\sigma^2}\right) \\ &\quad \exp\left(\frac{-v^2}{2\sigma^2}\right) \delta\left(x - \sqrt{u^2+v^2}\right), \end{aligned} \tag{C.2}$$

which is simpler to integrate in polar coordinates, $rdrd\theta = dudv$ where $r^2 = u^2 + v^2$. So the above becomes:

$$
\begin{aligned}
f(x,\sigma) &= \frac{1}{2\pi\sigma^2}\int_0^{2\pi} d\theta \int_0^{\infty} \exp\left(\frac{-u^2}{2\sigma^2}\right)\exp\left(\frac{-v^2}{2\sigma^2}\right)\delta\left(x-\sqrt{u^2+v^2}\right) r dr \\
&= \frac{1}{\sigma^2}\int_0^{\infty} \exp\left(\frac{-u^2}{2\sigma^2}-\frac{v^2}{2\sigma^2}\right)\delta(x-r)\, r dr \\
&= \frac{1}{\sigma^2}\int_0^{\infty} \exp\left(\frac{-\left(u^2+v^2\right)}{2\sigma^2}\right)\delta(x-r)\, r dr \\
&= \frac{1}{\sigma^2}\int_0^{\infty} \exp\left(\frac{-r^2}{2\sigma^2}\right)\delta(x-r)\, r dr \\
&= \frac{x}{\sigma^2}\exp\left(\frac{-x^2}{2\sigma^2}\right). \qquad \text{(C.3)}
\end{aligned}
$$

The integration is simple since the only time the function is none zero is when $x = r$ because $\delta(k) \neq 0$ only when $k = 0$.

The last expression is the Rayleigh distribution. Therefore the initial data can either take random Gaussian values for the real and imaginary parts or use a random Rayleigh value for the magnitude of the complex number and then choose a random angle.

Notice that σ^2 in each of the random gauss functions is the same as the one seen in the Rayleigh function. This is counter intuitive since the spectrum for z is the same as the spectrum for x and is double the spectrum for u and v.

If X is a complex random variable, $X = U + Vi$, then its variance is defined as:

$$
\mathrm{Var}(X) = \mathbb{E}\left((X-\mu)\overline{(X-\mu)}\right), \qquad \text{(C.4)}
$$

where $\overline{c}$ is the complex conjugate of c and μ is the mean of the distribution. In this case the mean $\mu = 0$, which gives:

$$
\begin{aligned}
\mathrm{Var}(X) &= \mathbb{E}\left(X\overline{X}\right) \\
&= \mathbb{E}\left(|X|^2\right) \\
&= \mathbb{E}\left(U^2+V^2\right) \\
&= \mathbb{E}\left(U^2\right)+\mathbb{E}\left(V^2\right) \\
&= \mathrm{Var}(U)+\mathrm{Var}(V).
\end{aligned}
$$

A similar thing can be done for the Rayleigh distribution however the mean is not zero [$\mu = \sigma\sqrt{\frac{\pi}{2}}$]. If is used $X = R\exp(i\theta)$:

$$\begin{aligned}
\operatorname{Var}(X) &= \mathbb{E}\left(|X|^2\right) \\
&= \mathbb{E}\left(R^2\right) \\
&= \mathbb{E}\left(R^2\right) - \mathbb{E}(R)^2 + \mathbb{E}(R)^2 \\
&= \operatorname{Var}(R) + \frac{\pi}{2}\sigma^2.
\end{aligned}$$

Since $\operatorname{Var}(R) = \frac{4-\pi}{2}\sigma^2$ the variance of X is $\operatorname{Var}(X) = 2\sigma^2$.

Appendix D

Deriving the evolution equations in comoving coordinates

D.1 Comoving coordinates

This section details the transformation of the Euler, Poisson and continuity equations from stationary coordinates, $\mathbf{x}$, to comoving coordinates, $\check{\mathbf{x}}$.

The Euler, Poisson and continuity equations in stationary coordinates are given by equation (6.6), (6.19) and (6.5). These equations will be re-written in the comoving coordinate variables $\mathbf{u}$, the peculiar velocity, and Φ, the peculiar potential. The relationship between the velocity and peculiar velocity is given by equation (6.4).

The relationship between the potential and the peculiar potential is:

$$\Psi = \Phi - \frac{1}{2}a\ddot{a}\check{\mathbf{x}}^2. \tag{D.1}$$

In all the above equations, a refers to the scale factor of the universe and a dot above a variable refers to a derivative by time, t. The gradient with respect to r becomes:

$$\nabla = \frac{1}{a}\nabla_{\check{\mathbf{x}}}. \tag{D.2}$$

The derivatives with respect to time evaluated at a particular position $\mathbf{r}$ become:

$$\frac{\partial}{\partial t}|_{\mathbf{r}} = \frac{\partial}{\partial t}|_{\mathbf{x}} - \frac{\dot{a}}{a}\left(\mathbf{x}\cdot\nabla_{\mathbf{x}}\right). \tag{D.3}$$

D.1.1 Euler equation:

The Euler equation during matter domination is:

$$\frac{\partial \mathbf{v}}{\partial t} + (\mathbf{v}\cdot\nabla)\,\mathbf{v} \;=\; -\nabla\Psi. \tag{D.4}$$

The pressure term is removed because the fluid is pressure-less. The conversion to comoving coordinates for each term separately is as follows. The first term on the left of equation (D.4) becomes:

$$\begin{aligned}\frac{\partial \mathbf{v}}{\partial t} &= \frac{\ddot{a}}{a}\mathbf{r} - \left(\frac{\dot{a}}{a}\right)^2 \mathbf{r} + \frac{\partial \mathbf{u}}{\partial t}|_{\mathbf{x}} - \frac{\dot{a}}{a}\,(\mathbf{x}\cdot\nabla_{\check{\mathbf{x}}})\,\mathbf{u} \\ &= \ddot{a}\mathbf{x} - \frac{\dot{a}^2}{a}\mathbf{x} + \frac{\partial \mathbf{u}}{\partial t}|_{\mathbf{x}} - \frac{\dot{a}}{a}\,(\mathbf{x}\cdot\nabla_{\check{\mathbf{x}}})\,\mathbf{u},\end{aligned} \tag{D.5}$$

and the second term on the left becomes:

$$\begin{aligned}(\mathbf{v}\cdot\nabla)\,\mathbf{v} &= \left[\left(\frac{\dot{a}}{a}\mathbf{r}+\mathbf{u}\right)\cdot\nabla\right]\left(\frac{\dot{a}}{a}\mathbf{r}+\mathbf{u}\right) \\ &= \left(\frac{\dot{a}}{a}\mathbf{r}\cdot\nabla + \mathbf{u}\cdot\nabla\right)\left(\frac{\dot{a}}{a}\mathbf{r}+\mathbf{u}\right) \\ &= \frac{\dot{a}}{a}\,(\mathbf{r}\cdot\nabla)\left(\frac{\dot{a}}{a}\mathbf{r}+\mathbf{u}\right) + (\mathbf{u}\cdot\nabla)\left(\frac{\dot{a}}{a}\mathbf{r}+\mathbf{u}\right).\end{aligned} \tag{D.6}$$

Since $(\mathbf{r}\cdot\nabla)\,\mathbf{r} = \mathbf{r}$ and $(\mathbf{u}\cdot\nabla)\,\mathbf{r} = \mathbf{u}$, the above is re-expressed in terms of $\mathbf{x}$ as:

$$\begin{aligned}(\mathbf{v}\cdot\nabla)\,\mathbf{v} &= \left(\frac{\dot{a}}{a}\right)^2 \mathbf{r} + \frac{\dot{a}}{a}\,(\mathbf{r}\cdot\nabla)\,\mathbf{u} + \frac{\dot{a}}{a}\mathbf{u} + (\mathbf{u}\cdot\nabla)\,\mathbf{u} \\ &= \frac{\dot{a}^2}{a}\mathbf{x} + \frac{\dot{a}}{a}\,(\mathbf{x}\cdot\nabla_{\check{\mathbf{x}}})\,\mathbf{u} + \frac{\dot{a}}{a}\mathbf{u} + (\mathbf{u}\cdot\nabla)\,\mathbf{u}.\end{aligned} \tag{D.7}$$

The term on the right of equation (D.4) becomes:

$$\begin{aligned}\nabla\Psi &= \frac{1}{a}\nabla_{\check{\mathbf{x}}}\left(\Phi - \frac{1}{2}a\ddot{a}\check{\mathbf{x}}^2\right) \\ &= \frac{1}{a}\nabla_{\check{\mathbf{x}}}\Phi - \frac{1}{2}\ddot{a}\nabla_{\check{\mathbf{x}}}\check{\mathbf{x}}^2 \\ &= \frac{1}{a}\nabla_{\check{\mathbf{x}}}\Phi - \ddot{a}\check{\mathbf{x}}.\end{aligned} \tag{D.8}$$

After combining all three terms, the Euler equation in comoving coordinates is:

$$\frac{\partial \mathbf{u}}{\partial t} + \frac{1}{a}\,(\mathbf{u}\cdot\nabla_{\check{\mathbf{x}}})\,\mathbf{u} + \frac{\dot{a}}{a}\mathbf{u} \;=\; -\frac{1}{a}\nabla_{\check{\mathbf{x}}}\Phi. \tag{D.9}$$

D.1.2 Poisson equation:

The Poisson equation, equation (6.19), can be rewritten in comoving coordinates by using the relationship between the potential and peculiar potential. The Laplacian of equation (D.1) is:

$$\begin{aligned} \triangle_{\mathbf{x}}\Phi &= \triangle_{\check{\mathbf{x}}}\left(\Psi + \frac{1}{2}a\ddot{a}\check{\mathbf{x}}^2\right) \\ &= \triangle_{\check{\mathbf{x}}}\Psi + \frac{1}{2}\triangle_{\check{\mathbf{x}}}a\ddot{a}\check{\mathbf{x}}^2. \end{aligned} \tag{D.10}$$

Using the original Poisson equation and remembering that the Laplacian becomes $\triangle = \frac{1}{a^2}\triangle_{\check{\mathbf{x}}}$, the Poisson equation in comoving coordinates is:

$$\begin{aligned} \triangle_{\check{\mathbf{x}}}\Phi &= 4\pi G\rho a^2 + \frac{1}{2}a\ddot{a}6 \\ &= 4\pi G\rho a^2 + 3a\left(-\frac{4\pi G}{3}\bar{\rho}a\right) \\ &= 4\pi G a^2\left(\rho - \bar{\rho}\right), \end{aligned} \tag{D.11}$$

where ρ is the physical density not the comoving density and $\bar{\rho}$ is the portion of the density that is only dependent on time.

D.1.3 Continuity equation:

The continuity equation can be written in comoving coordinates by converting each term. The first term in equation (6.5) becomes:

$$\frac{\partial\rho\left(\mathbf{r},t\right)}{\partial t}|_{\mathbf{r}} = \frac{\partial\rho\left(\mathbf{x},t\right)}{\partial t}|_{\mathbf{x}} - \frac{\dot{a}}{a}\mathbf{x}\cdot\left[\nabla_{\check{\mathbf{x}}}\rho\left(\mathbf{x},t\right)\right]. \tag{D.12}$$

While the second term becomes:

$$\begin{aligned} \nabla\cdot\left(\rho\mathbf{v}\right) &= \rho\left[\nabla\cdot\mathbf{v}\right] + \mathbf{v}\left[\nabla\rho\right] \\ &= \rho\left[\nabla\cdot\left(\frac{\dot{a}}{a}\mathbf{r} + \mathbf{u}\right)\right] + \left(\frac{\dot{a}}{a}\mathbf{r} + \mathbf{u}\right)\cdot\left[\nabla\rho\right] \\ &= \rho\left[\frac{\dot{a}}{a}3 + \nabla\cdot\mathbf{u}\right] + \frac{\dot{a}}{a}\mathbf{r}\cdot\nabla\rho + \mathbf{u}\cdot\nabla\rho \\ &= \frac{\dot{a}}{a}3\rho + \frac{1}{a}\rho\nabla_{\check{\mathbf{x}}}\cdot\mathbf{u} + \frac{\dot{a}}{a}\mathbf{x}\nabla_{\check{\mathbf{x}}}\rho + \frac{1}{a}\mathbf{u}\cdot\nabla_{\check{\mathbf{x}}}\rho \\ &= \frac{\dot{a}}{a}\left(3\rho + \mathbf{x}\cdot\nabla_{\check{\mathbf{x}}}\rho\right) + \frac{1}{a}\nabla_{\check{\mathbf{x}}}\cdot\left(\rho\mathbf{u}\right). \end{aligned} \tag{D.13}$$

After the terms are combined, the continuity equation in comoving coordinates is:

$$\frac{\partial \rho}{\partial t} + \frac{1}{a}\nabla_{\breve{\mathbf{x}}} \cdot (\rho \mathbf{u}) + 3\frac{\dot{a}}{a}\rho = 0. \tag{D.14}$$

D.2 Density contrast

The equations determined in Chapter D.1 are in terms of the density. It is more useful to define the equations in terms of the density contrast:

$$\delta \equiv \frac{\rho - \bar{\rho}}{\bar{\rho}}. \tag{D.15}$$

The Euler equation remains unchanged. The Poisson equation, equation (D.11), becomes equation (6.25).

For the continuity equation each term will be calculated separately. The first term in equation (D.14) becomes:

$$\begin{aligned} \frac{\partial \rho}{\partial t} &= \frac{\partial \left(\bar{\rho} + \bar{\rho}\delta\right)}{\partial t} \\ &= \dot{\bar{\rho}}\left(1 + \delta\right) + \bar{\rho}\dot{\delta} \\ &= -3\frac{\dot{a}}{a}\bar{\rho}\left(1 + \delta\right) + \bar{\rho}\dot{\delta}, \end{aligned} \tag{D.16}$$

where $\dot{\bar{\rho}}$ was calculated by using $\bar{\rho}a^3 = const.$ The second term becomes:

$$\frac{1}{a}\nabla \cdot (\rho \mathbf{u}) = \frac{1}{a}\bar{\rho}\nabla \cdot \left[(1 + \delta)\,\mathbf{u}\right], \tag{D.17}$$

and the third term becomes:

$$3\frac{\dot{a}}{a}\rho = 3\frac{\dot{a}}{a}\bar{\rho}\left(1 + \delta\right). \tag{D.18}$$

Resulting in the comoving density contrast continuity equation:

$$\frac{\partial \delta}{\partial t} + \frac{1}{a}\nabla \cdot \left[(1 + \delta)\,\mathbf{u}\right] = 0. \tag{D.19}$$

D.3 Solution in the linear regime

To solve the equations in comoving coordinates the system needs to be linearised, as discussed in Section 6.4. An evolution equation for the density contrast can be determined by combining the divergence of equation (6.27) and the time derivative of equation (6.28), i.e.

$$0 = \frac{\partial A}{\partial t} - \frac{1}{a}\nabla \cdot B, \tag{D.20}$$

where A is equation (6.28) and B is equation (6.27). The first term is:

$$\begin{aligned}
\frac{\partial A}{\partial t} &= \frac{\partial}{\partial t}\left(\frac{\partial \delta}{\partial t} + \frac{1}{a}\nabla \cdot \mathbf{u}\right) \\
&= \frac{\partial^2 \delta}{\partial t^2} - \frac{\dot{a}}{a^2}\nabla \cdot \mathbf{u} + \frac{1}{a}\frac{\partial}{\partial t}\nabla \cdot \mathbf{u} \\
&= \frac{\partial^2 \delta}{\partial t^2} + \frac{\dot{a}}{a}\frac{\partial \delta}{\partial t} + \frac{1}{a}\frac{\partial}{\partial t}\nabla \cdot \mathbf{u},
\end{aligned} \tag{D.21}$$

and the second term is:

$$\begin{aligned}
\frac{1}{a}\nabla \cdot B &= \frac{1}{a}\nabla \cdot \left(\frac{\partial \mathbf{u}}{\partial t} + \frac{\dot{a}}{a}\mathbf{u} + \frac{1}{a}\nabla\Phi\right) \\
&= \frac{1}{a}\left(\frac{\partial}{\partial t}\nabla \cdot \mathbf{u} + \frac{\dot{a}}{a}\nabla \cdot \mathbf{u} + \frac{1}{a}\triangle\Phi\right) \\
&= \frac{1}{a}\left(\frac{\partial}{\partial t}\nabla \cdot \mathbf{u} - \dot{a}\frac{\partial \delta}{\partial t} + \frac{1}{a}\triangle\Phi\right).
\end{aligned} \tag{D.22}$$

After combining the two terms, the evolution equation for the density contrast in a pressure-less fluid is:

$$\frac{\partial^2 \delta}{\partial t^2} + 2\frac{\dot{a}}{a}\frac{\partial \delta}{\partial t} - 4\pi G\bar{\rho}\delta = 0. \tag{D.23}$$

D.4 Introducing pressure

During the radiation dominated era, particles in the fluid experience pressure. The Euler equation will contain the pressure term:

$$-\frac{\nabla P}{\rho}, \tag{D.24}$$

where $P = c_s^2\rho$, c_s is the speed of sound in the fluid. This term can be re-written in terms of the density contrast:

$$\begin{aligned}
\frac{\nabla P}{\rho} &= \frac{c_s^2}{\rho a}\nabla\rho \\
&= \frac{c_s^2}{a\bar{\rho}\left(1+\delta\right)}\nabla\bar{\rho}\left(1+\delta\right) \\
&= \frac{c_s^2}{a\left(1+\delta\right)}\nabla\left(1+\delta\right) \\
&= \frac{c_s^2}{a}\left(1-\delta\right)\nabla\delta+\mathcal{O}\left(2\right) \\
&= \frac{c_s^2}{a}\nabla\delta. \qquad \text{(D.25)}
\end{aligned}$$

After including this term the Euler equation reads:

$$\frac{\partial\mathbf{u}}{\partial t}+\frac{\dot{a}}{a}\mathbf{u}+\frac{1}{a}\nabla\Phi+\frac{c_s^2}{a}\nabla\delta = 0. \qquad \text{(D.26)}$$

The same linearising procedure is perform with the new Euler equation, the divergence of the above equation is:

$$\begin{aligned}
\frac{1}{a}\nabla\cdot B &= \frac{1}{a}\nabla\cdot\left(\frac{\partial\mathbf{u}}{\partial t}+\frac{\dot{a}}{a}\mathbf{u}+\frac{1}{a}\nabla\Phi+\frac{c_s^2}{a}\nabla\delta\right) \\
&= \frac{1}{a}\left(\frac{\partial}{\partial t}\nabla\cdot\mathbf{u}+\frac{\dot{a}}{a}\nabla\cdot\mathbf{u}+\frac{1}{a}\triangle\Phi+\frac{c_s^2}{a}\triangle\delta\right) \\
&= \frac{1}{a}\left(\frac{\partial}{\partial t}\nabla\cdot\mathbf{u}-\dot{a}\frac{\partial\delta}{\partial t}+\frac{1}{a}\triangle\Phi+\frac{c_s^2}{a}\triangle\delta\right). \qquad \text{(D.27)}
\end{aligned}$$

Substituting this into equation (D.20), the propagation equation is:

$$\begin{aligned}
0 &= \frac{\partial A}{\partial t}-\frac{1}{a}\nabla\cdot B \\
&= \ddot{\delta}+2H\dot{\delta}-\frac{1}{a^2}\triangle\Phi-\frac{c_s^2}{a^2}\triangle\delta \\
\ddot{\delta}+2H\dot{\delta} &= 4\pi G\bar{\rho}\delta+\frac{c_s^2}{a^2}\triangle\delta. \qquad \text{(D.28)}
\end{aligned}$$

By decomposing the perturbations into plain waves i.e. $\delta\left(\mathbf{x},t\right)=C\exp\left(-i\left[\mathbf{k}\cdot\mathbf{x}-\omega t\right]\right)$,

$$-\omega^2\delta+i\omega 2H\delta = 4\pi G\bar{\rho}\delta-\frac{c_s^2k^2}{a^2}\delta. \qquad \text{(D.29)}$$

The dispersion relation is obtained:

$$\begin{aligned} \omega^2 &= \frac{c_s^2 k^2}{a^2} - 4\pi G\bar{\rho} \\ &= c_s^2 \left[\frac{k^2}{a^2} - \frac{4\pi G\bar{\rho}}{c_s^2}\right], \end{aligned} \tag{D.30}$$

where $k = \frac{2a\pi}{\lambda}$. The above equation can be written in terms of the wavelength:

$$\begin{aligned} \omega^2 &= c_s^2 \left[\frac{(2\pi)^2}{\lambda^2} - \frac{4\pi G\bar{\rho}}{c_s^2}\right] \\ &= c_s^2 \left[\frac{(2\pi)^2}{\lambda^2} - \frac{(2\pi)^2}{\lambda_J^2}\right] \\ &= 4\pi^2 c_s^2 \left[\frac{1}{\lambda^2} - \frac{1}{\lambda_J^2}\right], \end{aligned} \tag{D.31}$$

where λ_J is the Jeans length and is defined in equation (3.42).

Appendix E

Time evolution equations in dimensionless co-ordinates

E.1 Converting to dimensionless expressions

To convert the evolution equations to dimensionless form the dimensionless variables need to be defined. Section 6.5 defined the dimensionless variables τ and $\mathbf{x}$ as equation (6.37) and (6.34), respectively. The derivative with respect to time and space in dimensionless variables becomes equation (6.37) and (6.38), respectively.

The proper velocity of an object is defined as equation (6.39) from Section 6.5. All terms that include taking the gradient and/or Laplace of a variable need to be replaced by the dimensionless equivalents, i.e:

$$\nabla_{\tilde{\mathbf{x}}} = \frac{2\pi}{L}\nabla_{\mathbf{x}}, \tag{E.1}$$

$$\tilde{\triangle} = \left(\frac{2\pi}{L}\right)^2 \triangle, \tag{E.2}$$

respectively.

The full derivations of equation (6.41), (6.42) and (6.40) can be found in the sections below.

E.1.1 Density contrast

The continuity equation in comoving physical coordinates reads:

$$\dot{\delta} + \frac{1}{a}\tilde{\nabla}\cdot\left[(1+\delta)\,\tilde{\mathbf{u}}\right] = 0. \tag{E.3}$$

Using the conversions from Section E.1, the dimensionless continuity equation is:

$$
\begin{aligned}
\dot{\delta} + \frac{1}{a}\tilde{\nabla}\left[(1+\delta)\,\tilde{\mathbf{u}}\right] &= 0 \\
\frac{3}{2}H_0\delta' + \frac{1}{a}\frac{2\pi}{L}\nabla\left[(1+\delta)\,\frac{3LH_0}{4\pi}\mathbf{u}\right] &= 0 \\
\frac{3}{2}H_0\delta' + \frac{3H_0}{2a}\nabla\left[(1+\delta)\,\mathbf{u}\right] &= 0 \\
\delta' + \frac{1}{a}\nabla\left[(1+\delta)\,\mathbf{u}\right] &= 0. \qquad \text{(E.4)}
\end{aligned}
$$

E.1.2 Velocity equations

The Euler equation in comoving physical coordinates reads:

$$
\dot{\tilde{u}} + H\tilde{\mathbf{u}} + \frac{1}{a}\left(\tilde{\mathbf{u}}\cdot\nabla_{\tilde{\mathbf{x}}}\right)\tilde{\mathbf{u}} = -\frac{1}{a}\nabla_{\tilde{\mathbf{x}}}\Phi. \qquad \text{(E.5)}
$$

Using the conversions from Section E.1:

$$
\begin{aligned}
&\frac{3}{2}H_0\frac{3LH_0}{4\pi}\mathbf{u}' + H\frac{3LH_0}{4\pi}\mathbf{u} \\
&+\frac{1}{a}\left(\frac{3LH_0}{4\pi}\mathbf{u}\cdot\frac{2\pi}{L}\nabla_{\mathbf{x}}\right)\frac{3LH_0}{4\pi}\mathbf{u} &= -\frac{1}{a}\frac{2\pi}{L}\nabla_{\mathbf{x}}\Phi \\
\frac{9LH_0^2}{8\pi}\mathbf{u}' + \frac{3LH_0H}{4\pi}\mathbf{u} + \frac{1}{a}\frac{9LH_0^2}{8\pi}\left(\mathbf{u}\cdot\nabla_{\mathbf{x}}\right)\mathbf{u} &= -\frac{2\pi}{La}\nabla_{\mathbf{x}}\Phi \\
\mathbf{u}' + \frac{2}{3}\frac{H}{H_0}\mathbf{u} + \frac{1}{a}\left(\mathbf{u}\cdot\nabla_{\mathbf{x}}\right)\mathbf{u} &= -\frac{2\pi}{La}\frac{8\pi}{9LH_0^2}\nabla_{\mathbf{x}}\Phi \\
\mathbf{u}' + \frac{2}{3}\frac{H}{H_0}\mathbf{u} + \frac{1}{a}\left(\mathbf{u}\cdot\nabla_{\mathbf{x}}\right)\mathbf{u} &= -\frac{1}{a}\left(\frac{4\pi}{3LH_0}\right)^2\nabla_{\mathbf{x}}\Phi. \qquad \text{(E.6)}
\end{aligned}
$$

Equation (3.30) can be used to simplify the second terms and the last term requires a factor of c^2 to be dimensionless, the dimensionless Euler equation is:

$$
\mathbf{u}' + \frac{2}{3}\frac{1}{\tau}\mathbf{u} + \frac{1}{a}\left(\mathbf{u}\cdot\nabla_{\mathbf{x}}\right)\mathbf{u} = -\frac{1}{a}\left(\frac{4\pi c}{3LH_0}\right)^2\nabla_{\mathbf{x}}\Phi. \qquad \text{(E.7)}
$$

E.1.3 Poisson equation

The Poisson equation in comoving physical coordinates reads:

$$
\delta = \frac{1}{4\pi G\rho a^2}\tilde{\triangle}\Phi. \qquad \text{(E.8)}
$$

Using the conversions from Section E.1, it becomes:

$$\left(\frac{2\pi}{L}\right)^2 \triangle\Phi = 4\pi G\bar{\rho}a^2\delta. \tag{E.9}$$

The terms a and $\bar{\rho}$ can be replaced by τ equivalent terms, equation (3.29) and (3.31):

$$\begin{aligned}\left(\frac{2\pi}{L}\right)^2 \triangle\Phi &= 4\pi G\left(\frac{3}{8\pi G}H_0^2\tau^{-2}\right)\left(\tau^{2/3}\right)^2\delta \\ \triangle\Phi &= \frac{L^2}{4\pi^2}\frac{3H_0^2}{2}\tau^{-2/3}\delta \\ \triangle\Phi &= \frac{3}{2}\left(\frac{LH_0}{2\pi c}\right)^2\tau^{-2/3}\delta,\end{aligned} \tag{E.10}$$

where a factor of c is included to ensure the constant is dimensionless.

E.2 Growing mode

Using the general solution to the propagation equation from Section 6.6, equation (6.49), and setting the decaying mode to zero, the density contrast grows according to equation (6.50). The linearised continuity equation is equation (6.50) which can be used to calculate the peculiar velocity:

$$\begin{aligned}\delta' &= -\frac{1}{a}\nabla\mathbf{u} \\ \frac{2}{3}\tau^{-1/3}\tau_i^{-2/3}\delta_{ini}(\mathbf{x}) &= -\tau^{-2/3}\nabla\mathbf{u} \\ \frac{2}{3}\tau^{1/3}\tau_i^{-2/3}\delta_{ini}(\mathbf{x}) &= -\nabla\mathbf{u}.\end{aligned} \tag{E.11}$$

The Poisson equation, equation (E.10), is then used to determine the relationship between the potential and the peculiar velocity:

$$\begin{aligned}\frac{2}{3}\tau^{1/3}\tau_i^{-2/3}\frac{2}{3}\left(\frac{2\pi c}{LH_0}\right)^2\tau^{2/3}\triangle\Phi &= -\nabla\mathbf{u} \\ \left(\frac{4\pi c}{3LH_0}\right)^2\tau\tau_i^{-2/3}\triangle\Phi &= -\nabla\mathbf{u} \\ \left(\frac{4\pi c}{3LH_0}\right)^2\tau\tau_i^{-2/3}\nabla\Phi &= -\mathbf{u}.\end{aligned} \tag{E.12}$$

To obtain the initial velocity, the above equation is evaluated at $\tau = \tau_i$ as shown in equation (6.52) in Section 6.6.